High Intensity Effects in Bandgap Materials

Dissertation
an der Fakultät für Physik
der Ludwig–Maximilians–Universität
München

von

Ayman Akil

Kolumbien

2017

Erstgutachter: Prof. Dr. Ferenc Krausz
Zweitgutachter: Prof. Dr. Abdallah Azzeer
Datum der Abgabe: 29.03.2017
Tag der mündlichen Prüfung: 05.05.2017

Kurzzusammenfassung

Die höchsten heutzutage zuverlässig realisierbaren Betriebsfrequenzen in der Elektronik liegen im Gigahertzbereich (10^9 Hz). Könnte man stattdessen nichtlineare optische Phänomene zur Signalverarbeitung verwenden, wären Taktraten im Sub-petahertz (10^{15} Hz) Bereich möglich. Ein solcher Geschwindigkeitssprung würde fast unweigerlich die Informationstechnologie revolutionieren.
Die Untersuchung solcher Phänomene und ihrer Eignung zum Optoelektronischen Schalten, ist eng verknüpft mit dem Verständnis der zugrundeliegenden Wechselwirkung von Licht und Materiel auf der Zeitskala einer einzelnen Schwingung des verwendeten Lichts, im sichtbaren Spektrum also wenigen Femtosekunden.

Für eine hypothetische Anwendung von optischen Effekten für die ultraschnelle Schaltung müssen das ausgewählte optische Phänomen und konventionelle elektronischen Schaltkreise miteinander verbunden werden. Aus diesem Grund ist die Erweiterung der Fähigkeiten der AttoSekundenspektroskopie entscheidend, um elektronischen Anregungen in Halbleitern, welche kleine Energielücken zwischen Valenz- und Leitungszustände aufweisen, zu studieren. Diese bilden die Bausteine der modernen Elektronik.
Aus den genannten Gründen und mehreren experimentellen Betrachtungen welche im Haupttext ausführlich dargestellt sind, haben wir eine Halbleiterlegierung, Galliums-Arsenide (GaAs), mit einer direkten Bandlücke in dem Spektralbereich des sichtbaren Lichtes als geeignetes Material ausgewählt, um die AttoSekundenphotoelektronspektroskopie anzuwenden.
Die Attosekundenphotoelektronspektroskopie hat sich als ein geeignetes Verfahren erwiesen, um die Auslösezeit von Photoelektronen aus metallischen Oberflächen zu erforschen. Die Technik zeigt theoretisch auch Potential zur Erforschung von elektronischen Erregungsdyamiken. Jedoch müssen mehrere experimentelle Herausforderungen überwunden werden. Die folgenden Kapitel stellen die Ergebnisse der Attosekundephotoelektronspektroskopie an einem Bandlückenmaterialien, in dem ein Lichtflelden elektronische Anregung induziert, vor.

Contents

Chapter 1

Introduction

The current operating frequency of electronics is in the range of a few Gigahertz (10^9 Hz). If nonlinear optical phenomena could be used instead of electronic switching clock rates, the sub-petahertz (sub-10^{15} Hz) range would become feasible and have revolutionary effects on technology. To study such phenomena and test their suitability for hypothetical future opto-electronic switches, experiments have to be carried out that allow to track light-matter interaction with a temporal resolution surpassing the few-femtosecond half-cycle duration of visible light.

In the past decade, a range of novel experiments achieved the required attosecond temporal resolution and allowed to track light-field driven electronic processes in gas phase experiments. More recently, by applying a transient absorption scheme, the toolbox of attosecond spectroscopy has been expanded to also allow the investigation of condensed matter systems. Sub-optical-cycle resolution has been demonstrated studying the interaction of ultra-intense and –short laser pulses with wide-energy-gap dielectric materials.

For a hypothetical use of optical effects for ultrafast switching, the optical phenomenon of choice has to be interconnected to electronic devices. It is therefore crucial to expand the capabilities of attosecond spectroscopy to the study of electronic excitations also in semiconducting materials that exhibit small energy gaps between valence and conduction states and are the building blocks of modern electronics.

This thesis reports on a series of experiments where photoelectron emission triggered by extreme ultraviolet (XUV) light bursts of attosecond duration serves as probe of the instantaneous occupation of the energy bands after optical excitation.

Photoelectron spectroscopy is a versatile tool widely used to probe the electronic configuration and population distribution on the surface of matter. Upon XUV irradiation, the photoelectric effect causes electrons to leave the surface and the occupation distribution in the energy bands is mapped onto a momentum spread of the ejected electrons, which can be measured by detecting their flight-time distribution. Owing to specifically tailored attosecond probe pulses, the experiments discussed here combine sub-femtosecond resolution of the probing with a strong temporal confinement of the excitation process due to the employment of few-cycle optical excitation pulses.

Optical switching should be efficient with regard to the achievable transfer of population between the localized valence band states and the mobile conduction band states that contribute to an increase in conductivity. In addition, the switching process should be reversible in order to allow for a complete return of the system to its non-conductive ground state after the switching operation. An elegant approach to meet both conditions is the application of coherent population transfer under conditions that allow Rabi-oscillations to occur.

Rabi oscillations are described by the optical Bloch equations and defined as the cyclic population transfer between two energy levels of an isolated quantum system under the influence of a resonant electromagnet field. While in the idealized case of perfect resonance between field and transition energy true unity population transfer can be achieved, for longer exposure to the driving field, i.e. half a period of the cyclic population transfer later the process is also fully reversible.

Seeking the condensed matter analogy, a semiconductor material with energy levels arranged in valence- and conduction bands separated by the band-gap can serve as the two-level quantum system. Furthermore, if the continuous wave driving field is replaced by ultrashort pulse excitation, the processes that cause rapid decoherence in solid-state devices and thus would be detrimental to the fidelity of cyclic population dynamics can be largely eliminated.

For these reasons and a number of experimental considerations detailed in the main text, we chose Gallium-Arsenide (GaAs), a semiconducting alloy with a direct bad-gap in the spectral range of visible light as suitable material to apply attosecond photoelectron spectroscopy and seek ultrafast Rabi-type oscillations of the population dynamics

Earlier experiments already provided an indication of possible Rabi oscillations with a period that ranges between $50fs$ and $1ps$ [1], [2]. The central aim of the efforts discussed here was to develop the experimental capability to explore if this timescale can be shortened such that efficient population transfer becomes feasible on the timescale of optical oscillations.

Attosecond photoelectron spectroscopy has proven to be applicable to explore the escape time of photoelectrons from metallic surfaces [1]. These experiments have shown that the technique in principle holds promise to allow the time resolved exploration of electronic excitation dynamics. For that, several experimental challenges had to be overcome and the following chapters demonstrate the achievements along the quest for attosecond time resolved photoelectron spectroscopy of light field induced electronic excitations in band-gap materials.

Descriptive Outline

Chapter 2, presents the experimental and theoretical tools of photoemission streaking experiments (PES). It includes a description of the femtosecond laser systems and the experimental setup consisting of the beamline chambers and optical layouts. The theory of the process of high harmonic generation is explained and a description is given of the diagnostic tools used to characterize the pulses.

Chapter 3 is an overview of the theory of Rabi oscillations in bandgap materials. It describes the simplified case of a two level model and then studies the possible candidates for a PES experiment. Finally, we discuss the reasons for choosing GaAs as a preferable sample to undertake the measurement.

The detailed sample preparation process is described in chapter 4. We managed to prepare a clean single structure (100) GaAs surface using an Arsenide-capped GaAs sample grown at Walter Schottky Institute at TUM in Garching bei München. In order to test the quality of our sample surface, we used low-energy electron diffraction (LEED) and X-ray photoemission spectroscopy (XPS). The results of both techniques are presented and assure near perfect single crystalline sample conditions and an uncontaminated sample surface.

In chapter 5, we discuss the efforts to develop a Chromium\scandium multilayer XUV mirror which reflects at $145 eV$ central energy. This relatively high center energy of the XUV multilayer mirror helps to isolate the XUV triggered photoelectron emission energetically from the laser generated above-threshold photoelectrons generated by a multiphoton process. At the same time, the mirror is optimized to offer the best possible energy resolution (1.8 eV badnwidth) while still maintaining sub-femtosecond temporal resolution.

The first application of this mirror allowed for the first time in an attosecond time resolved experiment to spectrally resolve and separate the valence-band photoelectron emission from photoelectrons originating from atomic orbitals in GaAs. This allows for a clear spectral assignment of laser induced electronic transitions from the valence to the conduction band. In this chapter, also the retrieval of the surface emission time difference between electrons from Gallium- and Arsenic-electron orbitals is presented.

Chapter 6 investigates the space-charge effect, a common challenge for PES experiments, specifically under the influence of strong pump light. The photoelectrons ejected from the surface by the laser field form a charged cloud leaving the sample surface and detector. On their way to the detector, the XUV ejected photoelectrons have to penetrate this cloud or they will acquire an additional momentum transfer depending on the arrival time difference between the NIR and XUV pulses. This interplay results in a characteristic modification of the time-of-flight distribution of the XUV generated photoelectrons and is analyzed to conclude on the number of laser-generated photoelectrons form a graphene covered surface that was investigated as an alternative material due to its unique band-structure.

Chapter 7 summarizes the outcome of the studies and demonstrates the remaining challenges that prevented the definite observation of electronic excitations in GaAs. The chapter analyzes which fundamental experimental hurdles remain and presents how some of them can be overcome in very specific sample configurations. By the example of a graphene covered surface we demonstrate first experimental evidence for the ultra-rapid buildup of conduction band population that outlasts the pulse duration of the excitation pulse.

Chapter 8 presents a summary of the findings and gives recommendations for future attempts to use attosecond time resolved photoelectron spectroscopy to explore light field induced electronic excitations in band-gap materials.

Chapter 2

Experimental and Theoretical tools

2.1 Principles of Attosecond Experiments

Studying the dynamics of a phenomenon needs a gating mechanism which can work on a comparable time scale [3]. As long as the time scale of the phenomenon under study is larger than picosecond, special electronic devices can be used to study the system, but if we want to study faster systems then a new approach needs to be crafted. This approach involves a pump probe experiment where two synchronized light pulses are used, one is used to initiate a phenomena and the second is used to probe it. More specifically, investigating electron's dynamics in molecules and atoms requires femtosecond and sub-femtosecond resolution which is far beyond the reach of electronic metrology. Such requirements are only satisfied by the development of short pulsed lasers which achieve a resolution down to tens of attoseconds.

2.1.1 Waveform controlled few femtosecond pulses

The electric field of the laser pulses can be defined either by the spatial and temporal characteristics $E(r,t)$ or the spatial and spectral characteristics $E(r,\omega)$, where r denotes the spatial coordinate while t and ω denote the temporal and spectral coordinates, respectively. Both, spectral and time domains, are connected by the Fourier theorem, this implies that spectral width and the duration of a laser pulse are connected via the relation:

$$\Delta t \cdot \Delta\omega \geq C \tag{2.1}$$

where C denotes a constant that depends mainly on the pulse shape. Table 1 gives the value of C in the case of a Gaussian, Sech and Square pulse shape.

In the case of a Gaussian shaped pulse, which is the case in the course of the

Table 2.1: Values of the constant C for different pulse shapes.

Pulse Shape	Intensity Profile	C
Gauss	$\exp(-2(\frac{t}{\tau_{gauss}})^2)$	0.441
Sech	$sech^2(\frac{t}{\tau_{sech}})$	0.315
Square	1 or 0	0.443

pulses described in this thesis, the previous equation can be rewritten as follows:

$$\Delta t[fs] \cdot \Delta(\hbar\omega)[eV] \geq 1.83 \tag{2.2}$$

To describe a laser pulse at an arbitrary point in space, one can consider this representation of the electric field:

$$\overrightarrow{E}(t) = \widetilde{E}(t)\exp(i\phi_{CEP})\exp(i\phi(t))\exp(i\omega_L t) \tag{2.3}$$

where $\widetilde{E}(t)$ denotes the real envelope function, ϕ_{CEP} the carrier envelope phase (CEP), ϕ(t) the temporal phase and ω_L the central frequency of the laser pulse. If we assume that the laser pulse has an envelope with a Gaussian form, then the real envelope function can be defined as follow:

$$\widetilde{E}(t) = \overrightarrow{E_0}\exp(-\frac{2\ln 2}{\tau_L^2} \cdot t^2) \tag{2.4}$$

where τ_L denotes the full width at half maximum of the laser pulse. In order to extract the instantaneous frequency of the laser pulse, one has to perform the derivative of the temporal phase,

$$\omega(t) = \omega_L + \frac{d}{dt}\phi(t) \tag{2.5}$$

where $\phi(t)$ is the time dependent phase. We can expand $\phi(t)$ in Taylor series in powers of t,

$$\phi(t) = a_0 t + a_1 t^2 + a_2 t^3 + ... \tag{2.6}$$

It is clear that there is no time-independent term in $\phi(t)$ and this is due to its definition in (3) where the time-independent term was included in the carrier envelope phase ϕ_{CE}. If $\phi(t)$ is nonzero then the pulse is said to be chirped. This chirp can be linear, quadratic, etc. for n=1, 2, etc.. Moreover, the pulse can be positively or negatively chirped depending on the sign of a_n. In order to achieve a flat phase, i.e. $\omega(t) = constant$, $\frac{d}{dt}\phi(t) = 0$ and the parameter a_n should be zero for all $n > 0$. The later condition is necessary for the pulse to have the shortest possible pulse length, which is called Fourier limited pulse [3]. In this case, the relative phase of the electric field under the envelope is described by ϕ_{CEP} and this is why it is called the carrier-envelope phase (CEP). This parameter

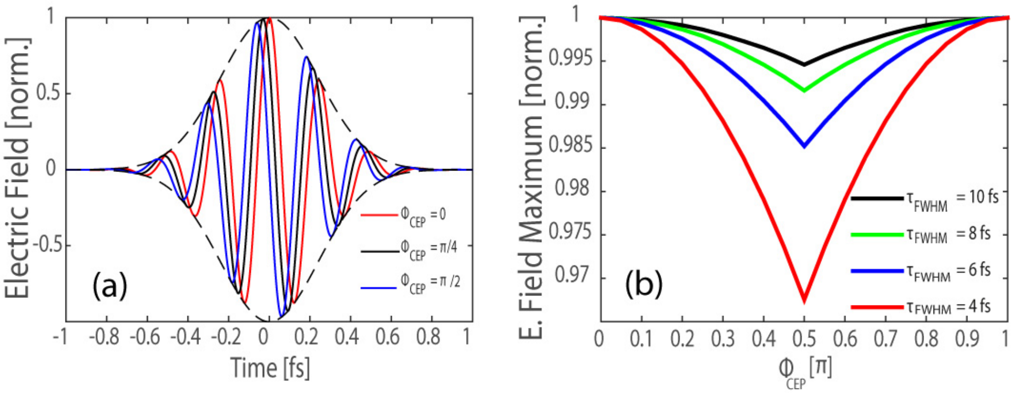

Figure 2.1: (a) Electric field of one and a half cycle Gaussian pulses with different CEP and identical envelope. (b) Variation of the envelope peak intensity with respect to four different pulse duration. The peak intensity of the pulse increases when the pulse duration decreases [4]
.

becomes of extreme importance when the pulse is short enough to be comparable to the oscillation period. Figure 2.1 shows 1.5-cycle pulses with different carrier-envelope phase (CEP). In the case of $CEP = 0$, the peak intensity of the pulse is determined by the electric field. This is better explained in Figure 2.1(a), where the CEP dependence is shown in the case of several pulses durations.

2.1.2 Generation of isolated attosecond pulses

In order to study the dynamics of electronic excitation, we should aim at sub-femtosecond resolution. One way to do so, is the high harmonic generation (HHG). The main idea is to generate photons which have higher energies compared to the driving near infrared (NIR) pulses. In this section we are interested in creating photons in the extreme ultraviolet (XUV) region and for that we need to address the non linear response of a material under the effect of a very intense electromagnetic field, this process is called high harmonic generation (HHG). In HHG process, an intense linearly polarized NIR pulses are focused into a gas target. The polarization in a material is expressed as:

$$P = \widetilde{\epsilon_0}(\chi^{(1)} E_L(t) + \chi^{(2)} E_L(t)^2 + \chi^{(3)} E_L(t)^3 + ...) \tag{2.7}$$

where ϵ_0 is the vacuum permittivity and χ is the susceptibility of the material while $E_L(t)$ denotes the applied electric field [3]. It is clear from the previous equation that the polarization response of a material will involve terms that are proportional to the square, cube, ... of the intense electric field. In order to see how this translate into the frequency of the components being generated, one has to substitute the time dependent part of the electric field $\exp i\omega t$ into (7) which will results the following

$$P = \widetilde{\epsilon_0}(\chi^{(1)} \exp{(iwt)} + \chi^{(2)} \exp{(2iwt)} + \chi^{(3)} \exp{(3iwt)} + ...) \tag{2.8}$$

The semiclassical three step model

The yield of the HHG process is clearly shown in Figure 2.2(a) where we observe three regimes. The perturbation theory is used in the previous equation, it usually gives a good prediction for low order harmonics (perturbative regime). For higher harmonics, the perturbative theory fails to explain the yield since we see a plateau regime as seen in Figure 2.2(a) where the harmonics are generated with the same efficiency. This is true up to a cutoff frequency where the efficiency of higher harmonics starts to decrease again until it vanishes (cutoff regime). In order to explain this behavior, we use a semiclassical approach called the three step model [5, 6]. This model is shown in Figure 2.2(b) where the first step involves the ionization of an electron wave packet from the parent atom after a strong linearly polarized electric field bends the potential of the atom. The intensity of the electric field should be comparable to the atomic electric field strength of the atom in order for the tunneling to take place. The electron wave packets are released to the continuum with twice the driving laser frequency [7], then they are accelerated due to the driving electric field and this is labeled as step two. The third and final step describes the back acceleration of the electron wave packets towards the parent atom when the driving electric field changes its direction in the following quarter wave cycle. These accelerated electron wave packets can then recombine with the parent atom with a small probability where they release the energy they gained during the acceleration in the electric field in addition to the ionization energy in the form of a high energetic photons. The semiclassical three step model is considered to be the standard approach to describe the generation of high harmonics, still there is a more sophisticated quantum mechanical description which is published by Lewenstein et al. in [8].The yield of this completely quantum mechanical model is very similar to the semiclassical three step model which is a good surprise considering the ability of the later classical model to successfully predicts an inherently quantum process as the HHG process.

The three step model suggests that the HHG takes place only in half of the cycle period of the electric field whose central frequency is denoted by ω_L. This suggests that the generated harmonics are $2\omega_L$ apart in frequency. As seen in Figure 2.2 (a), the harmonics on the plateau regime can reach maximum energy at a point labeled as the cutoff energy E_{cutoff} which is given as follows:

$$E_{cutoff} = I_P + 3.17 U_P \tag{2.9}$$

where I_P is defined as the ionization potential of the atoms and U_P is the ponderomotive potential of the electron in the presence of the driving laser field. The factor 3.17 comes from a semiclassical calculations done by F. Quere et al. in [9]. The ponderomotive potential U_P is given by this equation:

$$U_P = \frac{e^2 E_L^2}{4 m \omega_L^2} \tag{2.10}$$

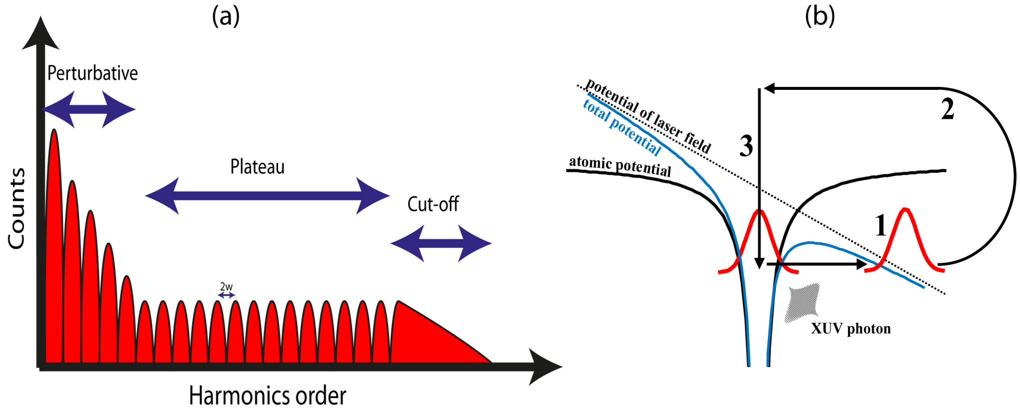

Figure 2.2: (a) XUV spectrum produced in HHG process. It is clear that we have three regimes: perturbative regime, plateau, and the cut-off. (b) Sketch of the semiclassical step model

where E_L is the electric field at its peak, m and e are the mass and charge of the electron respectively.

Isolated attosecond pulses

As seen in Figure 2.2(a), when the XUV energy is larger than E_{cutoff}, the yield of the HHG process diminishes exponentially with respect to the photon energy. The instant of ionization of the photoelectron determines the path of this liberated electron and consequently determines also the energy of the generated high harmonic photon, this is described in [10]. The optimum HHG photon energy is highly dependent on the CEP of the driving laser electric field. Consider the case given in Figure 2.1(a), it is clear that for the case of ϕ_{CE} =0 we have the largest discrepancy between the highest spike and the next highest one. In order to understand the modulation seen in the plateau of the figure 2.2(a), we need to consider high harmonic pulses being generated at different instants during subsequent half cycles and therefore interference takes place giving rise to these modulations. While in the cutoff regime, the modulations are highly reduced since electrons of this region are mainly generated from the highest peak of the driving laser pulse and thus there is no comparable peak in this case as long as the condition of ϕ_{CE} =0, i.e. the pulse have a cosine waveform, is satisfied. On the other hand, the shorter the driving laser pulse the broader the cutoff region since a shorter laser pulse means that we have relatively more high harmonics generated near the highest peak in the pulse. From the experimental perspective, we need to choose the right spectral filters and mirrors in order to end up with isolated attosecond pulses which are generated in the cutoff region and inherently synchronized with the driving laser pulse. According to [11,12], we can reach sub-hundred attosecond pulses at 90 eV center energy using this approach. There are different approaches to produce isolated attosecond pulses such as polarization gating technique mentioned in [13], though in our experiments we use the first approach to attain isolated attosecond pulses. Typically we use XUV multilayer mirrors reflecting at different center energies and with bandwidth that ranges between 1.8 eV up to 5 eV. It is clear from the high harmonic spectrum in the cutoff region that the efficiency decreases exponentially at high energy, so the XUV mirror will still reflect some of the XUV pulses even at lower energies compared to its chosen center energy. In order to more suppress these undesired XUV pulses, we use metal filters that have a transmission curve that opens at high energies only so that it highly suppresses the unwanted XUV pulses in addition to the NIR pulses. Finally, we end up with co-propagating XUV and NIR pulses which are concentric with the XUV being in the center. The co-propagation is guaranteed due to the phase matching in the gas medium where the high harmonics generation takes place since the constructive interference lies in the forward direction.

2.1.3 Characterization of the femtosecond and attosecond pulses

One of the most important advantages of ultrafast science is also one of its standard problems: there is no measurement device in the laboratory that matches the time resolution of the pulses, the electric devices has for example has a lower time resolution limit of picoseconds which is about 10^6 times slower than systems to be studied . To characterize the pulses one typically has to employ correlation by using using a replica of the pulse as a gating mechanism.

Frequency resolved optical gating of few cycle NIR pulses

Basically, there is no device that can measure and characterize the ultrafast pulses. One has to create a variable delayed replica of the pulse and then introduce a delay τ between the original pulse and its replica before overlapping them in a non linear medium. This yields a spectrogram $S(\omega, \tau)$ that has the following form:

$$S(\omega, \tau) = \left| \int_{-\infty}^{\infty} E(t) g(t-\tau) e^{-i\omega t} dt \right|^2 \tag{2.11}$$

where $g(t-\tau)$ is the gate function versus delay τ , $E(t)$ is the electric field and ω is the angular frequency. A spectrometer is used to collect a transmitted spectrum for each delay step τ. This yield a spectrogram $S(\omega, \tau)$ which contains the necessary information to characterize the ultrafast NIR pulse [14, 15].

In our laboratory, we employ two kinds of FROGs, the second harmonic FROG (SHG) in addition to the transient grating FROG (TG). In the case of SHG FROG, the nonlinearity is of second order and the spectrogram of this gating mechanism $S_{SHG}(\omega,\tau)$ is defined as follows:

$$S_{SHG}(\omega,\tau) \propto \left| \int_{-\infty}^{\infty} E(t)E(t-\tau)e^{-i\omega t}dt \right|^2 \tag{2.12}$$

In this case the gate function is give by $E(t-\tau)$. Note that it is important that both the fundamental NIR pulse and the generated second harmonic pulse are traveling in the same medium with the same group velocity in order for them to constructively interfere. Since both have different frequencies, hence different dispersion, this condition is only fulfilled in a birefringent nonlinear crystals where one can find an angle that enables the refractive index to match in both polarizations. This is usually a limiting factor for the SHG FROGs which is avoided in TG FROGs since the phase matching is always satisfied due to the fact that both the fundamental and the transient signal have the same wavelength and this enables measurement of very short pulses in the order of few femtoseconds due to the large spectral bandwidth [16]. In a TG measurement, a time dependent modulation of the refractive index is created in a non linear medium via Kerr effect when two synchronous beams are focused onto this medium. A third beam having a delay τ with respect to the other two beams is then diffracted off the grating created by the modulation of the refractive index. The spectrogram of a TG FROG is defined as follows:

$$S_{TG}(\omega,\tau) \propto \left| \int_{-\infty}^{\infty} E(t)|E(t-\tau)|^2 e^{-i\omega t}dt \right|^2 \tag{2.13}$$

Regardless of the FROG measurement used, SHG or TG, one needs to retrieve the electric field of the pulse to extract the useful information embodied in the measured spectrogram $S(\omega,\tau)$. To do so, we use an iteration procedure where we start with an initial guess of the spectrogram and try to fit the waveform then we use the mismatch to improve the guess until we reach to a guess which yield a relatively small mismatch. Figure 2.3 shows a measured and retrieved TG FROG spectrogram together with the retrieved spectral and time domains of the few-femtosecond NIR pulse in FP3 laser system (described thoroughly in 2.2.1).

XUV characterization by streaking

In order to characterize the XUV pulses, it is not possible to use nonlinear processes, as in the case of ultrafast NIR pulses, since these XUV pulses have very low energy due to the low efficiency of the HHG spectrum at such energies and in addition to this, there is no nonlinear medium which is nonabsorbent at the XUV pulses energies. An alternative to this is to perform a pump-probe experiment where we use the XUV pulse to ionize an atom and then we probe this photoionized electron with a synchronized NIR pulse [17]. This cross-correlation between

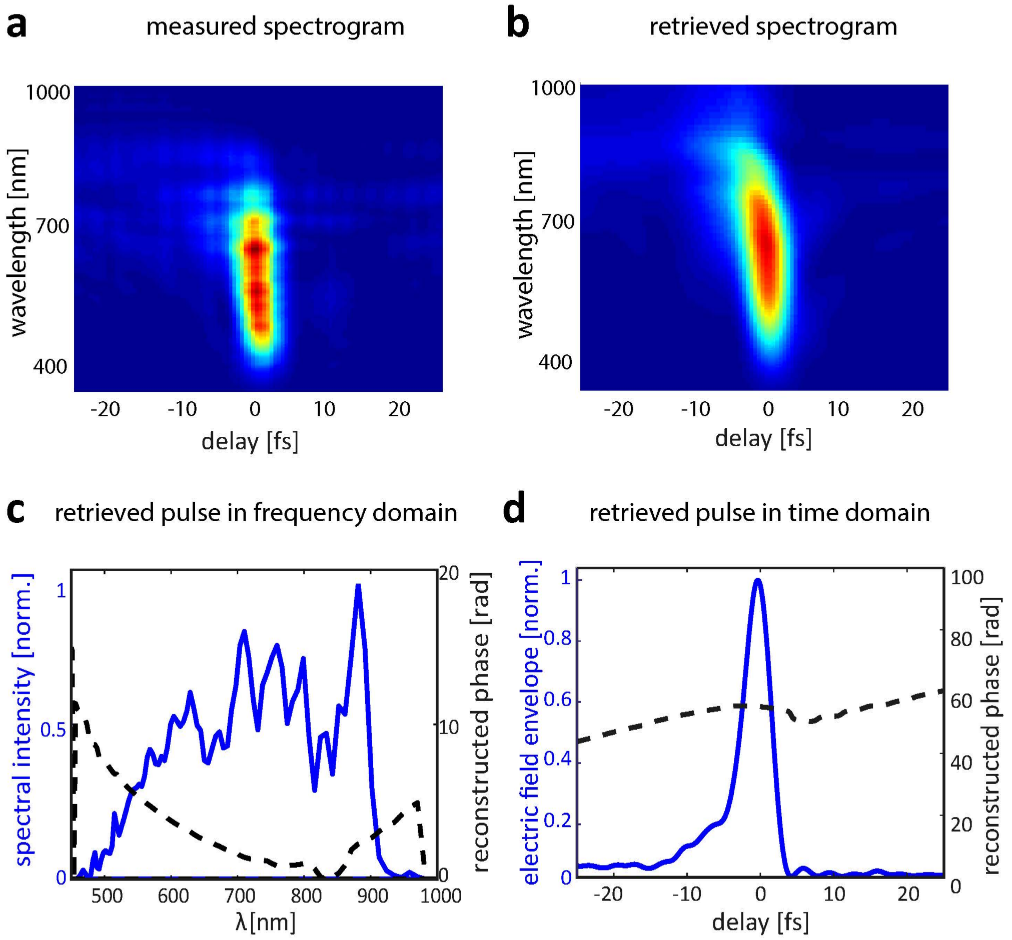

Figure 2.3: (a) measured and (b) retrieved transient grating FROG trace of a near 4 fs NIR pulse produced in FP3. (c) and (d) Retrieval of the electric field strength in the spectral and temporal domains respectively. Courtesy of A. Sommer

the two pulses presents a streaking trace which can be used to temporally characterize the two pulses. A possible way to achieve autocorrelation of XUV pulses is to use two-photon-absorption induced coulomb explosion [18]. In a two-photon two-color ionization measurement, the intensity of the side bands induced by the laser is a function of the spectral amplitude and the phase of the adjacent contributing harmonics. This enables us to measure the relative phase between neighboring individual XUV pulses in a pulse train [19, 20]. Unfortunately, this approach provides only narrow spectral and hence long temporal phase information therefore, we use the attosecond streak camera as an alternative approach to fully characterize an isolated XUV attosecond pulses.

XUV attosecond pulses are temporally synchronized with the NIR laser pulse as dictated by the phase matching condition of the HHG process, streaking uses this fact by combining the two beams in a single experiment [21–23]. The idea is old and it was utilized by E. Goulielmakis et al. where a streak camera was used to study ultrashort pulses in the picosecond regime [24]. The idea was to first ionize a medium by a short pulse, which is the pulse to be studied, then the ionized electrons pass through a rapidly varying electric field perpendicular to the direction of motion of the electrons. The electrons path will be dressed by the varying electric field forming a streaking trace on a camera screen which records the spatially altered spatial distribution of the electrons, basically this is the similar to the oscilloscope. The temporal profile can be fully recovered out of the streaking trace given that we know the temporal profile of the electric field. In the attosecond streaking experiment, we use the same principle where the short pulse to be studied is the XUV pulse and the streaking field is the NIR laser pulse. However, in this case a time resolution down to tens of attosecond can be reached rather than just picoseconds. When an XUV pulse hits a gaseous target, a photoelectron is released if the XUV pulse energy exceeds the ionization energy of the gas atoms. These photoelectrons will bear the same temporal profile as the XUV pulse which has ionized them. After they are released, these electrons passes through the synchronized NIR laser field at different instants determined by the delay τ introduced between them. The attosecond trace is formed by scanning the delay τ between the XUV and NIR pulses. We will use now a classical picture to illustrate the streaking, and for the sake of simplification we will use the atomic units, i.e. $|e| = \hbar = m_e = 1$, and we will also assume a linearly polarized NIR laser pulse. After these consideration, we will have the equation of motion of the photoelectron as follows:

$$\ddot{x} = -E_L(t) \tag{2.14}$$

where x is the position of the photoelectron in the direction of the polarization of the NIR streaking field. The next step is to integrate over the delay τ between

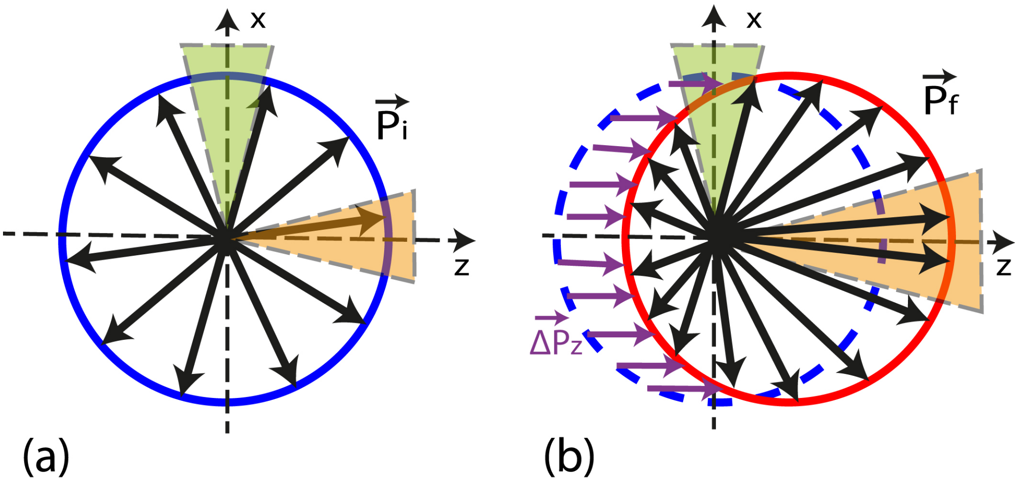

Figure 2.4: Photoelectron's momentum before (a) and after (b) the NIR streaking shift Δp_z. The gray and blue cones shows the detection in the x and z direction respectively

the two pulses, and this yields:

$$\dot{x} = -\int_{t_0}^{t} E_L(\tau)d\tau = v(t_0) + A_L(t) - A_L(t_0) \tag{2.15}$$

where A_L is the vector potential of the NIR laser field. With $A_L(t)$ being zero since we measure until the pulse is totally gone, equation (15) can be rewritten as follows:

$$\dot{x} = v(t_0) - A_L(t_0) \tag{2.16}$$

According to this equation, streaking determines the vector potential of the NIR pulse $A_L(t)$ rather than the electric field $E_L(t)$ itself as explained in [25].

Figure 2.4(a, b) shows an intuitive picture that describes qualitatively streaking along the direction of the detector, it shows that the the streaking trace follows indeed the vector potential of the NIR laser field. If the polarization of the NIR field is orthogonal to the detector, streaking is called transverse streaking and in this case the spectra are shifted to lower energies always. It is worth mentioning that our detector measure the time of flight of the photoelectrons which is easily translated into momentum. On the other hand, Figure 2.5 shows a measured spectrogram at our laboratories, where neon 2p electrons were photoemitted and streaked in the parallel polarization scheme. We see that the photoelectron line is shifted to lower and higher energies rather than being shifted to only lower energies as in the case of perpendicular streaking.

For the sake of simplicity, we made previously an assumption of a very short XUV pulse with respect to the NIR laser pulse which is not exactly the case. As a matter of fact, initial kinetic energy of the photoelectrons depends on the instantaneous frequency of the XUV pulse as the photoionization is happening

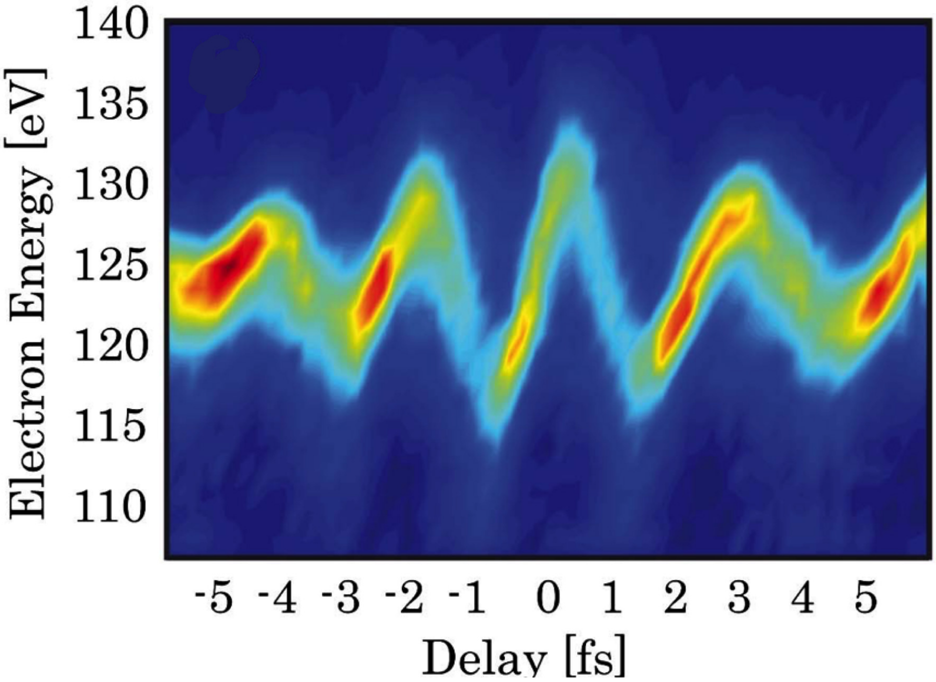

Figure 2.5: Streaking spectrogram measured in our laboratory showing the 2p photoelectron Neon line streaked in the parallel polarization scheme

over the whole XUV which is far from being an instant event. As a result, one could extract a lot of useful information if such details were included in the retrieval process. If the trailing edge of the XUV pulse has a higher frequency than the leading one, then the trailing photoelectrons having the higher kinetic energy will be decelerated while the leading photoelectrons of lower kinetic energy will be accelerated at the rising slope of the vector potential zero-crossing of the temporal center of the XUV pulse. We end up, in this case, with a narrow spectrum. On the other hand, if this happened at the falling slope of the zero-crossing we will observe a broadening of the spectrum according to [26].

In order to extract the delay from the streaking spectrogram, we use the center of energy method (COE) where the algorithms undergoes a Gaussian fit or uses the first moment analysis in order to find the center of energy of the spectral line for each delay step [27]. The algorithm fits the waveform $S(\tau)$ to the data that have the shape of:

$$S(\tau) = S_0 e^{-4\ln 2((\tau+\Delta\tau)/\tau_L)^2} \sin\left(\omega_L(\tau+\Delta\tau)+\phi_{CE}\right) \tag{2.17}$$

where τ_L and ω_L are the NIR streaking pulse length and frequency respectively, S_0 is its amplitude and ϕ_{CE} is the carrier envelope phase. On the other hand, $\Delta\tau$ is the difference in delay between the different photolines. As it is clear, the

COE method does not give information about the XUV pulse temporal properties while the TDSE does give such information in addition to other physical parameters with the cost of much more complex algorithm. In the TDSE algorithm, we use the single active electron picture, in addition to the first order perturbation theory, in order to represent the photoelectrons ionized by the XUV pulse. When the photoelectrons have small relative bandwidths, TDSE requires that the transition dipole matrix elements to be constant over the range of the experiment. Based on this, we use the parameters of the NIR and XUV pulses to construct the transition dipole matrix under the assumption that the final kinetic energy of the photoelectrons is greater than the ionization energy required to release these photoelectrons from the parent atom. TDSE makes a first guess for the input values using the some parameters of the XUV and NIR pulses, and then it iterates this guess in order to fit it to the spectrogram with a minimum error [28].

2.2 Equipment

2.2.1 The laser system

In the course of this thesis, two laser systems have been used to generate a few-cycle femtosecond NIR lase pulses FP2 and FP3 located in the Lab of attosecond science at Max-Planck Institute for Quantum Optics in Garching near Munich. Both Laser systems are basically identical, I will present briefly FP3 depicted in Figure 2.6 since it contains an additional amplification stage called the Booster, for more detailed information please refer to [29]

The Oscillator

It is a ker-lens mode-locked Titanium doped Sapphire (Ti:Sa) oscillator from Femtolasers Rainbow. This oscillator operates at 78 MHz repetition rate and produces $\approx 6fs$ pulses with an energy of $\approx 3nJ$. [30, 31]. We use a continuous wave (cw) pump laser (Verdi V6, Coherent Inc.) with central wavelength at 532 nm which passes through an acousto-optic modulator (AOM) in order to modulate its power. The spectral bandwidth of the produced pulses ranges between 700 nm and 1000 nm, this is possible due to the dispersive mirror design which compensates for the intra-cavity dispersion. Different frequency generation (DFG) takes place by the focusing of the pulses into a periodically poled magnesium oxide doped by lithium niobate (PP-MgO:LN). In the overlap region between the fundamental laser pulse and the DFG pulse, we use an IR photodiode and a spectrum analyzer to detect the CEP dependent f-to-0 interference beat signal which will serve as a monitor signal in the fast-feedback CEP stabilization loop discussed in details in [32, 33].

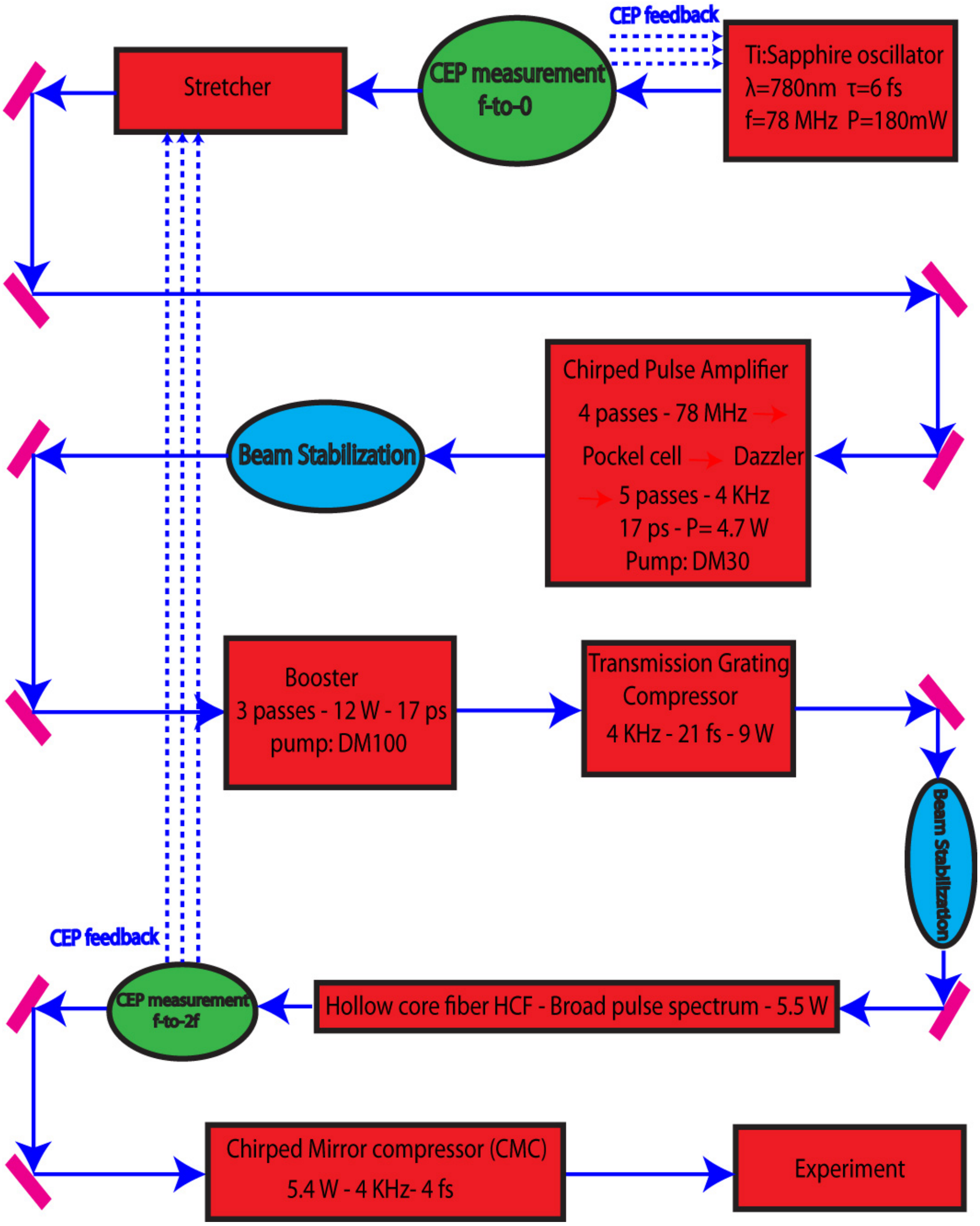

Figure 2.6: FP3 laser setup in MPQ. It consists of an oscillator, two amplification stages: CPA and booster, a hollow core fiber and a chirped mirror compressor (CPC)

The Chirped Pulse Amplification Stage (CPA)

The first amplification stage of FP3 system, CPA, uses the chirped pulse amplification scheme discussed thoroughly in [34]. It is a nine-pass amplifier which utilizes a Ti:Sa crystal which is kept at a temperature of $174K$ to minimize thermal lensing effects and a pump laser that produces a 300 ns, 532 nm pulses at 32 W (Photonics Industries, DM 30). Before entering the CPA, the fundamental laser pulse passes twice through a block of SF57 glass of length $13.5cm$. The later step is extremely important because it stretches the pulse to around $17ps$ ($1ps = 10^{12}s$) to avoid damaging the CPA crystal. In order to reduce the repetition rate down to 4 KHz, a Pockel cell is used as a pulse picker after the fourth pass. A programmable dispersive spectral shaper, called dazzler (from Fastlite), is used to reduce the spectral amplitude in the center compared to the wings of the gain window. The later step is extremely important to avoid gain narrowing and also to optimize the amplification in the next five passes. As a matter of fact, the dazzler can also be used to alternate the CEP of subsequent laser pulses by π or another desired value, this will turn out to be very beneficial when we perform the so-called differential streaking experiments. After completing the nine passes, the pulses are amplified up to $1.1mJ$ and then directed to the second amplification stage known as the booster.

The Booster

In this stage, a Ti:Sa multipass is used also but this time pumped with two mode-locked $532nm$ pump lasers from Thales ETNA HP. However, the booster is a three multipass system that has an amplification factor around three. In order to further reduce thermal lensing, thus improve the beam mode profile, the crystal is cooled down to $58K$ via cryogenically cooled setup. Moreover, the focusing in the booster is made very loose to avoid crystal damages. This comes with a price of making the refocusing into the crystal highly challenging, and one way to overcome this is to use a telescope before the booster which can easily alter the beam diameter and divergence. After the third pass, the booster can manage to boost the pulse energy up to 3 mJ.

Super Continuum Generation

After the booster, a transmission grating compressor with 86% transmission efficiency is used to recompress the pulse [35]. At this stage, the dazzler is used again to compensate the higher order chirp. For this, we use a second order FROG which is placed after the compressor and we feed the dazzler with the spectral phase extracted from the FROG measurement. Usually, few iterations are needed to reach a compressed pulse. A this stage, the near-Fourier limit pulse

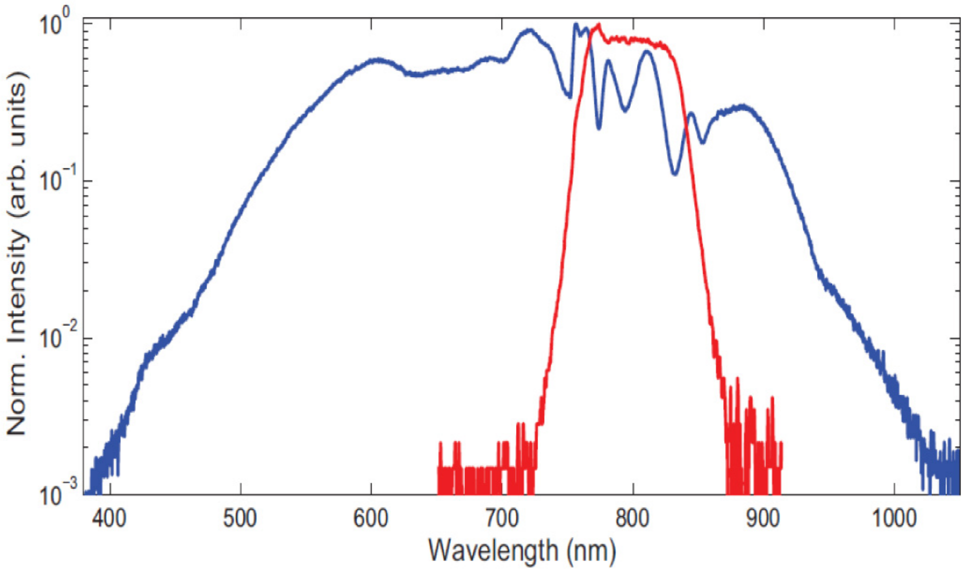

Figure 2.7: Laser spectrum measured before (red line) and after (blue line) spectral broadening in the hollow-core fiber filled with neon [36]

is far away from being the needed few cycle pulse. For this, the pulse spectrum is broadened due to self phase modulation (SPM) to produce a super continuum in Neon, or Helium, filled hollow core fiber (HCF). A persistent problem of using the HCF was the filamentation at the exit of the fiber due to the higher pulse energy and high gas pressure, this problem also ruins the beam profile. To avoid this, a differentially pumped fiber was installed so that we have now much lower gas pressure at the fiber entrance and exit. The spectrum then stretches from $450nm$ up to $1050nm$ which is a good broadening to have a Fourier limit pulse of few femtosecond. The new spectrum spans an octave enabling f-to-2f CEP detection which is then fed to a piezo prism in front of the CPA in order to stabilize the phase, this is called the slow loop stabilization stage and it will be discussed thoroughly in the next section. After this, the compression of the pulse is done via chirped mirror compressor (PC5). In order to check the compression done by PC5, we use a TG FROG as a diagnostic tool to determine the temporal and spectral profile of the pulses, as seen in Figure 2.7. Usually, we end up with a $\sim 4fs$ pulses, having an energy around $1.35mJ$.

2.2.2 Carrier-Envelope Phase Stabilization

The shorter the laser pulse gets, the more important is its CEP. Stabilization of the Carrier-Envelope phase (CEP) is beneficial especially in the HHG process where it is needed to reach an isolated attosecond XUV pulse. The mode-locked laser oscillator yields a train of equidistant frequency component of separation

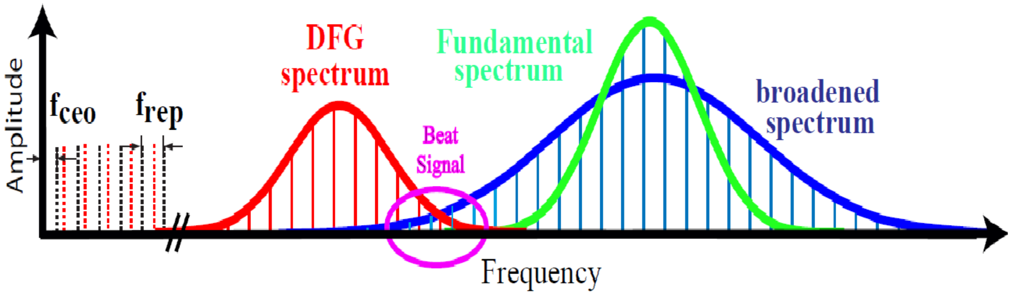

Figure 2.8: Sketch of the beat signal between the broadened fundamental spectrum and the DFG generated spectrum

frequency equals the repetition rate of the laser ν_{rep}. This is called a frequency comb [37]. For each round trip in the cavity, CEP difference $\Delta\Phi$ between consecutive pulses accumulates basically due to the fluctuations of the pulse parameters which lead finally to phase jitter or drift between the pulses due to non-linear changes [38]. This causes an offset, carrier-envelope- offset frequency ν_{CEO}, between the comb lines in the frequency domain, this offset equals an integer multiples of ν_{rep}. In order to stabilize the CEP, one needs to measure and stabilize ν_{CEO}. In the time domain, the frequency comb is formed of a train of pulses having an offset influenced by nonlinear effects [39] rather than equidistant frequency components. In another words, the energy and pointing fluctuations of the laser beam contribute into the CEP jitter. In order to control these changes, two stabiliyation schemes are used. The first stage is a $f-to-0$ scheme used to stabilize the oscillator CEP fluctuations. The beam coming from the oscillator is focused into a periodically poled magnesium-oxide doped lithium niobate (PP-MgO:LN) non-linear crystal. Due to self phase modulation (SPM), the spectrum examines broadening. In addition to this, difference frequency generation (DFG) takes place and a second spectrum is generated as seen in figure 2.7.

The generated second spectrum has a $\nu_{CEO}=0$ as in the following equations:

$$\nu_{DFG}=(m\nu_{rep}+\nu_{CEO})-(n\nu_{rep}+\nu_{CEO})=(m-n)\nu_{rep} \tag{2.18}$$

As illustrated in Figure 2.8, the fundamental and generated spectra are mixed with a temporal delay to yield a beat signal which have a beat frequency ν_{beat} gives as follows:

$$\nu_{beat}=k\nu_{rep}+\nu_{CEO}-(m-n)\nu_{rep}=\nu_{CEO} \tag{2.19}$$

The heterodyne beat signal is detected simultaneously by a spectrum analyzer and a photodiode and can be locked to an external radio-frequency reference by adjusting the power of the laser pump using an acousto-optic modulator (AOM) which diffracts part of the beam [40]. The AOM can diffract a desired amount of the pump due to the modification of its refractive index introduced by an oscillating sound wave.

Although being phase stabilized, the pulses encounters another source of instabilities when they pass through the chirped pulse amplifier (CPA) and the hollow core fiber (HCF) due to perturbations, therefore a second CEP stabilization stage is necessary and is installed after the HCF. In this stage, we use a $f - to - 2f$ scheme since we have a relatively broad spectrum after the HCF. When the pulse passes through a nonlinear crystal (β-barium-borate), its lower frequency components are converted by the second harmonic generation (SHG) and then mixed with the higher tail of the fundamental spectrum as seen in Figure 2.8. This yields a beating signal which is used to lock the CEP using a piezo actuated glass wedges. This is called the slow stabilization loop compared to the first loop which is called the fast stabilization loop.

2.2.3 Experimental Setup: Beamline

In the course of work in this thesis, experiments were performed at the Laboratory for Attosecond Physics (LAP) at the Max-Planck-Institute of Quantum Optics in Garching. Using one of the two Ti:Sa based laser sources for attosecond streaking (FP2 and FP3), the second being thoroughly described previously. The experiments were performed mainly at the surface science AS3 Beamline but also at the interferometric Beamline AS2.

The surface Science Beamline AS3

The NIR-XUV Beamline

Ultra high vacuum conditions are needed in the case of chambers used in surface science photoemission experiments, i.e. the pressure should be in the range of 5×10^{-11}mbar. This is an extremely critical task since the pressure in the HHG chamber is usually around 10^{-2} mbar. Figure 2.9 depicts several vacuum chambers and stages that the pulses pass through before getting into the experimental chamber. The beam is guided to the HHG chamber by a set of silver mirrors and then focused with a concave silver mirror (ROC=-1100 mm) into a movable gas target backfilled with neon where the high harmonics are generated through HHG process. The gas target is made of a thin tungsten or ceramic tube with a drilled hole of diameter around 250 μm, the propagation distance inside the tube is minimized to ensure a better phase matching condition [41], see Figure 2.9.

In order to maximize the XUV flux in the cut-off region of the HHG spectrum, one has to optimize the target position, focus position and the aperture opening. The HHG chamber is pumped by a 600 l turbo molecular pump (Leybold MAG W 600) to ensure that the pressure remains in the low enough to avoid the re-absorption of the XUV [42]. A skimmer (S) together with a 200 l turbo pump are used as a second differential stage to further decrease the pressure before the pulse reach the experimental chamber. In addition to this pump, another 300 l turbo pump is used in the filter chamber, which we will talk about it in the next paragraph, to get the pressure down to 10^{-9} mbar. Just before entering the experimental chamber, the pulse enters a region pumped by a 400 l turbo pump to achieve a pressure lower than $10^{-}10$ mbar. Before reaching the experimental chamber, the XUV pulses can be reflected by a golden-palladium mirror (M2) into a gold-coated grating (G) and then dispersed onto a MCP detector. This enables us to examine the spectrum of the XUV pulses and ensure that we have the cut-off at the right energy range.

The filter assembly consists of a metallic filter glued in the center of a NIR-transparent nitrocellulose pellicle. Either aluminum (Al) or zirconium (Zr) are used as a metallic filter to absorb the NIR in the inner part ensuring that the central part of the beam consists only from XUV while the outer part consists from the NIR laser pulse only, see Figure 2.10.

At this point, the annular NIR beam and the co-propagating central XUV beam enters the experimental station where they are focused by the double mirror assembly into the surface of the sample to be measured as depicted in Figure 2.10. The double mirror assembly consists of two coaxial mirrors, the inner one is coated by a convenient multilayer structure to reflect the XUV pulses at a desired energy and with a designed bandwidth [43, 44]. On the other hand, the outer part of the double mirror assembly consists ofa mirror which reflects the NIR with a reflectivity of around 20%. The double mirror assembly is mounted on a piezo stage from Nanomotion which ensures the ability to put the two mirrors in temporal overlap. The delay between the two beams is introduced by the translational stage of the XUV mirror which is mounted on a closed loop piezo-electric transducer (PI Hera 621, customized for UHV). The stage can move along a 100 μm range with a resolution of 0.2 nm which corresponds to a temporal delay resolution of 1.3 asec.

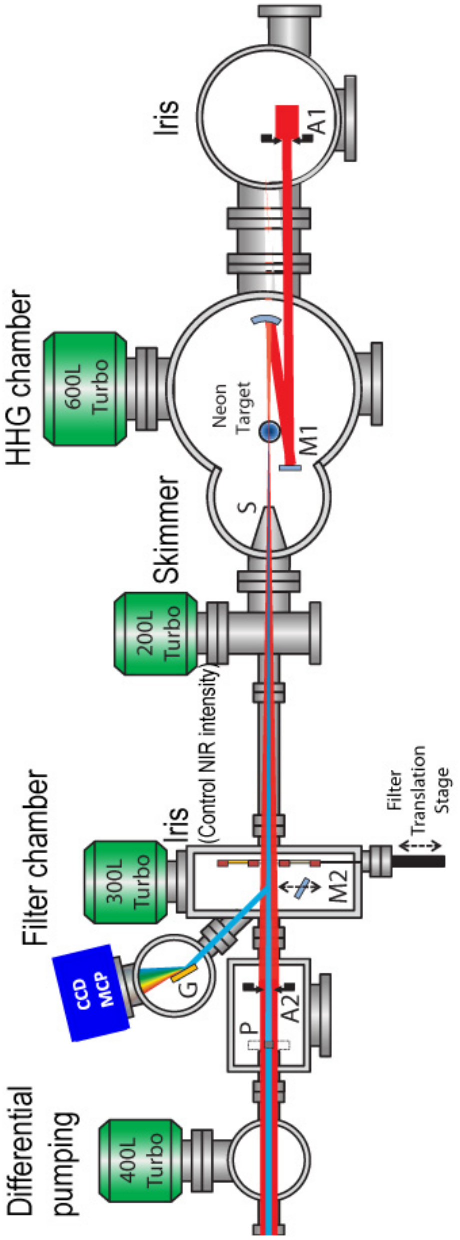

Figure 2.9: Sketch of the collinear generation of few-fs NIR and sub-fs XUV pulses by high-harmonic generation in AS3 Beamline. The transition from rough vacuum in the HHG chamber to UHV in the experimental area is achieved by several differential pumping stages. Adapted from [42]

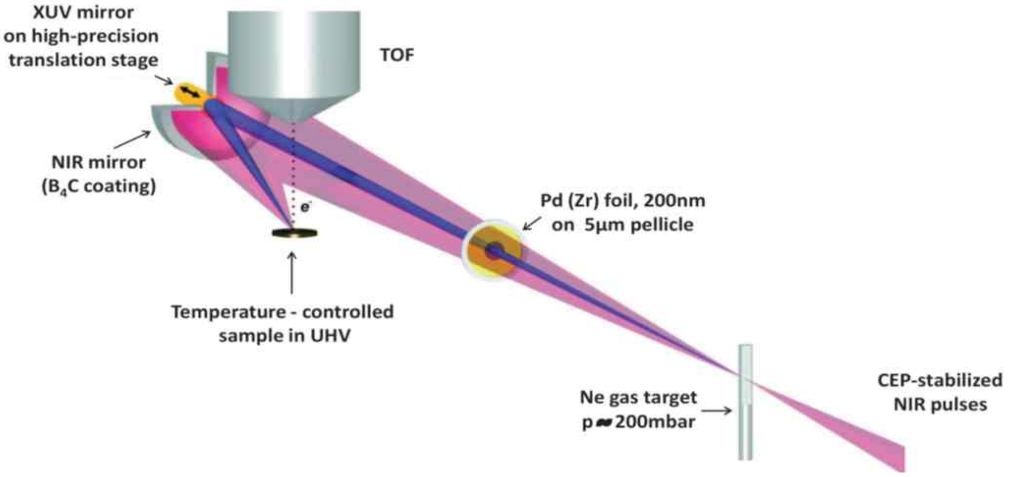

Figure 2.10: Overview of the AS3 setup used to isolate the copropagation NIR/XUV pulses via a metal filter glued on a NIR-transparent foil. The sketch shows also the translational motion of the XUV inner mirror at the axis of the NIR outer mirror [42]

The Preparation Chamber

AS3 beam line ends with two stainless steel chambers separated by a pneumatic gate valve. One is called the preparation chamber and is used to undertake cleaning, LEED measurements, annealing, etc. of the samples. The second one is the experimental chambers to which the sample is brought for photoelectric measurements after being prepared in the preparation chamber, see Figure 2.11.

Concerning the preparation chamber, the sample could be brought in front of each of the preparation stations by rotating the manipulator via a differentially pumped rotary feed through [45]. The preparation chamber consists of several devices used for surface preparation such as a four-grid LEED system, an ion sputter gun, annealing mechanism, a kundsen-type effusion cell and a gas dosing system used for spattering of the sample surface. The samples are mounted on a manipulator which can be moved in the three dimensions. It is also pumped differentially at a feed through to enable the rotational motion. We can measure the sample temperature by a C-type thermocouple welded to the edges of the sample, the sample holder provides the reference measurement of the thermocouple. This thermocouple connection enables a temperature reading up to 2500 K. Annealing of the sample is typically done as a common sample surface cleaning procedure and for this a radiative filament is used to achieve the desired temperatures.

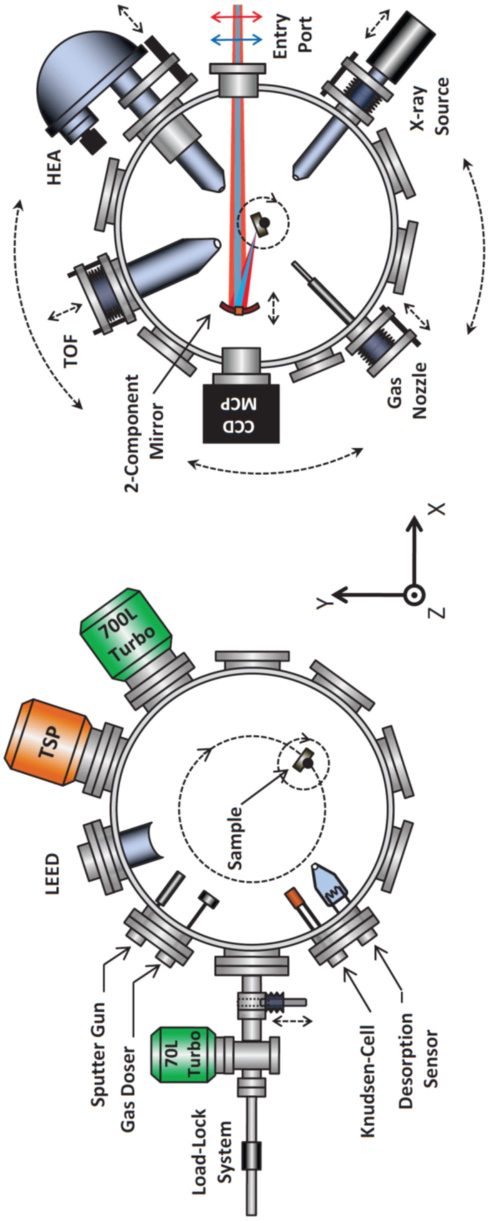

Figure 2.11: Sketch showing a cross-sectional view of the experimental (top) and the preparational (bottom) chambers at AS3 beamline. The sketch shows the various tools and equipment of both chambers [42]

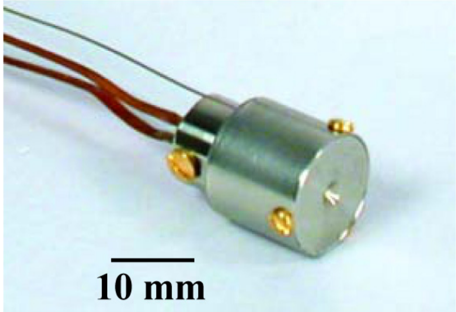

Figure 2.12: Photo of an unmounted electron flood gun (FRA-2X-2)

Installation of pulsed electron flood gun

While measuring some wide bandgap materials, we observed a discharging effect where the surface is totally depleted from electrons due to the photoemission from surfaces which are not conducting.

In order to overcome this and enable our experimental chamber to be able to undertake successful streaking experiments on wide bandgap materials, we installed a pulsed electron flood gun which is UHV compatible (FRA-2X-2, from Kimball Physics inc.), see Figure 2.12. The electron flood gun delivers an electron pulsed beam up to $5KHz$, the pulsing of the electron beam is done via a dual grid supply which needs a TTL control signal as an input. The electron pulse length can go down to $2\mu m$ with a rise/fall time of around $500ns$, this is important to make sure that the sample surface is recovered before the arrival of the next pulse. The electron energy ranges from 5 to $1000eV$ and the beam current ranges from $1nA$ up to $400\mu A$.

The beam spot on the sample has a Gaussian profile and has an adjustable size from 5 to $15mm$ which is small enough to fit the sample surface just under the TOF. The electron flood gun has a relatively small size as seen in Figure 2.12, and is mounted on a special designed arm to be able to insert it into the experimental chamber, as seen in Figure 2.13. This arm ensures the flood gun is close enough to the sample surface to have a reasonable spot size onto the sample surface. The flood gun is mounted on a movable stage which enables the position adjustment in the three dimensions. Figure 2.14 shows a picture of the experimental chamber where the position of the installed flood gun is shown alongside with the detector and the sample position.

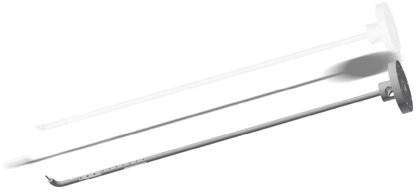

Figure 2.13: Sketch of the electron flood gun mounted on the mounting arm

The Experimental Chamber

After the sample is prepared in the preparation chamber, its is moved to the experimental chamber where the photoionization spectroscopic measurements take place. Two differentially pumped feedthroughs allow the rotation of the experimental chamber around the z-axis in order to bring it to a desired position, in addition to this the sample itself is rotated to align the sample surface parallel to the detector surface. We use a time-of-flight (TOF) spectrometer (Stefan Kasedorf, Geraete fuer Forschung und Industrie) as an electron detector in the course of streaking experiments where the time needed by an electron to reach the detector is used to calculate its energy. There are several reasons to perform streaking experiments with the TOF, most important is its efficiency which is extremely critical due to the relatively low XUV flux and also low laser repetition rate (3 and 4 KHz). In addition to this, the experimental chamber consists of a hemispherical analyzer (HSA) (Specs Phoibos 100) and a X-ray source which has a Mg\Al-twin anode for sample characterization with standard X-ray photoelectron spectroscopy. In order to optimize the XUV flux and target position, the XUV beam is guided to the CCD camera in the experimental chamber. After optimization, the experimental chamber is rotated in order for the NIR-XUV co-propagating beams to be reflected onto the sample surface as seen in Figure 2.11 . The double mirror stack is changed every now and then according to the desired multilayer XUV mirror to be used. In order to do this, the double mirror stack can be retracted away from the experimental chamber into a load lock to avoid breaking the highly demanding ultra UHV pressure every time the double mirror is changed.

Both chambers consist of liquid nitrogen cooled titanium sublimation pumps (TSP), they are used to further enhance the pressure inside chambers. A quadrupole mass analyzer is used in the preparation chamber and experimental chamber as well, they are used to detect the residual gas compositions in the chamber and this is extremely important in the case of

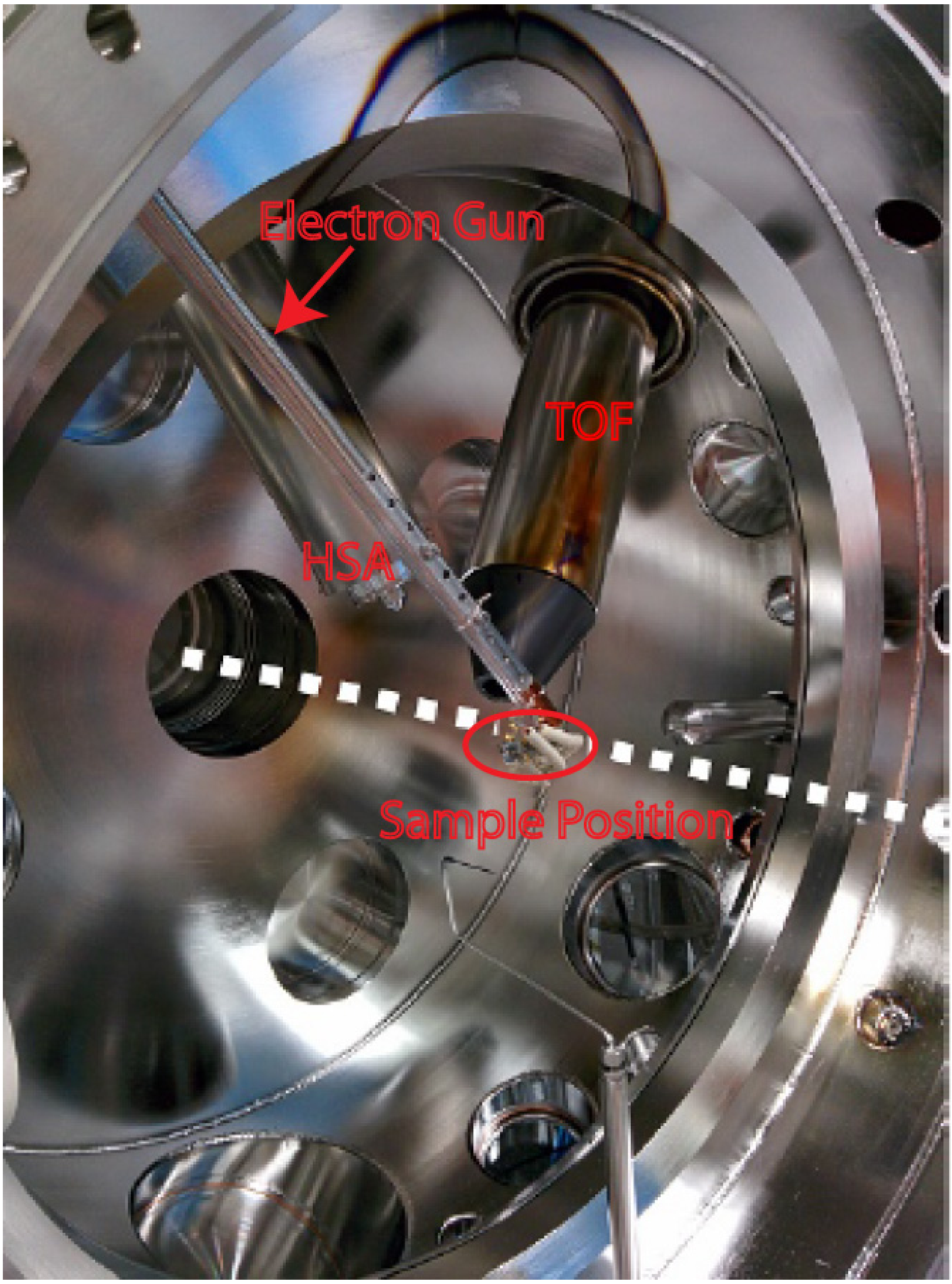

Figure 2.14: Side view of AS3 experimental chamber. It shows the electron gun, TOF, HSA, and the sample position. The dashed red line shows the translation axis along which the sample is inserted into the measurement position

sample annealing in the preparation chamber. A sub 10^{-11} $mbar$ pressure could be reached after baking out and switching on the TSPs, and this is appropriate pressure to perform photoionization experiments. In order to ensure the temporal and spatial overlap between the two mirrors of the double mirror, we block the XUV beam and we sent a NIR beam instead of it. We reflects both NIR beams, reflected from the outer and inner mirrors, out side the chamber onto an external CCD camera. We optimize the outer mirror position so that we achieve a well symmetric interference fringes on the CCD camera which confirm the desired temporal and spatial overlap.

Chapter 3

Rabi oscillations in Bandgap materials

Rabi oscillations in bandgap materials opens the door towards electric excitations in the attosecond regime compared to the current picosecond limit. Understanding Rabi oscillations both in semi-classical and quantum mechanical images is discussed in this chapter, this is done in the scope of the study on interactions of strong electromagnetic fields with semiconductors. Furthermore, we will explore the possible semiconductors that can be good candidates for the photoelectron experiments. In addition to this, We discuss the choice of GaAs as a preferable sample, mainly due to its bandgap energy E_g and the availability of the required preparation technique at $AS3$ beamline.

3.1 Introduction

Rabi flopping is a well known phenomenon, it takes place when we illuminate a two-level system with a constant light intensity which force the inversion to oscillate periodically [46]. Researchers reported seeing a signature of Rabi oscillations of period that ranges between $50fs$ and $1ps$ in many occasions [47]. Things will start to look very interesting if a light field is used whose intensity is high enough for the Rabi oscillations to become comparable with one cycle of the used electromagnetic field. For the case of GaAs, whose $E_g = 1.42eV$, this would mean that the duration of one cycle of light should be close to $\frac{\hbar}{E_g} = 2.9fs$. This questions was investigated theoretically by Hughes [48] where he suggested the failure of the area theorem to predict a nonlinear phenomenon which he called Carrier wave Rabi oscillations. In an experiment, one needs to have both intensity and electronic coherence [1], this implies that we need very short

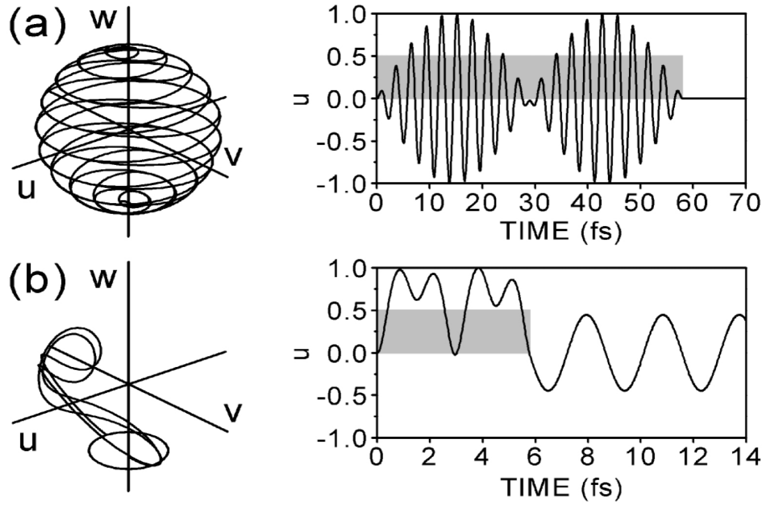

Figure 3.1: (a) Sketch of the Bloch vector of the conventional Rabi oscillations for a pulse of duration 20 optical cycles. Envelope pulse area is $\Theta=2\pi$. (b) Sketch of the Bloch vector of the carrier-wave Rabi oscillations for a pulse of duration 2 optical cycles and $\Theta=4\pi$. u and v are the real and imaginary parts of the optical polarization respectively while w is the inversion of the two level system [1]

pulses to successfully perform an experiment. Bloch sphere is schematically depicted in Figure 3.1(a), on top of it plotted also the Rabi flopping in the case of the period of these oscillations being considerably longer than the period of light.

In Figure 3.1, the real and imaginary parts of the optical polarization of light is defined by u and ν respectively, while the inversion of the two level system is defined by w. In the case of a square-shaped pulse which has an envelope area $\Theta = 2\pi$, the Bloch vector spirals up from the south pole to the north pole and then back to the south pole. This means that all the electrons which started from the valence band, will be excited to the conduction band, this is seen as a modulation of u. On the other hand, if we have a shorter pulse which have an envelope area $\Theta = 4\pi$ then the Bloch vector will not go back to the south pole ass seen in Figure 3.1(b). This is a failure of the area theorem in nonlinear optics. In addition to this failure, we observe distortion in the optical polarization vector. This will cause the generation of high harmonics.

3.2 Semi-classical two level model

To describe bandgap materials, the two level system is used to simplify the situation. It does not give a detailed solution, though it offers a windows into the behavior of the system. Figure 3.2 shows a sketch of a quantum mechanical two level system which is driven by an electromagnetic field of frequency ω. If we are in the near resonant case, then this would mean that there is a small mismatch, called the detuning value Δ, between the light energy $\hbar\omega$ and the bandgap energy E_g. The transition matrix, i.e the population, oscillates between the two quantum energy eigenstates $|1\rangle$ and $|2\rangle$ of the system giving rise to the so called Rabi oscillations.

In the absence of the electromagnetic field, the system rests in the initial state $|1\rangle$ and its state is expressed by $|\psi(t)\rangle \propto e^{-it/\hbar}|1\rangle$ where the probability of occupying the initial state is 1. This is called the stationary state of the system. On the other hand, if we apply an electromagnetic field to this system, the eigenstate is a combination of the two states $|1\rangle$ and $|2\rangle$ of probabilities c_1 and c_2 respectively rather than being a single stationary state, i.e $|\psi\rangle = c_1|1\rangle + c_2|2\rangle$. The states of the system are coupled via the applied field. Using the two-component vector, the state of the system can be expressed as follows:

$$\psi = \begin{pmatrix} \langle 1|\psi\rangle \\ \langle 2|\psi\rangle \end{pmatrix} \tag{3.1}$$

In the case of a light field interaction with the two level system, the Hamiltonian of the system is given by $\hat{H} = \hat{H}_0 + \hat{H}_{int}$, where $\hat{H}_0$ is the Hamiltonian of the system in the stationary state and $\hat{H}_{int}$ is an energy perturbation which represents the interaction term between the field and the system which introduces a dipole moment between the two states $|1\rangle$ and $|2\rangle$. $\hat{H}_0$ is expressed as follows:

$$\hat{H}_0 = \begin{pmatrix} 0 & 0 \\ 0 & \omega_0 \end{pmatrix} \tag{3.2}$$

On the other hand, the perturbation $\hat{H}_{int}$ is given by:

$$\hat{H}_{int} = \hbar \begin{pmatrix} 0 & \Omega\cos(\omega t) \\ \Omega^* \cos(\omega t) & 0 \end{pmatrix} \tag{3.3}$$

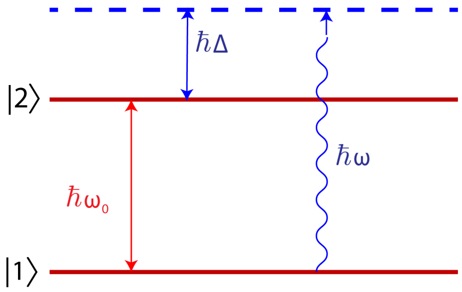

Figure 3.2: Sketch of a two level system. $\hbar\omega$ is the photon energy, $\hbar\omega_0$ is the bandgap energy, and $\hbar\Delta$ is the detuning factor

where the energy of the electromagnetic field is given by $\hbar\Omega$. The next step is to solve the Schrödinger equation in the interaction picture, i.e the time dependent part of the Hamiltonian $\hat{H}_{int}$ is expressed in the rotating frame. Combining the two equations (2) and (3), we get:

$$\hat{H} = \frac{\hbar}{2}\begin{pmatrix} 0 & \Omega(e^{i\omega t} + e^{-i\omega t}) \\ \Omega^*(e^{i\omega t} + e^{-i\omega t}) & 2\omega_0 \end{pmatrix} \tag{3.4}$$

next, for the sake of our calculations we define the operator H_1 as follows:

$$\hat{H}_1 = \begin{pmatrix} 0 & 0 \\ 0 & \omega \end{pmatrix} \tag{3.5}$$

substituting equation (5) in equation (4) in the rotating frame yields:

$$\hat{H} = e^{iH_1 t/\hbar}(\hat{H} - \hat{H}_1)e^{-iH_1 t/\hbar}). \tag{3.6}$$

we end up with the following expression:

$$\hat{H} = \frac{\hbar}{2}\begin{pmatrix} 0 & \Omega(1 + e^{-2i\omega t}) \\ \Omega^*(1 + e^{2i\omega t}) & 2\Delta \end{pmatrix} \tag{3.7}$$

If we ignore the terms that oscillate at twice the field frequency which is a consequence of rotating wave approximation, we can rewrite the previous equation as follows:

$$\hat{H} = \frac{\hbar}{2}\begin{pmatrix} 0 & \Omega \\ \Omega_* & -2\Delta \end{pmatrix} \tag{3.8}$$

The final step involves solving the time dependent Schrodinger equation in order to determine the time evolution of the states:

$$\frac{d|\psi\rangle}{dt} = -\frac{i}{\hbar}\hat{H}|\psi\rangle \tag{3.9}$$

and in the matrix form, it is written as follows:

$$\begin{pmatrix} \dot{c_1}(t) \\ \dot{c_2}(t) \end{pmatrix} = -\frac{i}{\hbar}\begin{pmatrix} 0 & \Omega \\ \Omega_* & -2\Delta \end{pmatrix}\begin{pmatrix} c_1(t) \\ c_2(t) \end{pmatrix} \tag{3.10}$$

Solving the differential equation will yield the following relation:

$$\begin{pmatrix} c_1(t) \\ c_2(t) \end{pmatrix} = e^{\frac{it\Delta}{2}}\begin{pmatrix} \cos\left(\frac{\Omega_R t}{2}\right) - i\frac{\Delta}{\Omega_R}\sin\left(\frac{\Omega_R t}{2}\right) \\ -i\frac{\Omega}{\Omega_R}\sin\left(\frac{\Omega_R t}{2}\right) \end{pmatrix} \tag{3.11}$$

where Ω_R is the Rabi frequency and defined as:

$$\Omega_R^2 = \Omega^2 + \Delta^2. \tag{3.12}$$

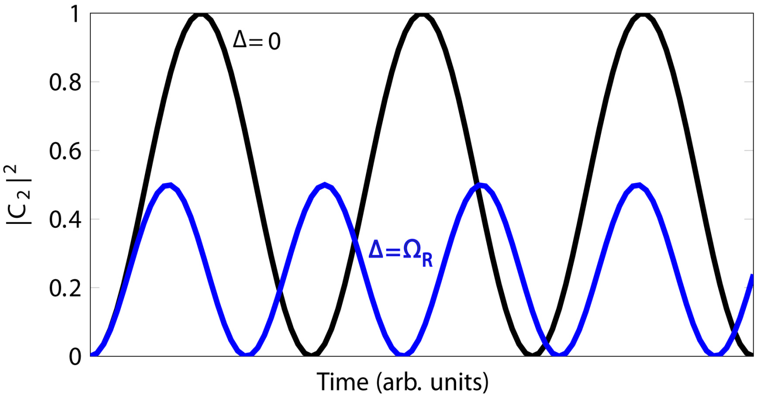

Figure 3.3: Oscillation of the carrier population between the levels in the case of a zero and non-zero detuning factor Δ. $|c_2(t)|^2$ is the probability of the system to be in the level $|2\rangle$

finally, the probability of the system to be in either of the states $|1\rangle$ or $|2\rangle$ is given by:

$$|c_1(t)|^2 = \frac{\Omega^2}{\Omega_R^2}\sin^2\left(\frac{\Omega_R t}{2}\right) \tag{3.13}$$

$$|c_2(t)|^2 = \frac{\Delta^2}{\Omega_R^2} + \frac{\Omega^2}{\Omega_R^2}\cos^2\left(\frac{\Omega_R t}{2}\right) \tag{3.14}$$

Figure 3.3 shows a simulation which explains the oscillation of the transition matrix in the case of a zero and non-zero detuning factor Δ. It is clear that only in the case of a zero Detuning factor we can populate and depopulate the whole electrons in the states.

3.3 Small bandgap materials

In order to maximize the chance of detecting a photoemission signature of Rabi oscillations, one should aim at direct bandgap materials since the condition of exciting a phonon for the sake of phase matching is not needed in the case of direct bandgap materials. In addition to this, one should also aim at a zero Detuning factor to be able to fully populate the conduction band. These are the main criteria which should be taken into consideration when searching for a good candidate for the measurement.

3.3.1 Examples of Rabi oscillation in bandgap materials

Rabi predicted the oscillations in a simple magnetic two level system, and instead of the current oscillations under the influence of an optical field, Rabi used an oscillating magnetic field [49]. Later, Y. S. Bai in [50] saw an oscillation in a simple optical two level system using nonlinear optics by fluorescence signal. They proved that optical oscillations are in principle identical to the previously predicted magnetic oscillations.

Coming to semiconductors, R. Binder et al. [51] illustrated that Rabi oscillations occur also in semiconductors where optical Bloch equations which contain additional exchange terms were modified. It was striking to see an excitation in [52] given that there was an absence of an upper limit of the excitation density and the carriers form a continuous set with momentum dependent detuning. Additionally, both the transition energy and Rabi frequency are normalized due to the excited carriers. It is worth mentioning that excited carriers in bands undergo Coulomb interaction which create an internal field that enhances Rabi oscillations by a factor of two [53] after being added to the external field. In fact, this is the reason of the renormalization of Rabi frequency and transition energy. On the other hand, in order to gate such excitations, one has to use a metrology of comparable time scale [54]. Given that the predicted dephasing time is in the order of hundreds of femtoseconds, this suggests the using of very short laser pulses with comparable pulse length.

There were various experimental efforts aiming at seeing Rabi flopping in semiconductors which would be measured as a density variation of occupation of valence and conduction band. Giessen et al. used a cross-correlation signal between a reference beam which was measured and a probe beam which was transmitted through CdSe sample, they were able to see flops in the density of carriers of CdSe. On the other hand, schülzgen et al. saw Rabi oscillations in sub picoseconds time regime [52]. They were the first to directly observe these oscillations. Figure 3.4 depicts the simulation of their experimental results where it shows clearly the flops, though not all the carriers go back to the valence band, mainly due to scattering in the conduction band.

Mücke et al. in 2001 saw Rabi oscillations in GaAs semiconductor in the femtosecond regime when they used intensities close to $10^{12} W/cm^2$ [55]. SWith such intensities, they observed a peak structure in the third harmonic which is a clear evidence of Rabi oscillations, see Figure 3.5.

3.3.2 Bandgap Materials Candidates

To observe Rabi oscillations in an experiment, metals are excluded as candidate materials. Rabi oscillations occur between two levels with a certain energy gap and this does not exist in metals where the conduction

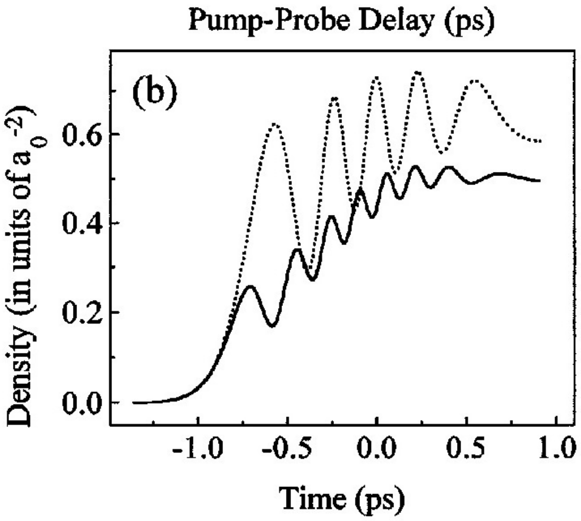

Figure 3.4: Theoretical calculation of the carrier density in the case of a 770 fs pulse with (solid line) and without (doted line) nonlinear Coulomb renormalization, as discussed throughly in the work of A. Schuelzgen et al. in [52].

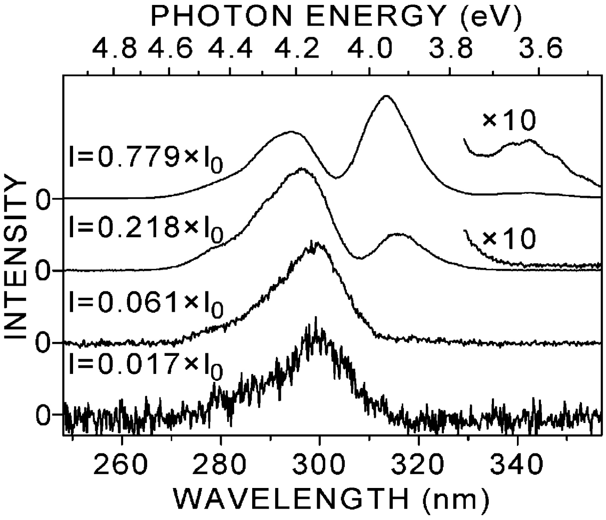

Figure 3.5: Experimental spectra of light emitted at the third harmonic in GaAs. The system is excited with a pulse of duration 5 fs [1]

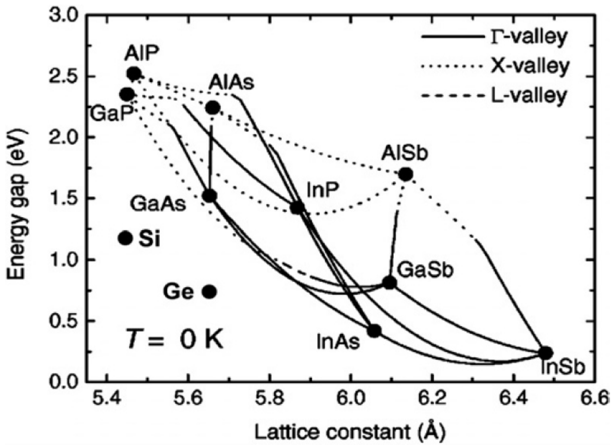

Figure 3.6: Sketch showing simultaneously the bandgap and lattice constants of different materials at $0K$ temperature. Nature of the bandgap is indicated by the line structure for the three cases:Γ, X, and L valleys. Th candidate material should have a direct semiconductor which has a bandgap around $1.4eV$ [57].

band is partially filled. So, semiconductors were chosen as better candidates as compared to metals.

The band structure of semiconductors offers the energy gap which separates two levels, conduction and valence band. So, Rabi oscillation could occur when the carriers oscillate between these two levels. Having the valence band completely filled, the velocity of the electrons is zero giving rise to a zero current [56]. This condition is applicable also in insulators, but the bandgap energy E_g of insulators is in the order of several eV while the laser field photons energy is around $1.5eV$ which means that direct absorption could not occur leaving the whole process highly inefficient. This would leave us with only semiconductors, whose E_g are comparable to the laser photon energy, as possible candidates.

Having limited ourself to semiconductors with bandgap energies in the order of $1.5eV$, Figure 3.6 depicts some of the semiconductors, from which we can choose possible material candidates for our experiment.

Among the materials shown in Figure 3.6, we should omit those which have bandgap energies lower than $1.2eV$ and higher than $1.7eV$ since between the laser energy lies between these two values. In addition to this, in the case of semiconductors of small bandgap energies, electrons are excited to the conduction level with different energies which boosts the scattering process between these electrons. The dephasing time of conduction band carriers are smaller than the time scale of Rabi oscillations [58] making the observation of Rabi oscillations in such semiconductor almost impossible.

Concerning small bandgap material, there is an additional problem connected to the signal to noise ratio [59]. This problem becomes remarkable due to the expected low excitation signal in addition to the relation between the signal $\Delta E_{excitation}$ and the bandgap energy which is explained in this relation:

$$\Delta E_{excitation} \geq x E_g \tag{3.15}$$

where $\Delta E_{excitation}$ is the energy of the expected excitation and x is the percentage of the excited electrons from level 1 to level 2.

Knowing that (3.15) is true for the simple two level system, still it gives a rough estimation of the possible signal to noise ration. Based on all the previous mentioned criteria, we limit ourselves to semiconductors of bandgap energies higher than $1.2eV$. An additional factor which should be taken into account is the detuning factor Δ discussed previously in 3.1. In order for the resonance to occur, and hence efficiency in the absorption process, one needs Δ to be set to zero. Having the center energy of our NIR laser field at around $1.58eV$, we should prefer semiconductors having a comparable E_g. Looking at Figure 3.6, we see that we have three possible candidates: GaAs, $Al_xGa_{1-x}As$ and InP. All of these three materials could be successfully grown using molecular beam epitaxy method (MBE) [60].

InP was excluded as a possible candidate for our experiment because it is almost impossible to have a good surface structure while growing it. This is not convenient since in surface science we probe basically only the very top layers in materials. On the other hand, growing $Al_xGa_{1-x}As$ is possible up to $x = 0.4$ while keeping a direct bandgap, hence it is in principle a good candidate for the measurement which will yield a bandgap energy between $1.42eV$ and $2.16eV$ depending on the alloy ration$x$ [61] and also in [17]. GaAs is a very good candidate since its bandgap energy, $E_g = 1.42eV$ matches the field photon energy and its has a direct bandgap. Moreover, Growing As-capped GaAs samples offers an experimental window into an oxidized free GaAs sample surface after appropriate treatment in our preparation chamber at AS3, therefore we did the measurements on As-capped GaAs samples grown at Walter-Schottky Institute (WSI) in Garching near München.

3.3.3 Properties of GaAs

In our measurement, we used (100) As-capped GaAs samples. These samples have direct band and a bandgap energy of $1.42eV$ at Γ-point as seen in Figure 3.7.

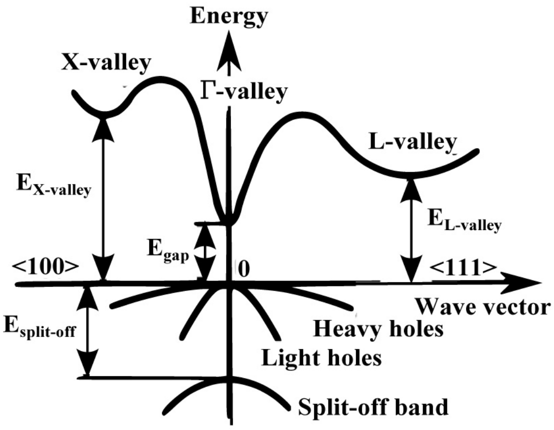

Figure 3.7: Band structure of GaAs adapted from [62]. It shows that GaAs is a direct bandgap material with $E_g = 1.42eV$

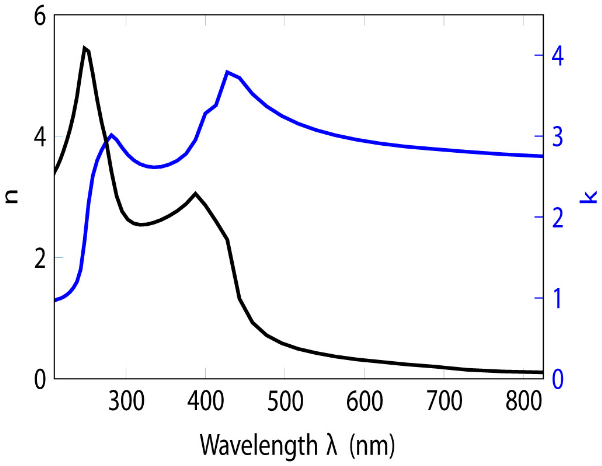

Figure 3.8: Real n and imaginary k parts of the GaAs refractive index, adopted from [63]

Concerning the optical properties, Figure 3.8 shows the real and imaginary part of the index of refraction of GaAs [63].

The work function Φ of GaAs is equal to $4.69eV$. In order to determine the absorption coefficient α of GaAs we use the relation:

$$\alpha = \frac{4\pi k}{\lambda} \tag{3.16}$$

Also in the transmission scheme, the transmittance T as a function of the sample thickness d and the absorption α of a field on intensity I_0 is given by this relation:

$$T(d) = \frac{I(d)}{I_0} = I_0 e^{-\alpha d} \tag{3.17}$$

The Brewster angle of GaAs at $780nm$, which is the NIR center energy, is around 75° which is very close to the incident angle used during our measurement. This fact ensures that there is almost ni reflected NIR field from the sample surface and hence no undesired standing wave will be formed .

In order to give an estimation of the density of the excited carriers to the conduction band $n_{excitation}$ by the NIR laser field, we employ this formula:

$$n_{excitation} = \frac{\alpha I_0 \tau}{E_g} \tag{3.18}$$

where α is is the absorption coefficient which is equal to $1 \times 10^{20} cm$ [64]. I_0 and τ are the intensity and pulse length of the laser field respectively, assuming that we use an intensity of $10^{12} W/cm^{-2}$ and pulse length is around 4 fs. substituting all this in (18) will yield a carrier excitation density of $2.2 \times 10^{20} cm^{-3}$. The whole electron density in GaAs is estimated to be around $2.2 \times 10^{23} cm^{-3}$ according to a density of $5.32 g \backslash cm^3$ and a molar mass of $144.65 g/mol$. Therefore, we can manage to excite up to 0.1% from the valence band to the conduction band in the best scenario. This is not much of an excitation signal given the signal to noise ratio we have. This means that it is extremely necessary to have a resonant process similar to Rabi flopping, in order to be able to excite more carriers to the conduction band.

Chapter 4

GaAs sample Preparation

Sample preparation is an extremely important step in streaking experiments. The photoelectrons detected by the TOF come from the very first few layers since their inelastic mean free path is very small, and this makes the experiments extremely sensitive to the surface structure and quality. In order to characterize the surface structure of our samples, we use Low-energy Electron Diffraction (LEED) and X-ray Photoelectron Spectroscopy (XPS) as monitoring tools.

4.0.1 Low-energy Electron Diffraction (LEED)

LEED is a well established surface science technique that utilizes diffraction principle and enables the examination of the surface quality of single crystal samples. An electron beam, mono-energetic collimated, hits the surface and a diffraction pattern is formed on a fluorescent screen, see Figure 4.1. Diffraction patterns come from the Bragg's law description of electrons as a wave-like particles where the disperse of the angular intensity is affected by the interference of partially back-scattered waves, this leads to the formation of a regular diffraction pattern [65].

In principle, LEED can be used in two ways: qualitatively and quantitatively. In the first way, analysis of the spot positions gives information on the symmetry, size, and rotational alignment of the crystal at the surface. On the other hand, quantitative analysis of the diffraction pattern spots intensities with respect to the incident beam energy yield the so-called I-V curve which provides accurate information on atomic positions. In this thesis, LEED analysis is done only qualitatively which turned out to be good enough to extract conclusive information of our sample surface quality. The electron beam energy is around 400 eV, therefore the mean free path of the electrons is around 1 nm. This implies that LEED will give us information on the structure of the very first layers rather than the bulk.

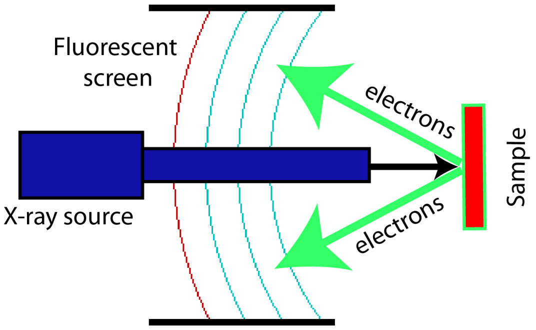

Figure 4.1: Sketch of the LEED installed in the AS3 preparation chamber. The electron beam is diffracted from the crystal surface onto a fluorescent screen where the diffraction pattern is formed.

The single crystal structure of a surface will generate a small and sharp diffraction spots while the amorphous samples will yield smeared patterns.

LEED matches the single crystal surface structure with a diffraction pattern, i.e it records the reciprocal space vectors ($\overrightarrow{v}^*_1$, $\overrightarrow{v}^*_2$) and ($\overrightarrow{w}^*_1$, $\overrightarrow{w}^*_2$) instead of the real space crystal vectors ($\overrightarrow{v}_1$, $\overrightarrow{v}_2$) and ($\overrightarrow{w}_1$, $\overrightarrow{w}_2$) respectively, in the case of a (100) crystal shown in Figure 4.2.

According to [65], the four vectors are related as follows:

$$\overrightarrow{v}_1.\overrightarrow{v}^*_1 = 2\pi \tag{4.1}$$

$$\overrightarrow{w}_1.\overrightarrow{w}^*_1 = 2\pi \tag{4.2}$$

and

$$\overrightarrow{w}_2.\overrightarrow{v}^*_1 = 0 \tag{4.3}$$

$$\overrightarrow{v}_2.\overrightarrow{w}^*_1 = 0 \tag{4.4}$$

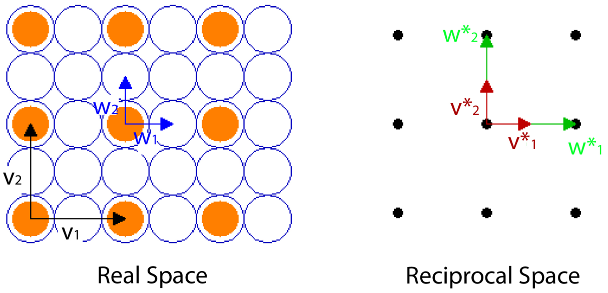

Figure 4.2: Sketch of the real (left) and reciprocal (right) space of a crystal

These equations enable to reconstruct the real space lattice defined by ($\overrightarrow{v}_1$, $\overrightarrow{v}_2$) and ($\overrightarrow{w}_1$, $\overrightarrow{w}_2$) starting from the reciprocal lattice vectors ($\overrightarrow{v}^*_1$, $\overrightarrow{v}^*_2$) and ($\overrightarrow{w}^*_1$, $\overrightarrow{w}^*_2$) measured by LEED.

4.0.2 X-ray Photoelectron Spectroscopy (XPS)

While LEED examines the crystal structure, XPS examines the elemental composition of the crystal. This enables us to assure the absence of impurities in the sample surface. Given the mean free path of the photoelectrons and the small detection angle of them, XPS can probes only the very first layers of a sample which make it a good surface science technique for the AS3 beamline to host. To emit X-rays, we use a radiation source provided by two anodes: Magnesium (Mg $K_\alpha - line, \hbar w = 1253.6eV, \Delta(\hbar\omega) = 0.75eV$) and Aluminum (Al $K_\alpha - line, \hbar w = 1486.6eV, \Delta(\hbar\omega) = 0.85eV$)). To get rid of the satellite lines and the Bremsstrahlung which is typically generated in the X-ray source, we use a monochromator as discussed in [66].

In an XPS, a high voltage is used to accelerate electrons towards a sample, after being released from a hot cathode filament. In a typical XPS experiment, the photoelectrons coming out of the sample are analyzed by a hemispherical analyzer (HSA) which consists of two concentric hemispheres of respective radii R_1 and R_2. We apply an adjustable voltage between the two hemisphere to select the photoelectrons having the right energies. The right energy means the specific energy of a chosen band to be studied.

4.0.3 GaAs grown by Gradient-freeze Technique (GF)

A first attempt to prepare an oxidized-free GaAs surface was made at AS3 using samples grown by molecular beam epitaxy (MBE) and also by ordinary vertical-gradient-freeze technique. With such samples, the first task would be to get rid of the oxidized surface on top. These samples have very good bulk quality but at the surface they have an oxidized layer on top in addition to impurities coming from the ambient. Trying to get rid of this undesired oxidized layer, we use the spattering gun in the chamber in which, high energetic noble gases atoms, such as Neon and Argon, are accelerated using a high voltage potential to bombard the sample surface. This helps to blow away the loosely attached impurities at the sample surface. During this process, the surface structure itself is damaged and relative roughness increases which is not desired in the course of streaking experiments because it could cause electric field enhancement. In order to avoid this, we simultaneously anneal the sample to boost the diffusion rate so that GaAs could easily retain its surface structure. The previously mentioned technique could work for large number of samples but unfortunately not in the case of GaAs. The reason is the relatively low melting temperature of GaAs which prevent us from reaching the necessary temperature for the surface structure to recover. One solution to this would be to have the possibility of applying As-back pressure in the preparation chamber so that the As atoms deficiency due to annealing could be recovered. Unfortunately, in our AS3 preparation chamber we lack such possibility therefore we couldn't prepare these samples and we end up only with samples having blurred low energy electron diffraction (LEED) patterns which is a signal of a bad surface structure as shown in Figure 4.3.

4.0.4 As-capped GaAs

An alternative to GaAs samples grown by the gradient-freeze technique is As-capped GaAs samples grown in Prof. Amman group at Walter-Schottky Institute (WSI) in Garching near Munich. This method turned out to be very successful and it yielded an oxidized-free (100) GaAs single crystal surface.

To grow the As-capped GaAs samples, our collaborators use the MBE technique which offers the possibility of growing a thick As cap on top of the

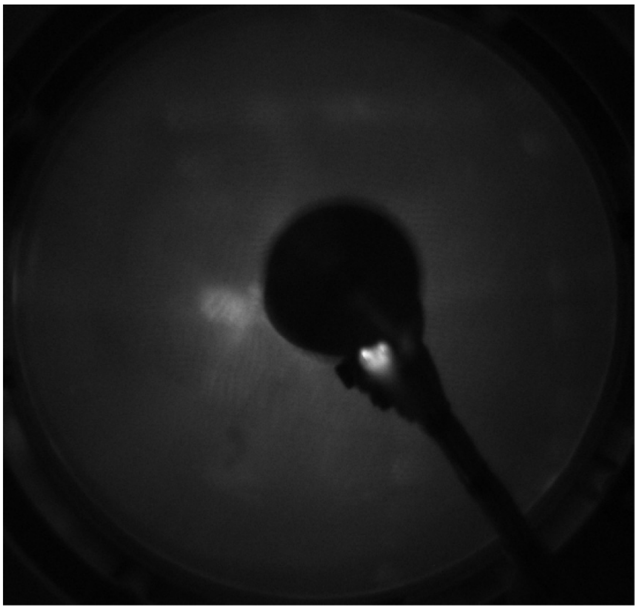

Figure 4.3: Measured LEED pattern of a GaAs (100) sample surface grown by Gradient-freeze Technique (GF). The LEED pattern is totally blurred which is an evidence of the absence of a single crystal at the surface

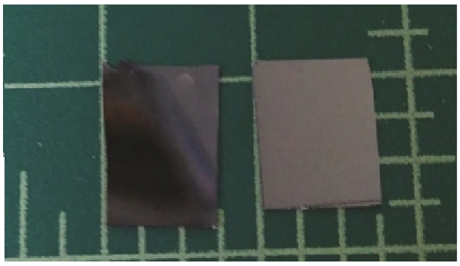

Figure 4.4: A Photo of a grayish GaAs sample which is As-capped (right) along with a mirror-like black de-capped GaAs sample (left)

sample surface while it is in vacuum. This prevents the direct oxidization of the surface whenever the sample is exposed to atmosphere. the oxidized layer will form rather at the top of the As layer and is blown away with As layer during annealing at certain temperature, this will yield an oxidized-free GaAs surface. Figure 4.4 shows two As-capped GaAs samples grown at WSI before (grayish) and after (black) de-capping.

The de-capping is performed in the preparation chamber of AS3 Beamline, it is thoroughly described in [67] and also in [68]. The procedure is to anneal the sample up to $620K$, temperature is monitored by a thermocouple, for about 10 minutes. This is enough to remove the thick As patine from the sample surface. The mass spectrometer in the chamber is used to measure the signal of the desorbed As layer, i.e the decrease of the As signal down to a minimum assures that the patina As cap layer vanished. To check the surface constituents atoms and structure, XPS and LEED were used.

XPS measurement

After having the sample de-capped, we drive it to the experimental chamber to examine the relative signal of Ga and As atoms, in addition to undesired signal coming from impurities. The Aluminum anode is used as an X-ray source in the XPS, it is advantageous compared to the Magnesium anode since it better reveals the possible impurities. In a capped GaAs sample, the only signal detected by the HSA is that coming from Ar, this is clear in Figure 4.5. As annealing starts, we detect less As and more Ga until we end up with a clean GaAs surface where the relative signal of As and Ga matches what is expected according to [67]. The red line in Figure 4.5 is an intermediate stage between the capped and completely de-capped surface.

Figures 4.5 gives information on the relative ratio of As and Ga. In order to fully check the sample concerning the impurities, one has to do a broad energy range scan of XPS, Figure 4.6 gives such a scan. As it is clear,

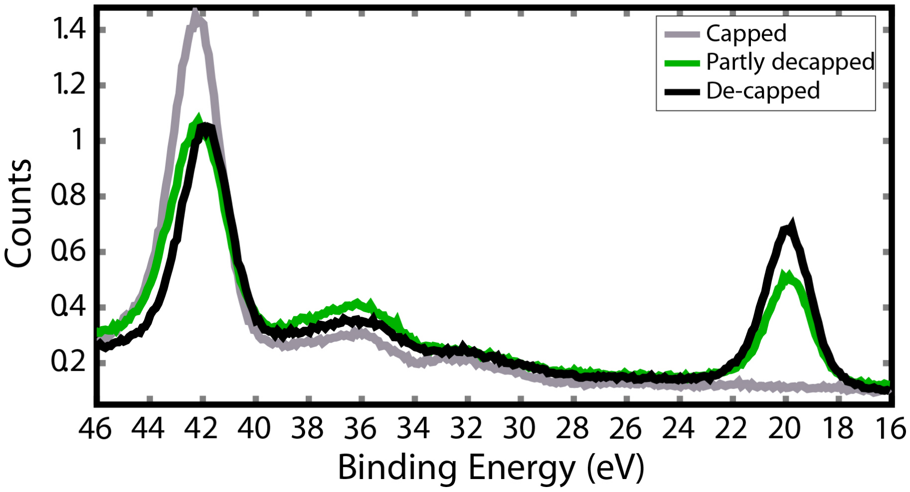

Figure 4.5: An XPS spectrum showing three stages of an As-capped GaAs sample. Grey spectrum is for a sample without annealing, where we see only the signature of As. Green spectrum shows an intermediate spectrum where Ga signature appears though not pronounced enough. Black spectrum shows a sample completely annealed, it have the expected GaAs surface.

there is absolutely no sign of a signature of foreign atom other than As and Ga. This is a conclusive result which assures that we have an impurity-free sample surface.

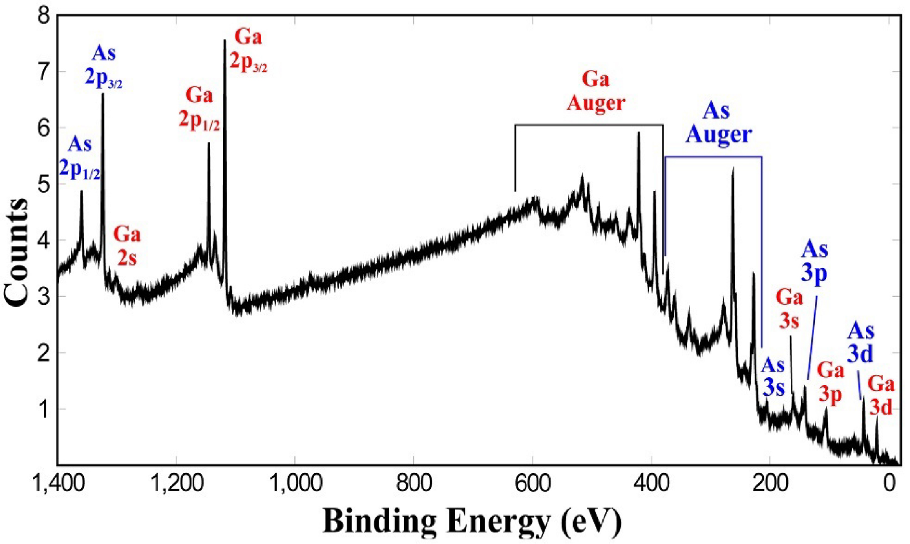

Figure 4.6: A full XPS spectrum of the annealed GaAs sample surface measured at AS3. It shows the expected Ga and As signature and does not reveal any sign of impurities.

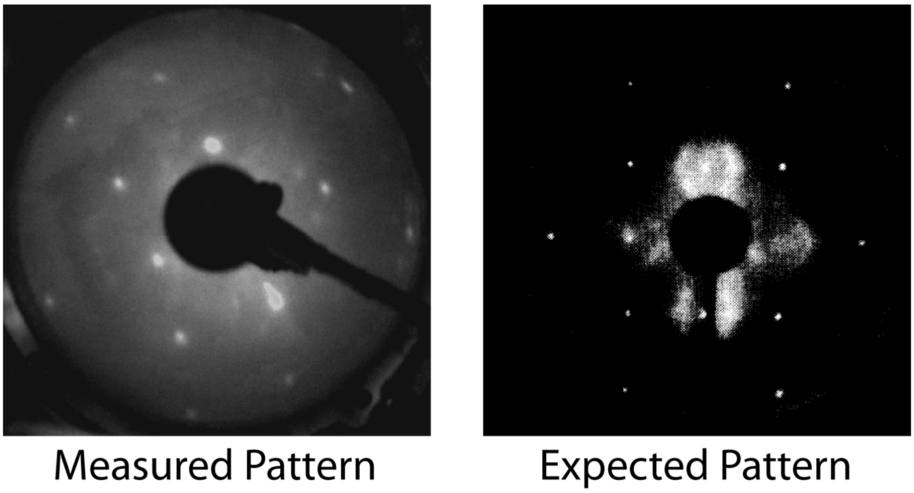

Figure 4.7: Measured LEED pattern (left) along side with a measured LEED pattern taken from [73]. The two pattern are identical, assuring that we attained the desired surface structure at $620K$ annealing temperature.

LEED patterns

De-capping of GaAs is straightforward due to the multiple studies performed before on this topic [67], [69] and also in [70]. It is widely accepted that the best surface structure is determined in the case of As-capped GaAs samples [68] and [71]. De-capping is successful because the decomposition temperature of the As layer is around $620K$ while the decomposition of the used (100) GaAs surface starts at around $990K$. This means that we can get rid of the cap layer before the structure is destroyed. In addition to this, before reaching the decomposition temperature GaAs surface undergoes from several surface reconstructions. One way to check that we have the desired (100) GaAs surface structure is to alter the temperature between $620K$ and $990K$, and trace the LEED pattern to compare with the already known patterns.

Figure 4.7 shows the measured LEED pattern at our laboratory together with that measured in [67] for the sake of comparison.

For temperatures lower than $670K$, the (1×1) reconstruction should take place, this will yield a $(2\times4)-c(2\times8)$ as a sole surface structure [69]. Figure 4.7 clearly shows that this is verified. This structure is stable up to $750K$, this means that up to this temperature the two domains (2×4) and (2×8) coexist. It is important to mention that LEED can not differentiate between the two domains and in both cases it yields a (1×1) pattern [67].

On the other hand, if we anneal the sample beyond to 790 K we end up with a new reconstruction where $(4 \times 2) - c(8 \times 2)$ surface structure is seen as shown in Figure 4.8.

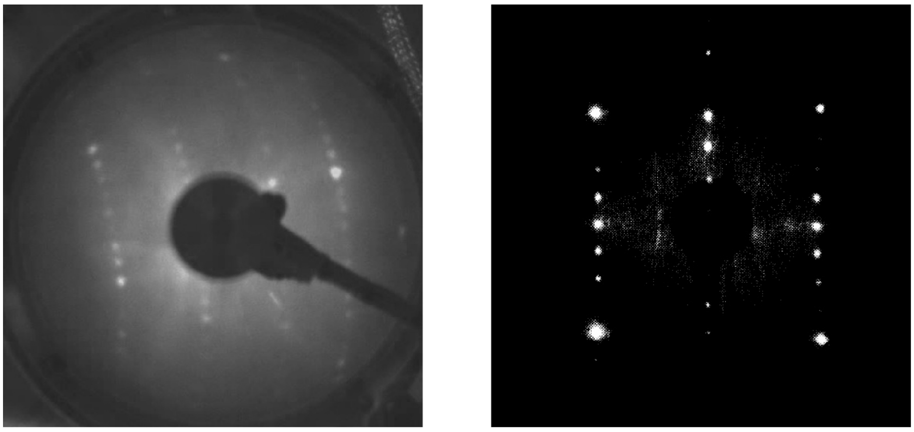

Measured Pattern

Expected Pattern

Figure 4.8: Measured LEED pattern (left) along side with a measured LEED pattern taken from [67]. The two pattern are identical, assuring that we attained the desired surface structure at $790K$ annealing temperature.

In this case, the Ga dimers assemble similar to the As dimers in the previous surface structure as discussed in [69] but with a dimerization direction which is rotated by 90°. Figure 4.9 shows the so-called ball-stick-models of the two domains $c(2 \times 8)$ and $c(8 \times 2)$ in the case of a (1×1) GaAs surface in the real space, it shows the Ga rich surface of second pattern which is a precursor of total surface deconstruction.

Finally, when we annealed the sample beyond $990K$, we saw the so-called star burst LEED pattern as seen in Figure 4.10, which revealed a full decomposition of the surface as predicted in [67]. We consider this to

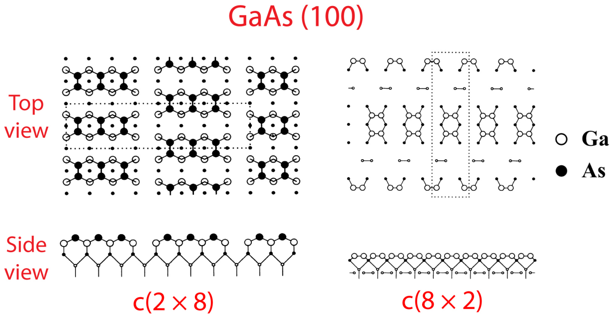

Figure 4.9: A ball-stick-model of two surface reconstructions of (100) GaAs surface, adapted from [69]

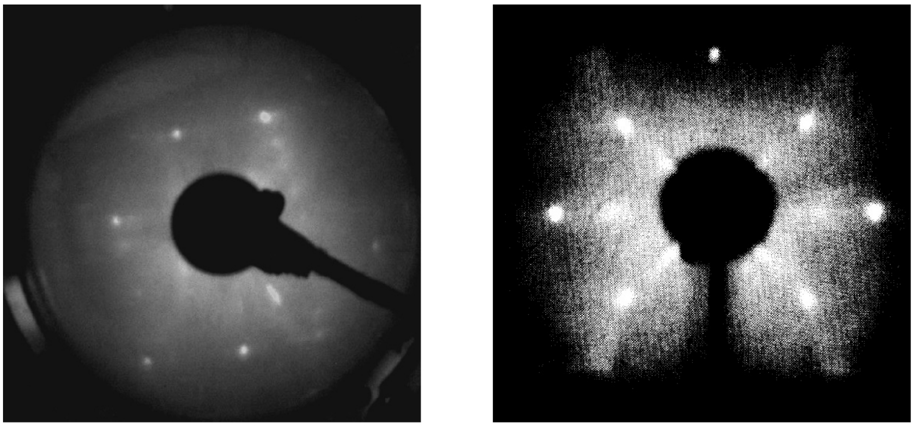

Measured Pattern

Expected Pattern

Figure 4.10: Measured LEED pattern (left) along side with a measured LEED pattern taken from [67]. The two pattern are identical, assuring that we attained a destroyed surface structure at $990K$ annealing temperature.

be a successful treatment of our samples which proves almost a match with previous LEED measurement done on (100) GaAs samples.

Chapter 5

Requirements of PES experiments

Performing PES experiments on a small bandgap material like GaAs is challenging. In order to excite enough photoelectrons from the VB to the CB, one has to illuminate the sample surface with huge NIR intensities. This will increase the energy of the ATI photoelectrons excited by the nonlinear multiphoton ionization processes. This poses a challenge on the ability to see the photoelectrons of the GaAs VB because it will be washed out by the ATI photoelectrons at high intensities. In order to overcome this problem, we have successfully designed a Chromium\scandium multilayer XUV mirror which reflects at 145 eV [72]. This is beneficial to maximize the energy difference between the energy of the VB photoelectrons (dictated mainly by the center energy of the XUV mirror) and that of the ATI photoelectrons (dictated mainly by the NIR intensity).

5.1 Realization of high energy XUV mirrors

In order to better steer and shape attosecond pulses, different material systems and designs were used in developing multilayer XUV mirrors in the soft x-ray regime. At AS3 beamline, we used ion-beam-deposited chromium\scandium (Cr\Sc) multilayer mirrors to reflect isolated attosecond pulses at $145eV$ center energy out from the HHG spectrum.

5.1.1 Growing parameters of Chromium\scandium multilayer mirrors

Researchers are highly interested in optimizing the growing parameters of the multilayer XUV mirrors in the energy range between $284eV$ and $543eV$ [73], named as the water window. This energy interval con-

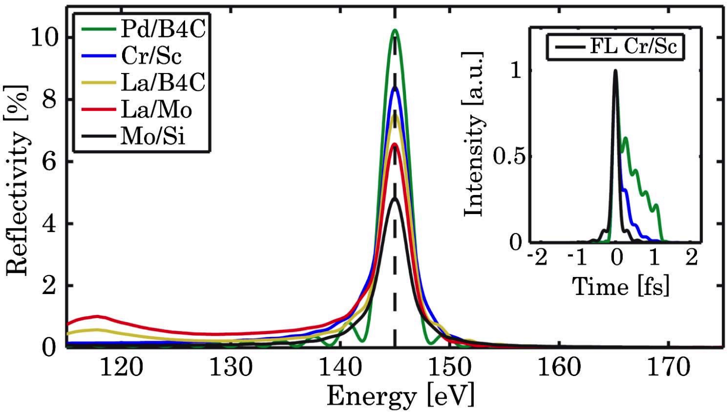

Figure 5.1: Simulation of the reflection of certain multilayer material systems having a FWHM bandwidth of 3 eV centered at 145 eV. The inset shows a comparison of the Cr Sc and Pd B4C systems in the time domain including the transmission through a 200-nm-thick palladium (Pd) filter. The black line shows the Fourier limit (FL) of the Cr\Sc mirror reflection [72]

tains the K-shell absorption of both carbon and oxygen respectively, as discussed in [74] and also [75]. The interest aroses from the ability of the growing parameters of the Cr\Sc multilayer mirror system to be adjusted to yield relatively high reflectivity [72], high resolution in soft x-ray microscopy regime [76] and also soft x-ray astronomy regime [77]. In addition to the ability to be utilized in the time-resolved attosecond soft x-ray spectroscopy [78]. In AS3 beamline, we show that this material system can be used to design a multilayer XUV mirror tailored to realize experiments in the $130 - 160eV$ energy range which has been available in our laboratory without having the access to the appropriate optics before [79]. Designing XUV mirrors reflecting at relatively higher energies helps to increase the energy separation between the XUV photoemission line and the NIR photoelectrons ejected by the nonlinear multiphoton absorption. A simulation was run to compare the yield of some commonly used multilayer material systems reflecting attosecond pulses at 145 eV central energy with a spectral bandwidth (FWHM) of 3 eV at an angle of near normal incidence of 5 degrees, see Figure 5.1.

As we care about both the temporal and spectral bandwidth in the streaking attosecond experiments, we made a trade-off between the two values in the course of these simulations. The simulations were done using a Matlab multilayer Fresnel code, this code utilizes atomic scattering factors from Henke and Gullikson [80]. The outcome of the simulation predicts a weak suppression of the HHG spectrum below $120eV$ in the lanthanum (La)-based multilayer mirrors (La\Mo and La/B_4C).

Table 5.1: Mirror Parameters

System	d[nm]	γ	σ [nm]	N	Capping
Cr\Sc	4.371	0.4	0.5	65	1.4 nm nat. ox.
La\B_4C	4.402	0.5	0.8	50	—
La\Mo	4.423	0.5	0.4	56	3 nm B_4C
Pd\B_4C	4.402	0.6	0.84	44	—
Mo\Si	4.376	0.5	0.5	60	1.5 nm nat. ox.

The suppression is extremely important to have an isolated attosecond pulse. Using a metallic filter does not help in this context, for example if we used a palladium (Pd) filter of $200nm$ thickness we will not end up with a well suppressed pulse due to Pd transmission curve which does not close entirely below $120eV$. At this point we excluded such material systems for reflecting attosecond pulses at $145eV$ center energy. On the other hand, molybdenum-based multilayer systems highly suppress low energy tails of the spectrum as seen in Figure 5.1. Though, in the case of the molybdenum\silicon (Mo\Si) mirrors we encounter a relatively low reflectivity which is not obviously an advantage. The reflectivity of other molybdenum-based multilayer such as: molybdenum\boron carbide (Mo\B4C), molybdenum\yttrium (Mo\Y), molybdenum/beryllium (Mo\Be), or molybdenum\strontium (Mo\Sr)) systems is good enough as discussed in [81]. But the material systems Mo\Y, Mo\Be, Mo\Sr suffer from remarkable spectral modulations near the main reflecting Bragg peak and this introduces group delay dispersion (GDD) which causes temporal broadening of the pulse. In addition to this, the Mo\Sr shows long-term degradation and beryllium is strongly toxic, thus we exclude them as good candidates. The small inset of Figure 5.1 shows the comparison in reflection in the time domain between Cr\Sc and Pd/B_4C [82]. Looking at this inset, Cr\Sc shows a reflection which is close to the Fourier limit with an almost Gaussian pulse shape, while in the case of the Pd/B_4C system we observe temporal broadening basically due to GDD and the multilayer reflectivity fringes which causes temporal modulations. For all the above mentioned reasons, the Cr\Sc material system was chosen since it combines all the mentioned advantages [83]. Table 1 depicts the growing parameters (period thickness d, ratio γ, interface roughness σ and period number N) of the various multilayer material systems used in the simulations of Figure 5.1.

Having chose Cr\Sc material system as the candidate for the multilayer

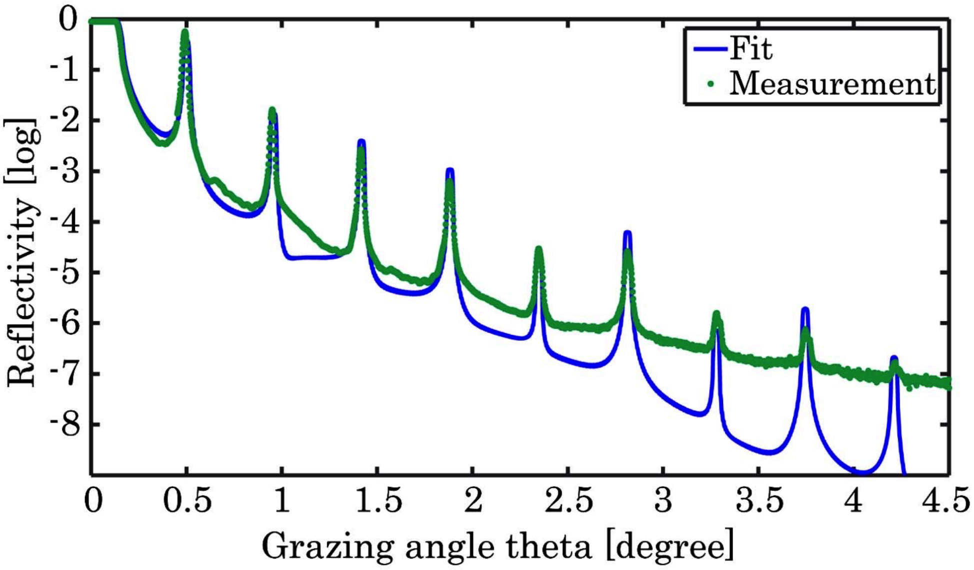

Figure 5.2: Hard x-ray reflectometry measurement (green dots) and the fit (solid blue) for the Cr\Sc mirror. [72]

mirror and optimized the growing parameters according Table 1, we used dual-ion-beam-sputtering technique mentioned in [84] to grow it, and for the sake of higher mirror reflectivity we applied tailored interface polishing according to [37].

5.1.2 Reflectivity measurements

In order to further characterize Cr\Sc multilayer XUV mirror we used both hard x-ray reflectometry and also reflectivity measurements techniques.

hard x-ray reflectometry

A molybdenum k_α-emission line which has a wavelength $\lambda \cong 0.071nm$ was used as a source in the hard x-ray reflectometry (XRR) measurements. The Cr\Sc was grown on a (100) silicon wafer forming a flat witness sample. Figure 5.2 shows both the measured and simulated XRR data of the multilayer XUV mirror.

The fitting shows a relatively small interface roughness, knowing that even the 9th Bragg order is fairly resolved. Furthermore, there exists only a 0.2% discrepancy between the designed period thickness. The Cr\Sc multilayer material system is still showing a periodicity as indicated by

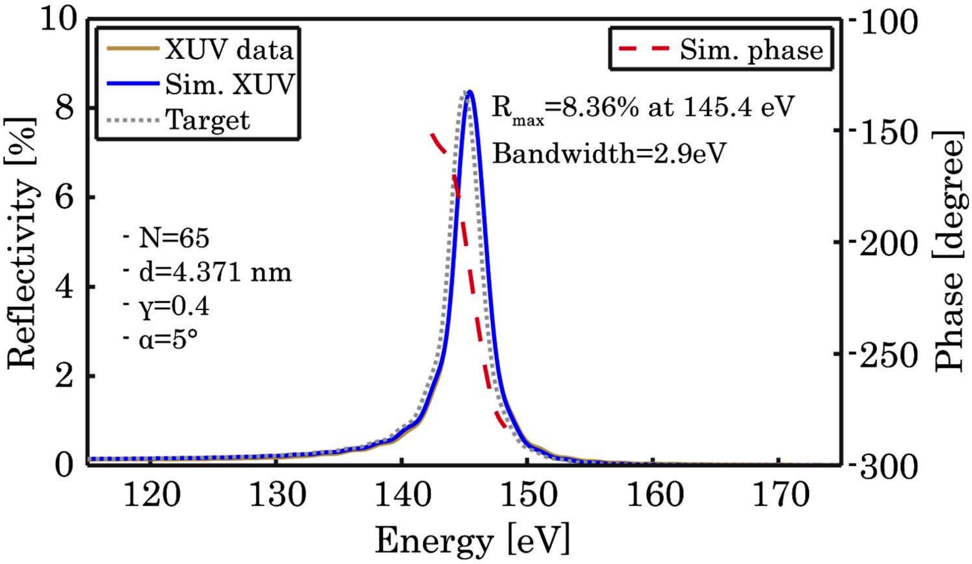

Figure 5.3: XUV\soft x-ray reflectometry measurement (solid brown), the corresponding fit (solid blue), and the target design (dotted gray) together with the simulated phase (dashed red) [72]

very sharp Bragg peaks. This pronounced periodicity is a good sign for a flat spectral phase upon reflection which does not add GDD.

XUV\soft x-ray reflectometry

The reflectivity of the Cr\Sc multilayer material system was further tested at near normal incidence via XUV\soft x-ray reflectometry in the Physikalisch-Technische Bundesanstalt (PTB) beamline at BESSY II in Berlin. Figure 5.3 shows the measured data, together with the simulated data and the target curve.

It is clear that we have an almost perfect match between the measured and simulated data where we have only around 0.27% mismatch of the peak wavelength compared to the target wavelength. The mirror shows a 8.36% reflectivity at $145.4eV$ and with a bandwidth (FWHM) of around $3eV$.

5.1.3 Streaking measurement on Neon using the Cr/Sc XUV mirror

We performed attosecond photoelectron streaking experiment in order to characterize the temporal response of the Cr\Sc XUV multilayer mirror. The XUV pump/NIR probe technique [85] was used to perform

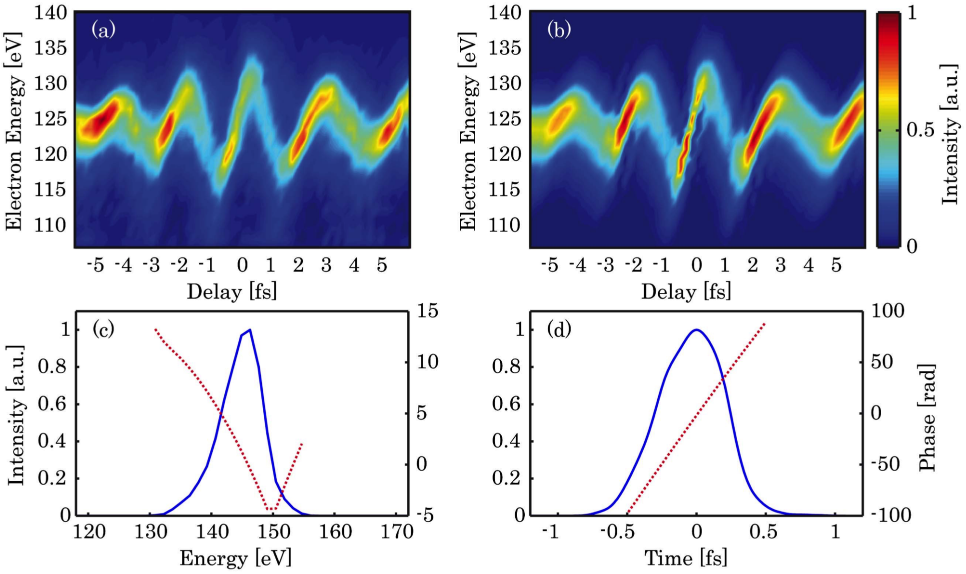

Figure 5.4: Cr/Sc multilayer mirror for attosecond pulses. (a)–(d) Results of an attosecond streaking experiment for pulse characterization in neon. (a) Shows the measured electron streaking trace and (b) the retrieved trace performed by FROG\CRAB analysis. (c) The retrieved soft x-ray pulse (solid blue) and the phase (dotted red) in the spectral domain. (d) Soft x-ray pulse and phase in the temporal domain. [72]

streaking of the Ne photoelectrons in which the XUV pulse ionizes electrons from the 2p shell and then they are momentum-streaked by the NIR pulse. Figure 5.4a and 5.4b show the measured and retrieved streaking spectrogram respectively, we used the FROG\CRAB analysis for the retrieval [86].

The same analysis was used to reconstruct both intensity and phase of the XUV attosecond pulse in the spectral and temporal domain respectively in Figure 5.4c and 5.4d.

The central energy of the XUV photoelectrons shows $145.6eV$, after adding the Ne-2p binding energy which is $21.6eV$. This is a good agreement with the design of the multilayer Cr\Sc XUV mirror. According to the retrieval results, the attosecond pulse duration is estimated to be around $580as$ and this is a good agreement with the Fourier-limited pulse of the $2.9eV$ bandwidth i.e. $629as$. Performing attosecond photoelectron streaking experiments at $145eV$ is itself an achievement, as it is $27eV$ higher than recent energy limit achieved in tabletop attosecond pump studies [87], and it opens the way towards accessing the dynamics of the core levels having higher ionization energies. This is a step towards achieving isolated attosecond at even higher energies up to the water window energy range, this will be extremely beneficial to perform attosecond experiments on biomolecules later.

5.2 Realizing of small-bandgap XUV Mirror

Experiments of attosecond photoelectron streaking spectroscopy offer very high temporal resolution. Streaking experiments done on gases have good spectral resolution since the bands are well separated [88]. This is also the case when streaking experiments are done on metals where core levels are spectrally confined [89]. On the other hand, doing attosecond photoelectron streaking spectroscopy on semiconductors demands a high spectral resolution in addition to the temporal one [90], knowing that both type of resolutions are related via the uncertainty principle. This means that there is a trade-off situation where one should tailor both resolutions to optimize the outcome of a measurement.

To overcome this problem and attain maximum spectral resolution and still have the temporal resolution necessary to perform streaking experiments, we successfully designed and used a Mo\B4C multilayer XUV mirror which has a 112 eV center energy and 1.8 eV bandwidth [91]. The ability to have this relatively small bandwidth was very advantageous since it allows us to spectrally disentangle the photoelectrons of the VB (where a possible excitation could be detected) and that of the Ga 3d photoelectrons. The validity of the mirror is tested by performing attosecond streaking experiments on GaAs samples in the AS3 beamline.

5.2.1 Narrowband XUV multilayer mirror

Attosecond streaking measurements of semiconductors electron band structure requires high spectral resolution [92]. On the other hand, streaking is only possible, according to [92], if the XUV pulse length is smaller than half of that of the NIR pulse. Otherwise, streaking vanishes for longer attosecond pulses, and the process changes into a spectrum of sideband pronounced "Reconstruction of Attosecond harmonic Beating By Interference of Two-photon Transitions" (*RABBITT*).

A first attempt to perform attosecond photoelectron streaking spectroscopy measurements was done on (100) GaAs surface using an XUV multilayer mirror reflecting at 112 eV with a bandwidth of 5 eV. This mirror was grown by Alex Guggenmos at Max-Planck-Institute for quantum optics (MPQ). Obviously, the relatively large bandwidth of the XUV mirror raises the concerns of energy resolution. The convolution of the pulse

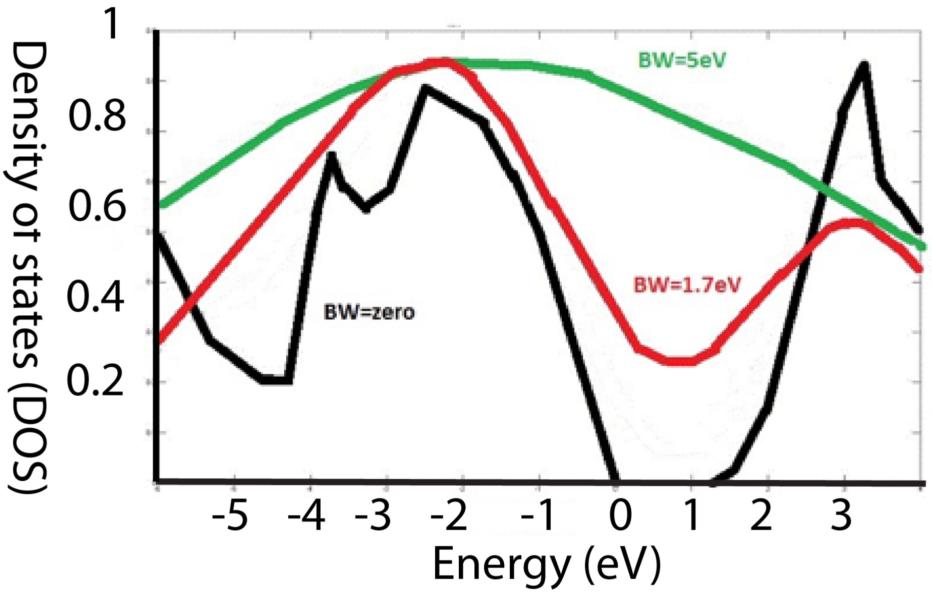

Figure 5.5: convolution of the density of states (DOS) with 0, 1.7, and 5 eV bandwidth

bandwidth with that of the TOF makes the issue even more critical since it washes out the possible excitation signal that one might search for in the VB and CB of GaAs. This was a principle motivation to try to narrow down the bandwidth of the XUV mirror as far as possible.

Growing an XUV multilayer mirror is far from being a trivial task. It is usually a trade-off between several parameters such as the desired spectral and temporal bandwidth via the uncertainty principle. To grow the XUV mirror, we chose the Mo\B4C material system since it allows precise determination of the spectral resolution limit for attosecond streaking experiments by a specific tuning of the multilayer growing parameters [88]. The spectral bandwidth of a multilayer mirror at a certain central energy can be influenced by the number of periods and the layer thickness ratio [93].

Before going into these details, we performed a simulation of the electron density of states (DOS) near the bandgap of GaAs convoluted with three different bandwidths: zero, 1.7 eV, and 5 eV. See figure 5.5.

It is obvious that the case where we have a zero-bandwidth is a perfect situation, spectrally speaking, because this clearly separates the VB and the CB. Though, this is not a real example because the engineering of such a mirror is basically impossible in up-to-date technology. The case of the density of states being convoluted with a 5 eV bandwidth is the same situation which we had before. It is clear that it is hard to differentiate between the CB and the VB which makes it even harder to see a possible excitation signal. On the other, looking at Figure 5.5 we see that using an XUV mirror of $1.7eV$ bandwidth seems to be a good choice since when we convolute the GaAs density of states with its bandwidth, we can see a discrepancy between the VB and the CB and this is certainly an advantage to detect an excitation signal from the VB to the CB.

Optimized growing parameters As a trade-off between reflectivity, narrow spectral bandwidth, flat phase in addition to the stability of the materials, the molybdenum\boron carbide system (Mo\B$_4$C) was chosen. In principle, such a material system allows a better definition of the limit of the spectral resolution in streaking experiments since it gives the chance to better control the parameters of the multilayer designed system. It is well known that the number of periods N, the layer thickness ratio γ, and the period thickness d contribute to the center energy at which the multilayer mirror reflects [91]. As an example, a molybdenum\silicon (Mo\Si) multilayer mirror realized in [94] has a spectral bandwidth around $500eV$ and it reflects at $97eV$ photon energy. For this material system, 300 periods, also called bilayers, were used with $\gamma = 0.04$.

It is noted that the Mo\B$_4$C system examines high stress in the case of a strong layer thickness ratio γ (bottom layer thickness versus period thickness) and high period number N [91], see Figure 5.6 (a). This stress which causes a self-destroying mechanism is independent of the sample material or even on capping or adhesion layers. As discussed before, we set ourselves to a $1.8eV$ bandwidth in order to achieve the maximum limit of the XUV pulse duration necessary to perform a successful streaking experiment. In order to avoid the high stress within the coating, we used an overall stack height of $400nm$. This translates into a period number N=70 and a gamma ration γ=0.35. We end up with a self-destructing-free XUV mirror coating as seen in Figure 2b.

Figure 5.6c shows the dependence of the simulated reflectivity on the gamma ratio γ=dMo\d and also the period number N for the Mo\B$_4$C material system centered at 112 eV. It shows clearly the interconnected parameters of γ, N, and reflectivity.

It is known that to allow larger period numbers and a lower gamma ratio, one has to optimize the deposition process by reducing the kinetic energies of the target atoms [95]. This will cause a lower spectral bandwidth and a more accurate experimental determination of the spectral resolution limit.

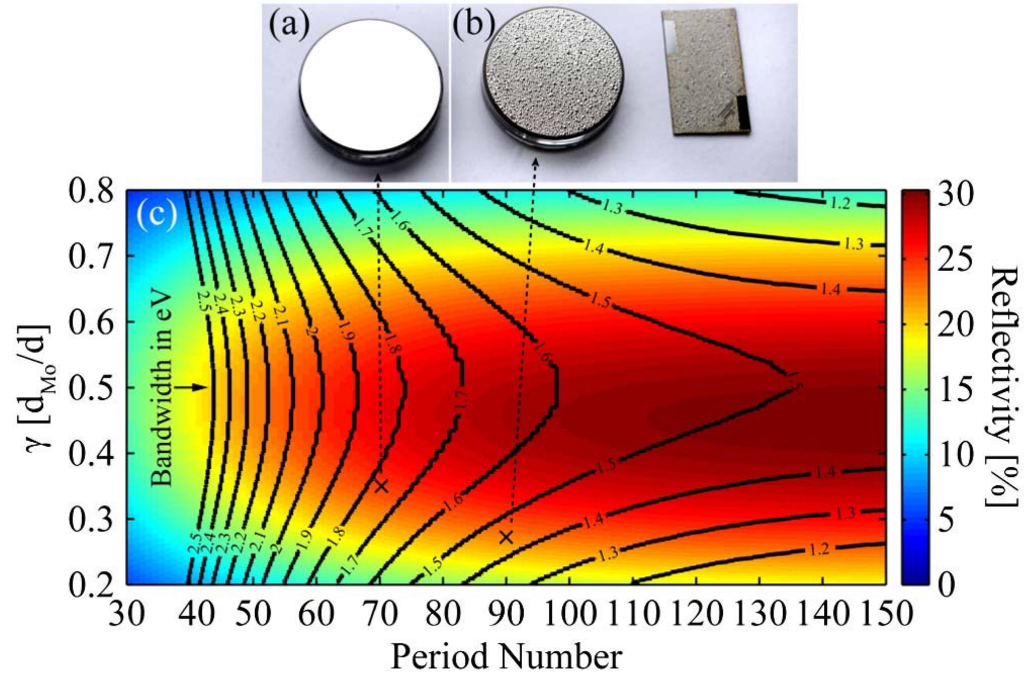

Figure 5.6: Mirror without (a) and with (b) delaminating multilayer coating. (c) simulated reflectivity dependence on the gamma ratio γ (The layer thickness ratio) and the number of periods N for the Mo\B4C material system centered at 112 eV. The corresponding spectral bandwidths in the eV unit are additionally depicted as black contour lines. [91]

Synchrotron Reflectivity measurement The design of the material system in the Mo\B$_4$C multilayer XUV mirror was intended to reflect at $112eV$, with a $1.8eV$ bandwidth under an angle of incidence equal to 5 degrees. This means that the mirror will reflect an isolated attosecond pulse at the cut-off of the HHG spectrum near the Gaussian shape pulse Fourier limit of around $1000as$. In order to test the reflectivity of the Mo\B$_4$C mirror, we carried out spectral characterization of it at the Physikalisch-Technische Bundesanstalt (PTB) beamline at BESSY II in Berlin [96], see Figure 5.7.

The narrow bandwidth ($1.8eV$), which is the main target of the mirror, was successfully tested and the spectral measurement shows an excellent match with the predicted bandwidth. The measurement shows a $600meV$ shift from the target center energy. The measured reflectivity at the center energy is 23.9%, it is known that other material systems, such as molybdenum\beryllium [97], could yield higher reflectivity at the expense of using toxic materials. Moreover, other material systems, such as molybdenum\strontium [98], are not sufficiently stable and they suffer from long term degradation. On the other hand, molybdenum\yttrium [99] causes strong spectral modulations around the Bragg peak via Kiessig

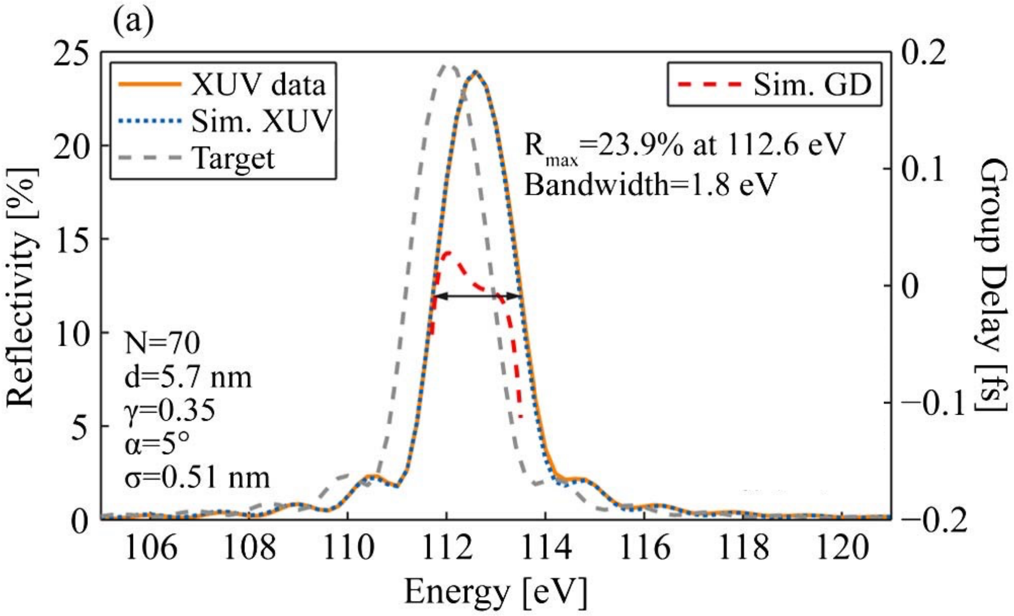

Figure 5.7: Measured spectral reflectivity profile (solid orange) of the realized Mo\B4C multilayer mirror, its fit (dotted blue), the target profile centered at 112 eV (dashed gray), and the corresponding simulated group delay dispersion GD (dashed red) within the bandwidth of 1.8 eV ΔE . The multilayer design parameters are listed bottom left [91]

fringes and this introduces group delay dispersion (GDD) which introduces temporal broadening into the pulse [100]. In the small inset of Figure 5.7, the complete spectral range of the normalized measured reflectivity profile is shown. It indicates a high suppression of the higher and lower frequency components which contribute to a better performance of the mirror to reflect an isolated attosecond pulse.

The first goal of our measurement would include the attempt to see an excitation in the conduction band of GaAs. To do so, one needs to see some discrepancy between photoemission spectra collected before and after the NIR pulse being impinged on the sample surface. It is clear that only after the NIR is impinged on the surface, some photoelectrons will be excited, with a non-zero probability, to the conduction band. Then the XUV can excite some of the excited photoelectrons in the conduction band.

Need for a narrow bandgap XUV mirror The first step of such measurement would include the attempt to see an excitation in the conduction band of GaAs. To do so, one needs to see some discrepancy between photoemission spectra collected before and after the NIR pulse being impinged on the sample surface. It is clear that only after the NIR is impinged on the surface, some photoelectrons will be excited, with a non-zero probability, to the conduction band. Then the XUV can excite some of the excited

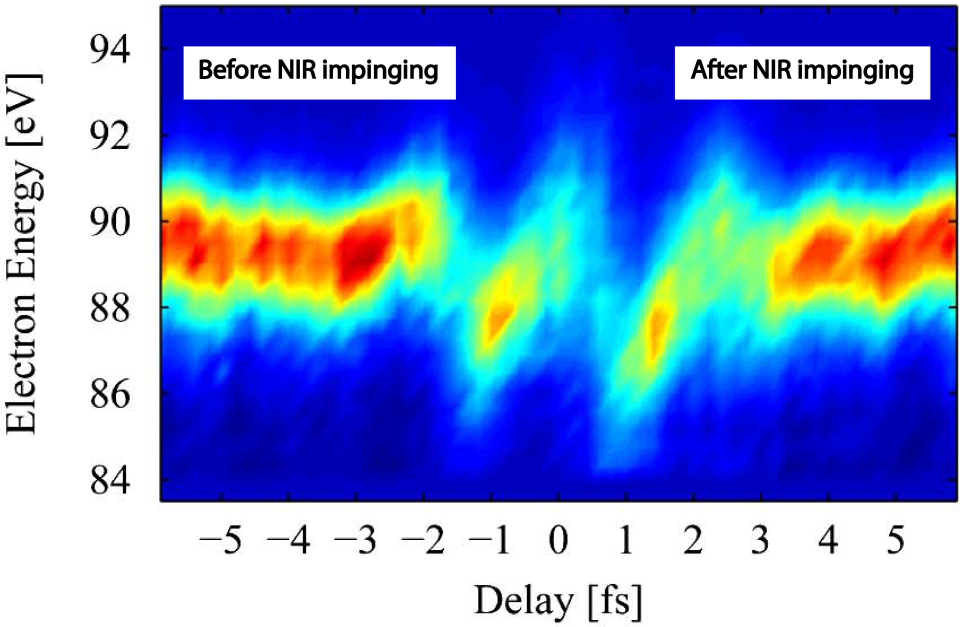

Figure 5.8: A trace showing the spectra before and after the impinging of the Laser field on the sample. The signal would suggest a discrepancy between the spectra before and after the impinging of the NIR pulse

photoelectrons in the conduction band. It is clear that it will not be an easy task to find an excitation is such a situation regarding the spectral resolution. The photoelectrons from the Ga peak has 18.6 eV as binding energy, and they are spectrally convoluted with the 5 eV bandwidth of the XUV mirror. In addition to this, the photoelectrons of the Ga peak has high counts in compared to those of the VB. All of the mentioned points, adds to the difficulty of the situation.

As mentioned before, at this point we adapt a very simple approach to search for an excitation signal. This approach involves comparing the spectra after and before the impinging of the NIR pulse on the sample. Figure 5.8 shows an example of such a trace taken by an XUV mirror of $5eV$ bandwidth.

One way to compare the spectra is to compare simply the count difference, or even to subtract the first moment of the spectra before and after. Data shows no consistent difference could be extracted from the traces which span large NIR intensities beyond $10^{12}Wcm^{-2}$. This means that there is no evidence of an excitation signal from the VB into the CB. One of the obvious reasons is the relatively large bandwidth of the XUV mirror which makes it hard to have a separable photoelectron signal between the

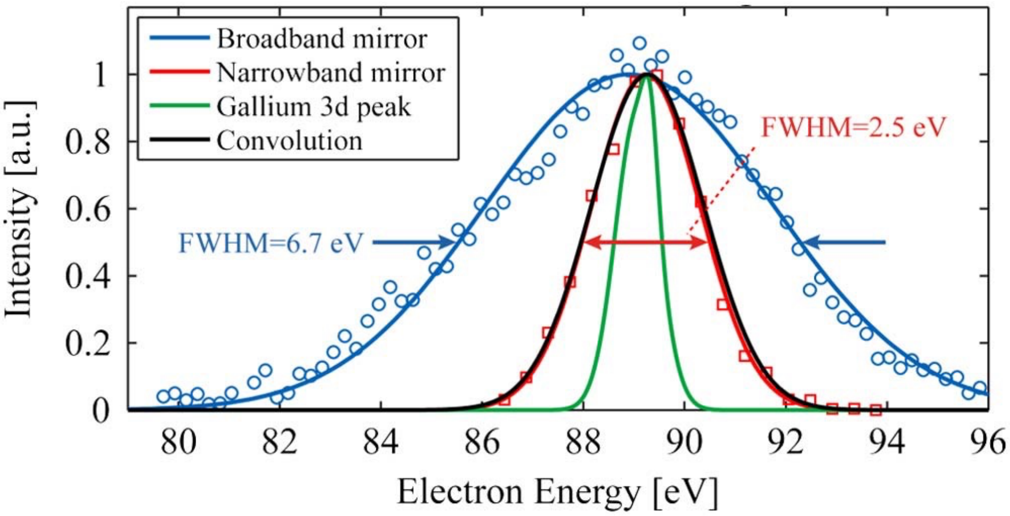

Figure 5.9: Measured spectral reflectivity profile (solid orange) of the realized Mo\B4C multilayer mirror, its fit (dotted blue), the target profile centered at 112 eV (dashed gray), and the corresponding simulated GD (dashed red) within the bandwidth of ΔE=1.8 eV. The multilayer design parameters are listed bottom left [91]

VB and the Ga peak. One way to tackle this problem is to use an XUV mirror with much narrower bandwidth.

5.2.2 Streaking measurement on GaAs using the narrow bandgap XUV mirror

After checking the designed narrow bandwidth of the Mo\B$_4$C multilayer XUV mirror in Bessy II in Berlin, we performed attosecond photoelectron streaking experiments on the (100) GaAs sample surface.

Comparison of the spectral resolution in Ga 3d core level

At AS3 beamline, we remeasured the spectral bandwidth of the reflected XUV pulse convoluted with the TOF spectral resolution at $112eV$. Figure 5.9 shows unstreaked photoelectron spectrum of Ga 3d peak with the wide bandwidth XUV mirror (FWHM= $5eV$) together with unstreaked photoelectron spectrum of Ga 3d peak collected with the narrow bandwidth XUV mirror (FWHM= $1.8eV$).

Figure 5.9 reveals a striking progress in terms of the spectral resolution and also in terms of signal-to-noise ratio. Off course, our main goal will be to look at the VB of GaAs, but looking at the Gallium peak also gives a hint about the better resolution reached by the new Mo\B$_4$C multilayer XUV mirror. Unlike the synchrotron data, at AS3 the reflected attosecond pulse will not bear the almost-bare bandwidth of the mirror, rather the

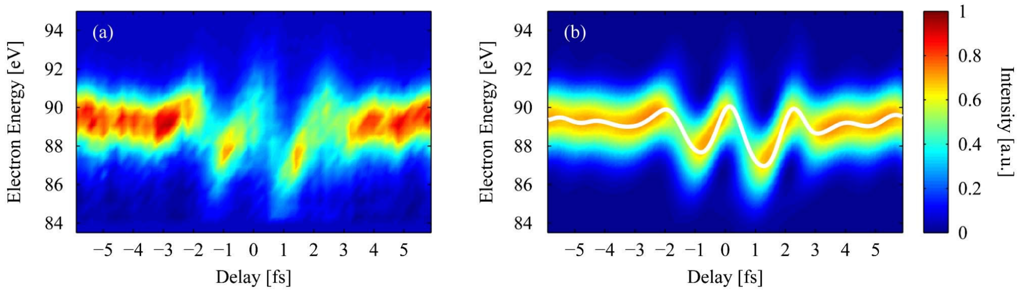

Figure 5.10: (a) Measured and (b) retrieved electron streaking on GaAs. The white line in (b) depicts the retrieved vector potential A(t) of the NIR pulse [91]

bandwidth of the photoelectron spectrum will be dressed by the TOF, which is estimated to be around 1 eV at this center energy, and also the double peak structure of Ga 3d [101].

Streaking of (100) GaAs sample surface

The ultimate goal of such a measurement is to have an access into the dynamics of the excitation from the VB into the CB in GaAs and streaking experiments enables such information. On the other hand, one could simply use the spectrogram to check the existence of the excitation rather than delve into the dynamics of this excitation. Figure 5.10(a) shows a measured photoelectron streaking trace of the GaAs Ga 3d core level together with its retrieval.

Figure 5.10a shows a well streaking trace of good quality although the spectral bandwidth and the flat phase of the mirror suggest an attosecond pulse duration close to a half of the probing NIR period, which is in theory the limit of a successful streaking experiment. Figure 5.10b shows the a retrieval spectrogram determined by the FROG\CRAB analysis thoroughly discussed in [93] and [102]. Figure 5.10b depicts also the vector potential of the streaking NIR field as an eye guiding. It is worth mentioning that the energy of the measured Ga 3d core level is shifted by the Ga 3d core level binding energy, i.e 18.6eV [101] in addition to the work function of GaAs which is estimated to be around 4.69eV according to [103].

The FROG\CRAB is used also to retrieve the intensity and phase in both the spectral and temporal domains as shown in Figure 5.11a and 5.11b respectively. Figure 5.11a shows a spectral bandwidth (FWHM) of 2.8eV which is 1eV larger than the measured in the synchrotron. This is attributed to many reasons, mainly to the precision of the TOF which is estimated to be around 1% of the center energy, also the double structure

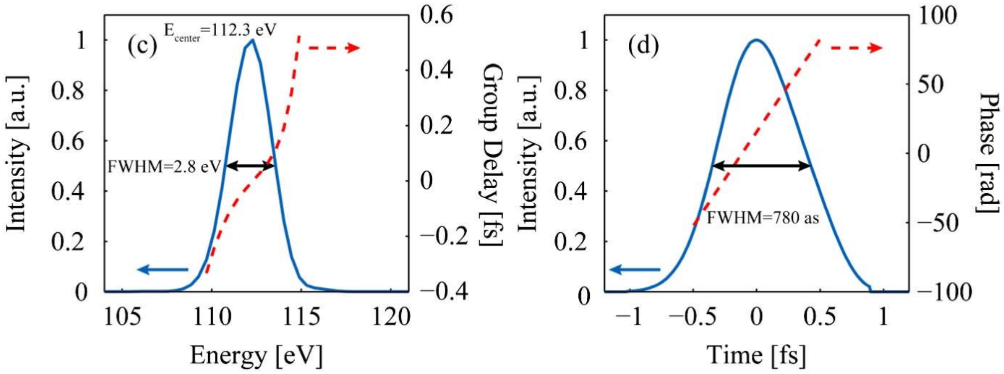

Figure 5.11: Retrieved XUV pulse in the spectral (a) and temporal (b) domains [91]

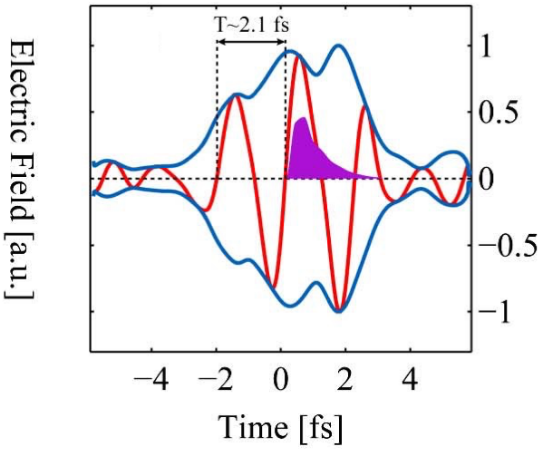

Figure 5.12: Calculated electric field of the NIR (solid red), the envelope (solid blue), and the simulated XUV pulse (purple) [91]

of the Ga 3d peak [101] contributes to the broadening. On the other hand, the spread in the spectral bandwidth leads to a shorter retrieved XUV pulse duration of $780as$ in the time domain ass seen in Figure 5.11b.

Figure 5.12 shows the retrieval of the streaking NIR electric field, together withe envelope. It shows that the NIR field duration around $2.1fs$ which indicates again the theoretical limit of streaking which states an upper limit for the duration of the XUV pulse to be half that of the NIR [92]. Clearly, the duration of the current retrieved XUV pulse is shorter than this upper limit.

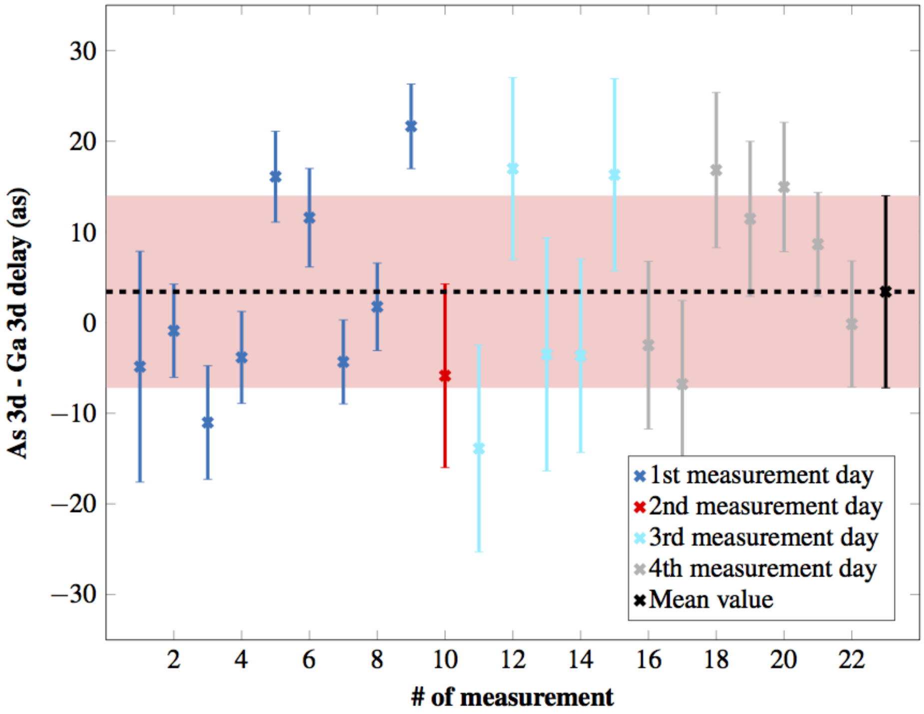

Figure 5.13: Photoemission delay recorded on GaAs(100). Bars represent the standard deviation. The dashed lines represents the mean value and the reddish area the standard deviation of all 22 measurements [104]

5.3 Photoemission delay between Ga 3d and As 3d core levels

One of the most interesting benefits in a photoemission streaking spectroscopy experiment is the ability to measure the time delay between photoelectrons coming from different core levels. In the streaking traces of GaAs samples, one could investigate the time delay between photoelectrons emerging from the As 3d core level and those coming from the Ga 3d core level. As discussed in the sample preparation section, GaAs has several surface reconstructions and the study of the delay is related to the way the GaAs surface is constructed.

To extract the delay between the two photoemission lines, we used the algorithm described in [59]. We define the negative delay to be the Ga 3d electrons lagging behind the As 3d electrons. Figure 5.13 shows the delay extracted from 22 streaking traces collected from (100) GaAs which have the $(2 \times 4) - c(2 \times 8)$ surface construction. The yield of the measurement shows a delay of $3 \pm 11as$.

A direct byproduct of this measurement would be that the measured sample is not As-capped GaAs since if it is the case we would detect a negative delay obviously as the As layer would be on top.
The NIR laser pulse is almost totally refracted inside the GaAs sample, so the absence of the metallic screening [105] which causes the laser pulse to penetrate into the sample will not cause undesired streaking of the XUV photoelectrons. This ensures to a large extent that the photoelectrons are streaked only by the NIR field in the TOF direction.
The localization properties of electrons of both Ga 3d line and As 3d lines are almost identical, this is because Ga and As atoms have similar structure as seen in the the sample preparation section in the case of the $(2 \times 4) - c(2 \times 8)$ surface construction of (100) GaAs. In other words, the time needed by a photoelectron to be kicked off from the surface, which is called the intrinsic time of photoemission, is identical for both lines of photoemission. Indeed, we have measured a delay of $3 \pm 11 as$ which is a very good match with what was predicated. This zero delay suggests that photoelectrons from both lines are probed by the laser pulse at almost the same instant.
This shows that photoemission streaking experiments could be used to investigate the reconstruction of the surface that takes place under the effect of annealing, where the measured delay between the photoelectrons coming from various core levels could be used to reveal the structure of the surface.

Chapter 6

Space-charge effects in Graphene

The most prominent undesired side effect of using an intense NIR field on photoemission experiments is the so-called vacuum space-charge effects which affect the photoemission spectra [106]. When probing the sample with a relatively intense laser field, the coulomb interactions among the NIR nonlinearly photoemitted electrons and also between them and the photoemitted electrons emitted by the NIR laser field causes distortions to the whole photoemission spectra. This poses a fundamental limitation on the resolution of the ultrafast experiments [107], especially in the course of experiments involving huge NIR intensities.

6.1 Mean Field Model

The XUV pulse induced vacuum space-charge effects are well understood [108] and one uses several analytical mean-field models [109] in addition to numerical N-body simulations [110] in order to reproduce them theoretically. On the other hand, the space-charge effects resulting from the Coulomb interactions between photoelectrons ejected from an XUV pulse and NIR pulses are not yet well understood [111]. L. P. Oloff et al. used 31 fs NIR pulses and frequency doubled UV at 1.58 eV and 3.16 eV as pump pulses alongside with an 11 fs XUV probe pulses at 22.1 eV to perform time- and angle-resolved photoemission spectroscopy experiments (TrARPES) in a pump-probe scheme [112]. They pumped Bulk highly oriented pyrolytic graphit samples (HOPG) with intensities up to 10 $mJcm^{-2}$ NIR and up to 2.1 $mJcm^{-2}$ UV. In order to reproduce the recorded delay dependence of the induced spectral space-charge shift in the XUV spectra, L. P. Oloff et al. used a mean field model which was essentially developed

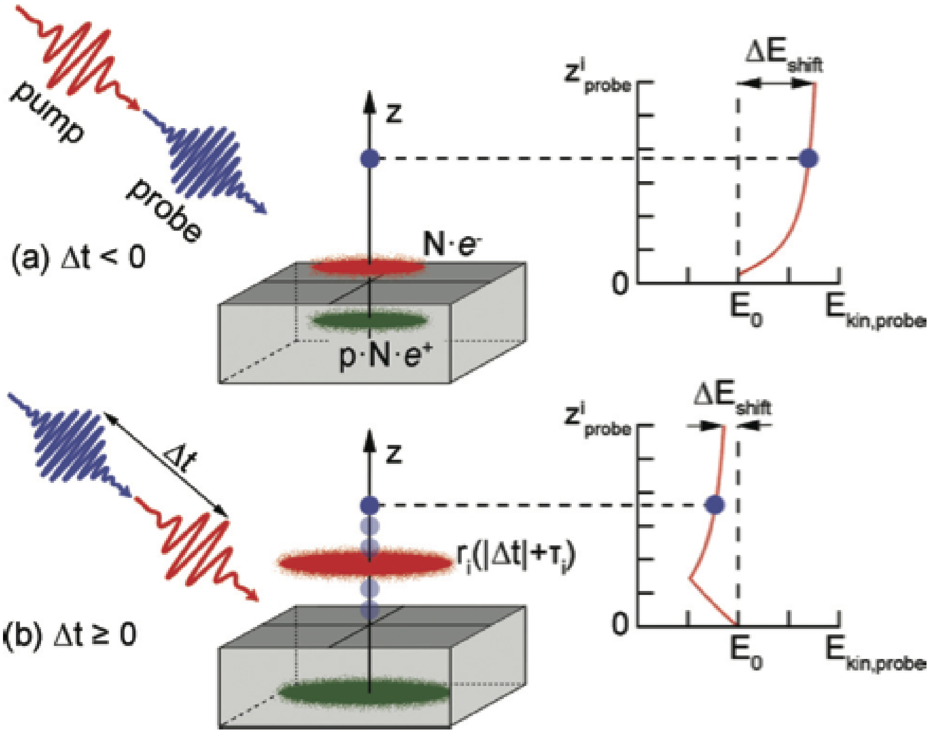

Figure 6.1: Schematic illustration of the model used to reproduce the dynamics of the pump pulse-induced spectral space-charge shift for (a) negative and (b) positive pump-probe delays. The N-electron cloud emitted by the pump pulse as well as its mirror charge cloud is modeled by homogeneous disks of charge with radius r. The probe electron is allowed to move only in the direction of normal emission (z direction). The space and mirror charge induced change of the probe-electron kinetic energy; probe is evaluated in time intervals by calculating the on-axis electric fields Ez as well as the corresponding electrostatic potentials Uz (not shown) of both pump-induced charge clouds at the probe-electron position. The procedure is repeated until the probe electron reaches the detector, where the change in kinetic energy then becomes the detected energy shift [112]

to reproduce the transient electric fields in ultrafast electron diffraction experiments [113]. In this model, the electron cloud excited by the NIR pulse is assumed to be a homogeneous disk moving at an average speed v_{pump} normal to the surface along the z direction. Therefore, the electric field caused by this disk is approximated to have this form:

$$E^z = \frac{Ne}{2\epsilon_0 \pi r^2}(1 - \frac{z}{\sqrt{z^2 + r^2}}) \tag{6.1}$$

where N denotes the number of electrons excited, ϵ_0 the permittivity constant and r the radius of the disk. $p.N$ is introduced in order to account for the mirror charges in the sample. Figure 6.1 shows a schematic diagram of the used model.

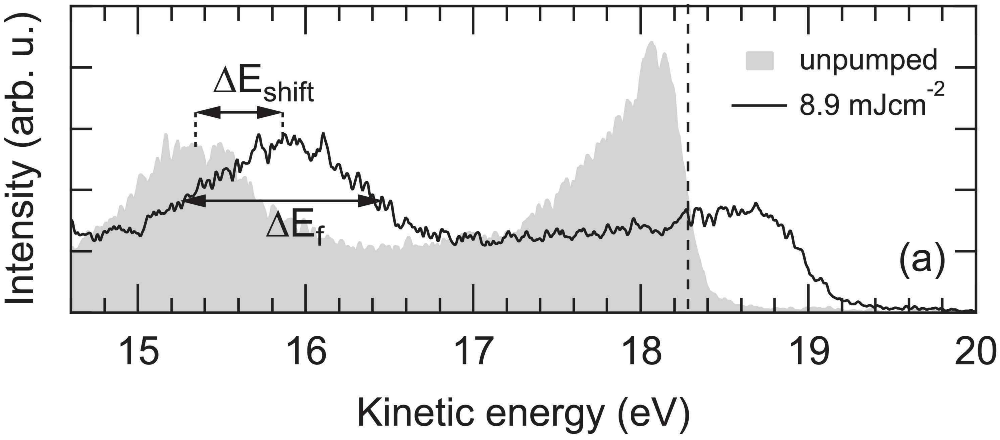

Figure 6.2: Typical momentum-integrated energy distribution curves of the valence band of HOPG. The space-charge shift is defined as the energy shift of the pumped spectrum (Black line) relative to an unpumped spectrum (Shaded area) and the Gaussian broadening as the full width at half maximum (FWHM) [112]

For negative delays, the XUV photoemitted electrons leed and the NIR photoemitted electrons (approximated as a charged disc) drag behind. The opposite thing happens for positive delays, and this is a bit more interesting case since the XUV electrons have to pass through the disc to reach the detector.

6.2 Energy Shift

6.2.1 Relaxation dynamics versus pulse energy

Figure 6.2 shows the energy shift of an XUV spectrum at a given NIR intensity as measured by [112]. The energy shift, represented by ΔE on Figure 6.2, is the shift between the energy of the unpumped spectrum (shaded) and that of the pumped spectrum (black line).

Figure 6.3 shows the energy shift as a function of the pump intensity. The figure shows the shifts in the case of two pumps, UV and NIR.

According to Figure 6.3, the NIR shifts and broadenings have a E_p^3 dependence while the UV shifts and broadenings has a E_p^2 dependence. This can be explained by the nonlinearity of the multiphoton ionization process. The Fowler-Dubridge model, explained in [114], calculates the necessary photocurrent densities which enable photoemission, using ultrashort pulses which have energies less than the work function $W = 4.6eV$ of the sample. The model predicts a E^n dependence where n is the lowest integer which fulfill the equation $n.h\nu$ greater than W. So, we should get n=2 for the UV pump ($3.16eV$) and n=3 for the NIR pump ($1.58eV$).

Regarding our Graphene samples, looking at their work function [115] and the energy of our NIR laser pulse, we should expect that n=3 in the power law of Fowler-Dubridge model. This would mean that the energy shifts should have E_p^3 dependence.
Figure 6.4 shows one of the collected photoemission streaking traces done on our Graphene samples. It shows the shifts at an NIR pulse energy of 322 nJ. One can clearly see the shift to lower energy which takes place due to the NIR impinging on the surface. This energy shift is dependent on the NIR pulse enrgy as we will show next.

Figure 6.5 shows a good match with the results reported in [112] and depicted previously in Figure 6.3.

6.2.2 Relaxation dynamics versus pump-probe delay

Figure 6.6 shows the time dependance the extracted space-charge relaxation which is happening on a $100ps$ time scale for several pump intensities which ranges from $0.9mJcm^{-2}$ and $2.1mJcm^{-2}$ [112].

Figure 6.7a and 6.7b shows the relative relaxation time $\frac{\Delta E}{E_{max}}$ in the positive and negative delays respectively as measured in [112]

For negative delays, the XUV photoelectrons are ejected before the emission of the pump electrons. We see in Figure 6.6 that the temporal relaxation is independent from the pump intensity. On the other hand, for positive delays, increasing the pump intensity causes an increase in the energy shift and produces a faster relaxation time as well. In addition to this, the data shows spectral shifts to even lower kinetic energies compared to unpumped spectrum. This can be explained by the mirror changes induced by the pump photoelectrons. For positive delays, the XUV photoelectrons

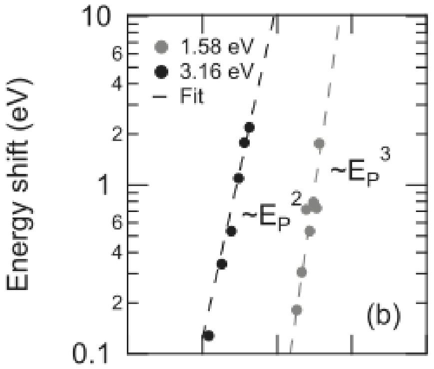

Figure 6.3: Spectral shift as a function of the pump-pulse energy, Ep, at a fixed pump-probe delay in a double logarithmic plot. The dashed lines are fits to the experimental results, and the dotted line represents a model calculation. Power law dependencies are indicated [112]

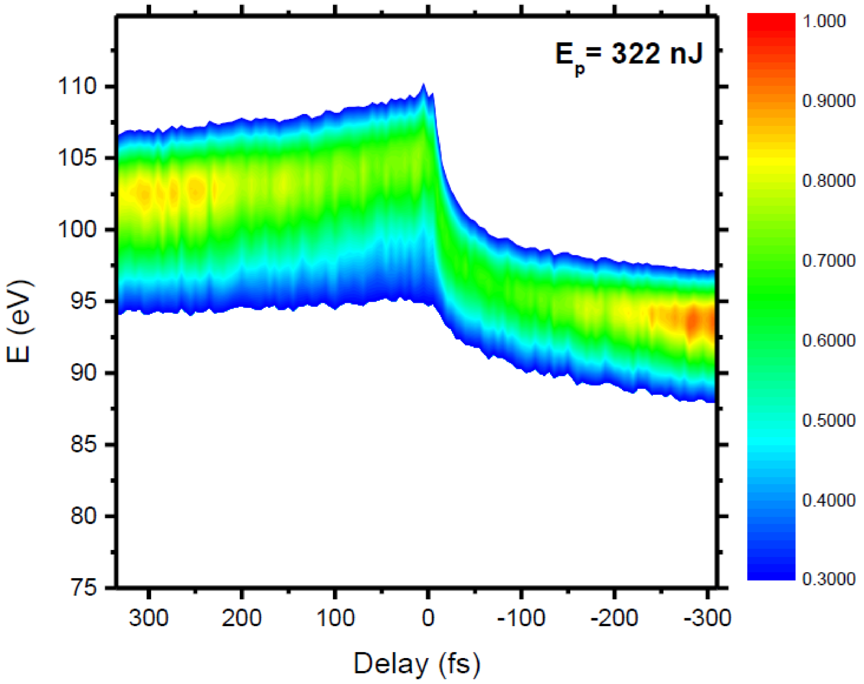

Figure 6.4: Measured streaking trace of Graphene at 322 nJ NIR pulse energy

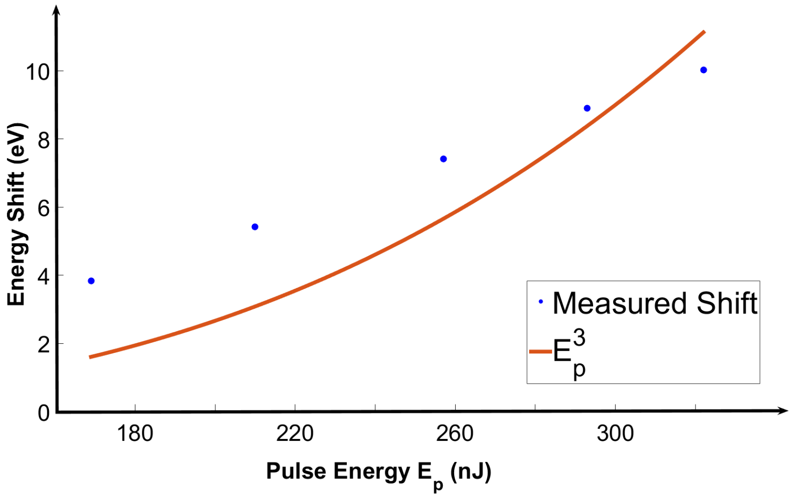

Figure 6.5: Measured spectral shift (blue data points) as a function of the pump-pulse energy, Ep, at a fixed pump-probe delay. The red line is the calculated Ep^3 line

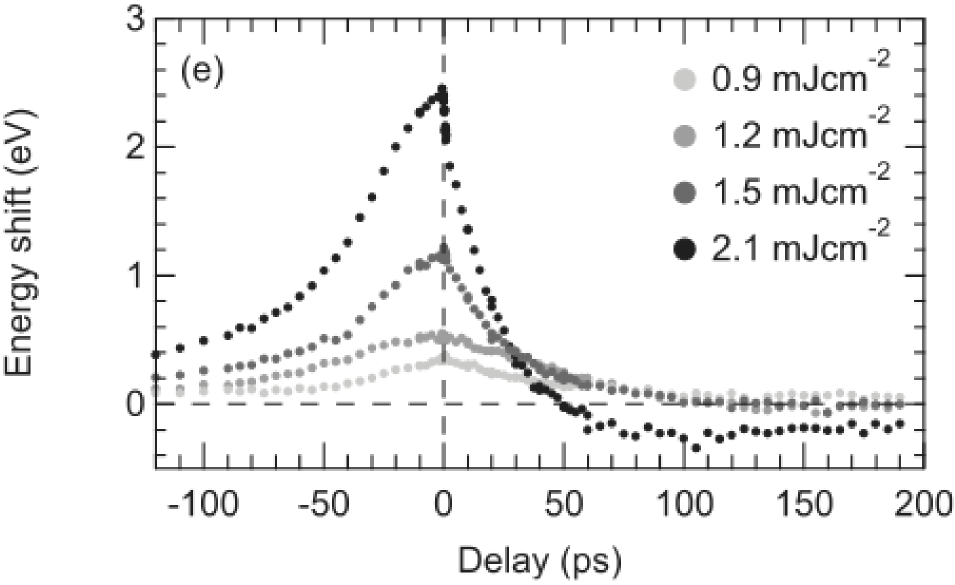

Figure 6.6: Extracted spectral shifts given with respect to an unpumped spectrum [112]

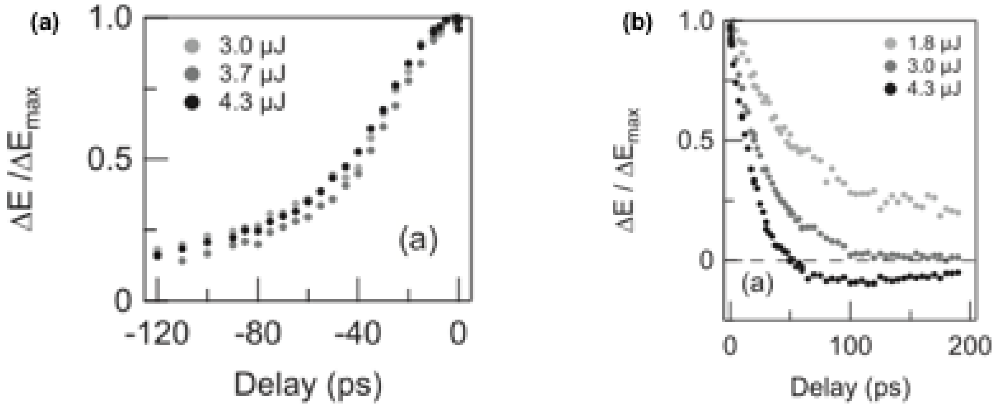

Figure 6.7: Relative relaxation time $\frac{\Delta E}{E_{max}}$ in the negative (a) and positive (b) delays respectively as measured in [112]

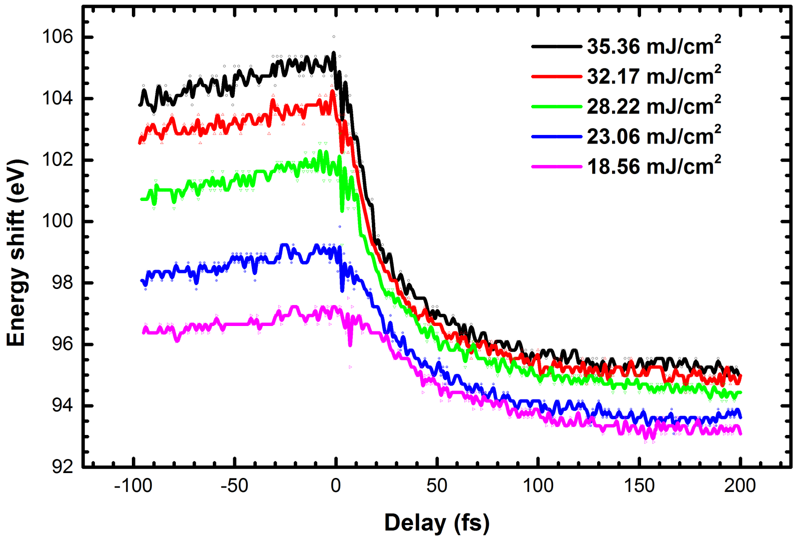

Figure 6.8: Measured relaxation of the NIR energy shift both in the positive delay and negative delay as well

are ejected after the emission of the pump electrons, therefore there are two phases of their dynamics; one before they reach the pump photoelectron disc and the other after they penetrate it on their way to the detector. This explains the characteristic asymmetry of the traces between the positive and negative delays. Moreover, in contrast to the relaxation times extracted in the case of negative delay, when we increase the pump intensity this leads to a faster relaxation time in the positive delay situation.

Figure 6.8 shows the positive and negative delays as measured in our laboratories.

On the other hand, Figure 6.9a and 6.9b shows the measured relative relaxation $\frac{\Delta E}{E_{max}}$ in the positive and negative delay respectively as measured in our labs.

It is interesting to notice that we encounter basically the same mechanism as compared to the work done in [112]. The relaxation of the energy shift seems to be NIR-independent in the negative delay (NIR lags behind the XUV photoemitted electrons). On the other hand, the relaxation of the energy shift seems very interesting when the NIR pulse proceeds the XUV pulse (positive delay) where the energy shift relaxations happens faster for large intensities. This result reassures the legitimacy of the mean field model used to describe the situation at several femtoseconds as discussed in this chapter. Our measurements serves as a successful extrapolation of the

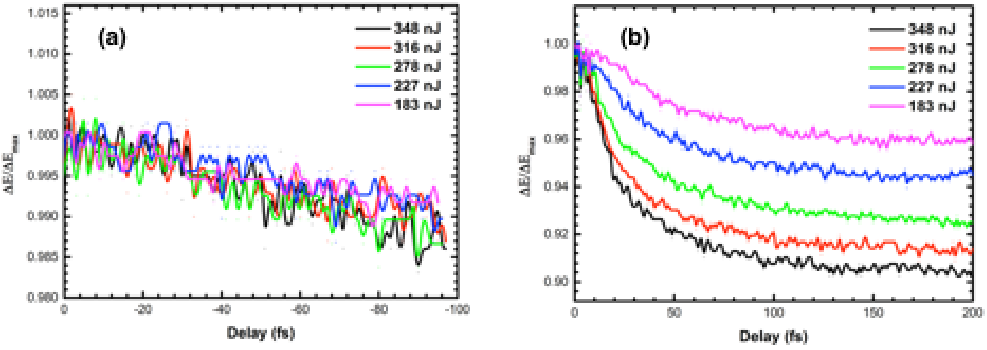

Figure 6.9: Relative relaxation time $\frac{\Delta E}{E_{max}}$ for negative (a) and positive (b) delay respectively as measured in our labs

mean-field model down to femtosecond time scales. This is inevitable if one seeks to undo the high laser intensities effect on the XUV photoemissioned electrons.

Chapter 7

Measuring excitation in PES experiments

7.1 PES experiments on GaAs

Seeking a photoemission signature of Rabi oscillations in a narrow bandgap material like GaAs is not a simple task due to the relatively small number of expected excited carriers from the VB to the CB in addition to the low signal to noise ratio. This was the reason why our approach aimed at finding an excitation signal first and later try to study the dynamics of this excitation signal as a signature of Rabi oscillation. In other words, we aimed at comparing the photoemission spectra before and after the impinging of the NIR field on the GaAs surface as a first step, this was a proof-of-principle experiment.
As discussed in Chapter 3, the intensity of the electric field has an oscillatory effect on the excited signal, this is well depicted in Figure 7.1. We used Equation 3.14 and set the detuning factor Δ to zero. The two level system is a simplification of the real situation but still it can give an insight into the behavior of the possible excitation.

In a real condensed matter semiconductor, we have to account for decoherence effects due to the scattering of carriers in the CB. In fact, according to [116], in the case of GaAs one should expect to excite only few percents to the CB and only part of these excited carriers will be de-excited back to the VB. One can use both polarizations, parallel and perpendicular in order to perform the streaking experiments. Using parallel streaking scheme offers the information about the intensity of the NIR field while the perpendicular streaking scheme gives the chance of having less undesired streaking in the spectrogram tails.

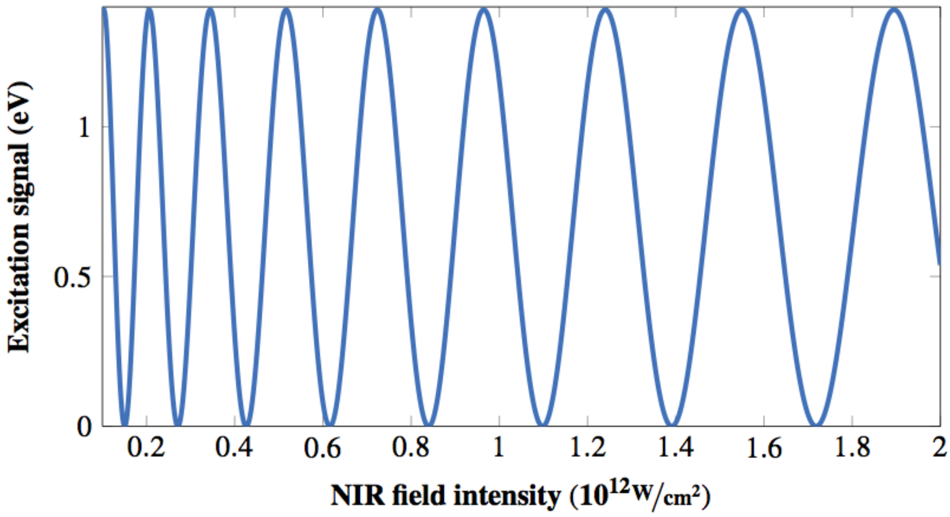

Figure 7.1: Dependence of the excitation signal on the NIR-field intensity in the two level approximation. This oscillation behavior of the excitation signal is determined from Equation 3.14 where the detuning factor Δ is assumed to be zero

7.1.1 Challenges of Measuring the Photoemission Signal

Streaking in the parallel polarization scheme

In a typical streaking experiment where the polarization of the NIR field is along the TOF, the energy of the photoelectrons is altered according to the instant of arrival of the NIR field. At the instant of overlap between the XUV and NIR fields, this could account to several electronvolts. Figure 7.2 shows a measured streaking trace done on GaAs in the parallel polarization scheme.

As seen in Figure 7.2, we also have streaking at the very tail of the spectrogram. This means that the expected signal itself is buried under several hundreds of meV which minimizes the signal to noise ratio and makes the chance of seeing a signature of this expected signal very slim.

Streaking in the perpendicular polarization scheme

On the other hand, measuring streaking traces in the perpendicular polarization scheme is advantageous since it helps to minimize the streaking effects at the tails of the spectrogram as seen in Figure 7.3. The measurement in Figure 7.3 shows a down shift in the photoelectron line at the instant of overlap between the NIR and XUV pulses. This matches what was expected in [117].

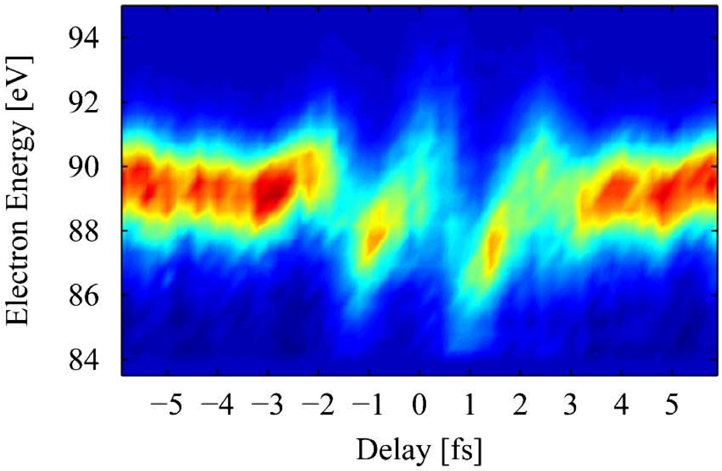

Figure 7.2: Streaking of GaAs 3d-Ga peak in the parallel polarization scheme

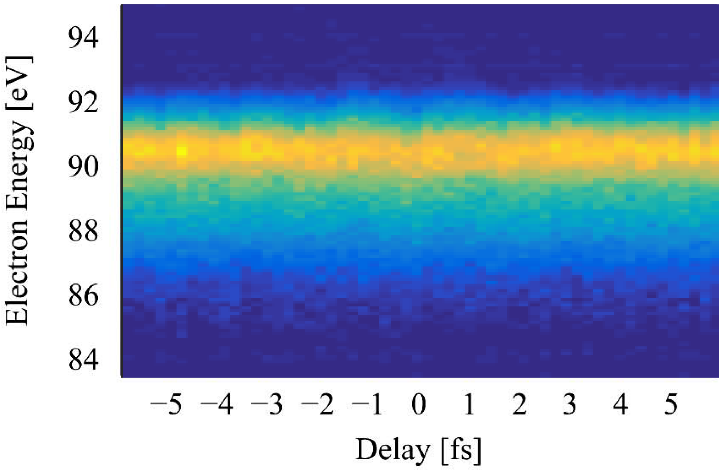

Figure 7.3: Streaking of GaAs 3d-Ga peak in the perpendicular polarization scheme

Moreover, streaking in the perpendicular polarization scheme is also beneficial since it helps to get rid of the space-charge effects. In a streaking experiment, photoelectrons are freed by the XUV pulse and then streaked by the NIR field. However, if the NIR intensity is high enough, electrons freed by the NIR field via multiphoton absorption process cause what we call as space charge shift [118]. Trying to reach high intensities in the range of 10^{12} W\ cm^2 to maximize the signal, photoelectrons freed by NIR pulses could reach the detector with comparable energy as those freed by the XUV pulse. This is a major distortion of the photoelectron signal. Streaking in the perpendicular polarization saves our spectrogram from this undesired Above Threshold Ionization (ATI) electrons [111], since the

ionization probability of ATI electrons is significantly lower in the perpendicular polarization scheme [119]. According to [117], streaking in the perpendicular scheme will cause a periodic down shift of a frequency double that of the NIR field.
On the other hand, photoelectrons created via multiphoton absorption could cause space charge which pushes the energy of all photoelectrons into higher energies, shifts of around $1.5eV$ were reported [42]. One way to overcome such problem, is to try to use doped semiconductors in order to induce conductivity which removes space-charge. However, the space-charge shifts the whole photoemission lines equally into higher energies, this makes correcting it relatively easy having the energy of the core lines well defined for various materials.

Experimental Difficulties

In a condensed matter semiconductor, which is way more complicated compared to a two level system, several effects could take place which makes the chances to see a signature of a possible excitation of some carriers from the VB to the CB even worse. Different effects could be discussed as the most prominent sources of complicating the resolution of a possible excitation signal such as surface photo-voltage effect and sample destruction due to above threshold high intensity laser.

Surface photo-voltage effect Near the semiconductor surface, the surface states causes excess charge which are compensated by the bulk charge which leads to band bending taking place across the surface in the opposite direction in the energy space in the case of n- or p- doped semiconductors. This is called surface photo-voltage effect and doped semiconductors usually encounter such effect. According to [120], a reduction in this band bending due to a separation of the excited electron-hole pairs in the strong electric field. Though, this happens on a much slower time scale, in the order of hundreds of femtoseconds, which is slower than the dynamics of excitation studied in such experiments. We avoided such a problem by using only undoped samples through the course of the experiments.

High intensity laser and carrier dynamics Attaining Rabi oscillations in semiconductors means that one has to use relatively high laser NIR intensities, where electrons are excited from the VB to the CB. If the number of those excited electrons are large enough, carrier-phonon scattering could takes place which might lead to overheating the crystal and destroying it [121]. Figure 7.4 summarizes the different scattering processes which usually take place in a bandgap material.

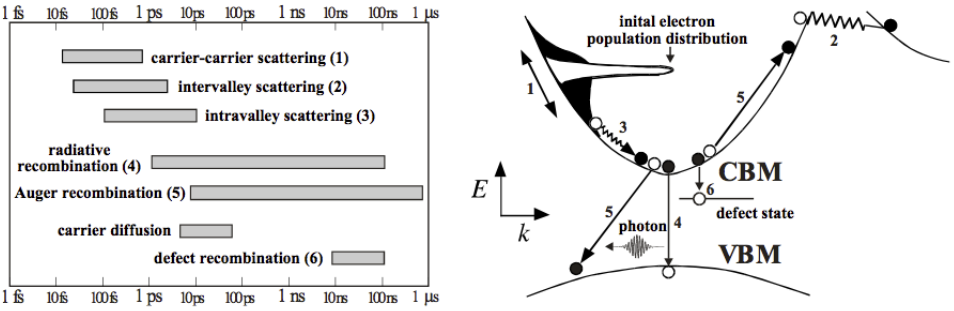

Figure 7.4: Carrier dynamics in a semiconductor and their approximate time scales which depend partially on the carrier density and\or temperature [58]. The photoexcited carrier density is assumed to be high and the system is at room temperature . Adapted from [122]

Since we are interested in the femtosecond time domain which is comparable to the dephasing time in Rabi oscillation, we are going to focus just on three scattering process mentioned in Figure 7.4 which are the carrier-carrier scattering, inter-valley scattering, and intra-valley scattering.

Carrier-Carrier Scattering When an electron is excited from the VB to the CB, a hole is created in the VB. This would suggest that we encounter three types of scattering: among electrons, among holes, in addition to the scattering among holes and electrons. These phenomenon are similar though not identical due to the different physical properties of electrons and holes [123]. In GaAs, which is a narrow direct bandgap material, this carrier-carrier scattering process is the fastest and is estimated to be below 30fs according to [124]. Moreover, if the excited carrier density increased dramatically, the time scale of this scattering process could be even shorter. Still, at higher carrier densities the inelastic scattering rate also increases and screening and degeneracy reduce the intrinsic scattering rate. This means that the time scale of the carrier-carrier scattering is decreased only moderately [123]. This process contribute ultimately in over-heating the lattice and finally destroying it since it preserves the energy inside the system.

Inter- and Intra-Valley Scattering These scattering processes transfer the energy to the lattice from the carriers via carrier-phonon coupling. The created phonon can carry high momentum which permits the inter-valley scattering. In a system where we have high density of unoccupied states,

the transition rate is considerably high and average transition time of electrons is about $100fs$ in GaAS according to [125]. Moreover, intra-valley contributes also to the relaxation of the electron energy and its transfer time is estimated to be around $160fs$ according to [125]. Though due to phonon energy, several repetition of this intra-valley processes are usually needed [58].
It is well known that phonon coupling is too slow compared to the time scale of Rabi flopping, still it can possibly damage the crystal. According to [126], individual atoms, molecules, and ions could leave the surface when the pulse energy deposited in the the sample is transferred into kinetic energy, this leads to unrecoverable changes at the surface and is called ablation. On the other hand, theory predicts that major changes to the band structure due to electronic excitations [127]. Bandgap renormalization takes place if the the carrier concentration are dense enough to extend over the whole Brillouin zone. In fact, if one excites around 1% of the carriers to the CB, then GaAs encounters what is called the semiconductor-metal transition. In this case, the NIR laser pulse will be screened at the surface of the sample and Rabi oscillation will not occur within the sample. Therefore, one should take into account how much carriers are excited into the CB to avoid screening effects and also avoid the damage of the lattice. In GaAs, one should aim at NIR intensities around 10^{12} W\ cm^3 [55] since such intensities are below the damage threshold of the crystal and enough to possibly see Rabi oscillation signature in the photoemission spectra.

7.1.2 Approaches for data analysis

We didn't embrace very ambitious data analysis approaches at first. The task was first simply to see some NIR-induced excitation from the VB to the CB. Later, we could look at the dynamics of this presumed excitation. To do so, the approach was to compare the spectra before and after the impinging of the NIR field. An excitation would mean a difference between the two spectra.

Parallel streaking scheme

Performing streaking photoemission experiments is itself beneficial since it enables the synchronization between the NIR and the XUV pulses which is extremely important to tune the spectra which contain the expected excitation from those which do not. Figure 7.5 shows a typical photoemission streaking trace of the VB and the Ga 3d core level in (100) GaAs samples using an XUV mirror reflecting at $112eV$ with $1.8eV$ bandwidth.

As discussed before, the idea is simply to subtract the spectra before

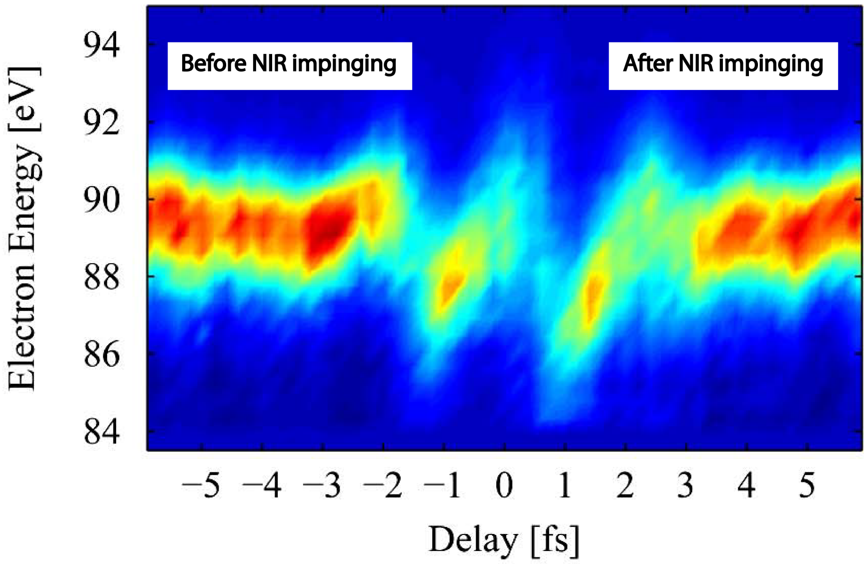

Figure 7.5: Streaking trace in the parallel scheme of GaAs 3d-Ga peak. Signal is extracted from the subtraction of the spectra before and after the impinging NIR instant

the impinging of the NIR field (positive delay) from the spectra after its impinging (negative delay), the difference is called the excitation signal. After implementing several approaches, it was clear that comparing the spectra before and after the impinging of the laser field does not show an excitation signal. There is no clear correlation between the intensity of the NIR and the amplitude of the excitation signal. Moreover, there is no clear positive sign of the excitation signal. This is a sign of low signal to noise ratio, in addition to the streaking at the tails of the spectrogram which is way larger than the expected few meV signal. One way out of this is to aim for an almost streaking-free trace. In other words, we streak in the perpendicular scheme as discussed before.

Perpendicular streaking scheme

Figure 7.6 shows a typical photoemission streaking trace in the perpendicular geometry of the VB and the Ga 3d core level in (100) GaAs samples using an XUV mirror reflecting at $112eV$ with $1.8eV$ bandwidth.

As discussed before, the idea is simply to subtract the spectra before the impinging of the NIR field (positive delay) from the spectra after its impinging (negative delay), the difference is called the excitation signal. One could already see that at the tails of the spectrogram we have almost streaking-free spectra which leaves us with only the challenge of a good signal to noise ratio. It is obvious that streaking in the perpendicular

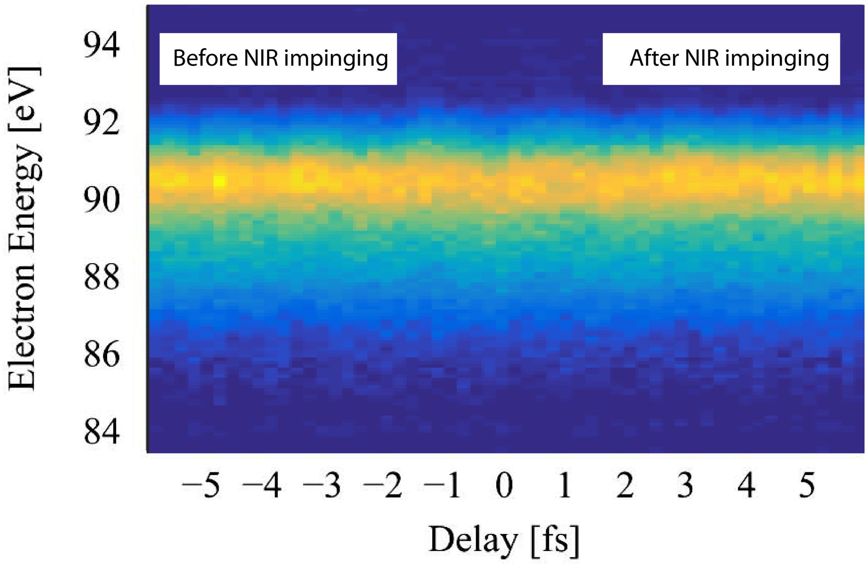

Figure 7.6: Streaking trace in the perpendicular scheme of GaAs 3d-Ga peak bands using an XUV mirror of $1.8eV$ bandwidth. Signal is extracted from the subtraction of the spectra before and after the impinging NIR instant

scheme makes us blind concerning the intensity of the NIR field, this could be a fair price to pay in order to get the streaking-free trace.

Unfortunately, after using several approaches, there is no clear positive sign of the excitation signal, this could be a sign of still low signal to noise ratio. The intensity of the NIR field was increased by opening an iris gradually until we burn a spot on the surface of the sample making sure that we already had enough NIR intensity to see a potential excitation signal.

7.2 PES experiments on Graphene

Now, we shift to 2-Dimensional (2D) materials and chose Graphene as our candidate. PES measurements were collected at AS3 beamline. To the best of our knowledge, this is the first time such measurements were collected on 2D materials. Figure 7.7 shows one of the streaking traces in the parallel polarization scheme.

By devising a method to cancel out the streaking of the spectrogram, the direct comparison of the individual spectra for every delay setting becomes possible. The method used in this work consisted of fitting a Gaussian to each and every individual spectrum of the spectrogram. In this way, the center of the emission spectrum was determined. Then each spectrum was

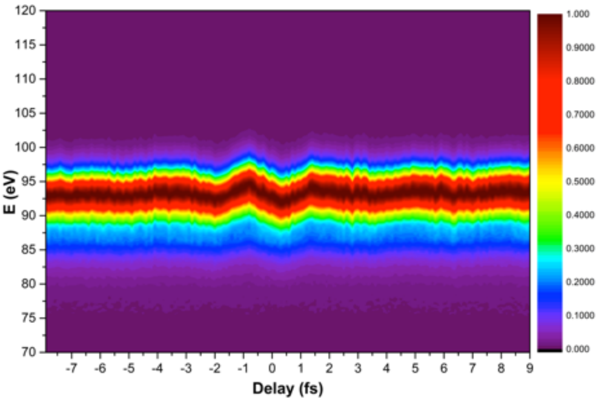

Figure 7.7: Streaking trace in the parallel polarization scheme of Graphene peak.

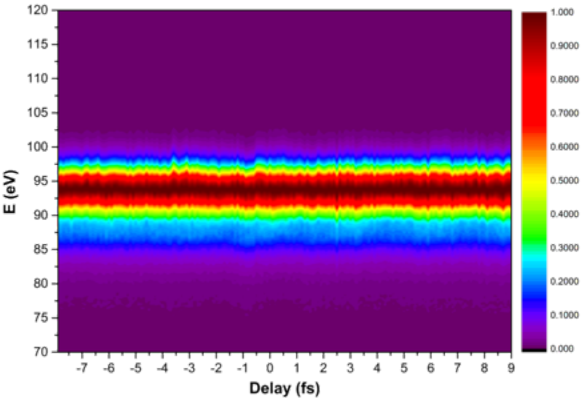

Figure 7.8: De-streaked Spectrogram trace collected in Figure 7.7

offset so that the peak matches the expected energy (in this case 93 eV). Finally the spectra were normalized so that the counts on each spectrum is constant. By those means we get the “de-streaked” spectrogram as one can see in Figure 7.8.

As we did in the PES traces on GaAs, we tried to subtract the spectra in Figure 7.8 before and after the impinging of the laser field. This subtraction should hold the information about the population transitions for every delay setting. By subtracting the average of the recorded spectra for negative delays (XUV before IR), from every spectrum, we obtain the so-called “differential” trace.
On the other hand, Figure 7.9 shows a de-streaked spectrogram where the vertical axis is the energy axis. The existence of a signal would suggest that if we subtract the spectra before the impinging of the laser field (positive delay) from the specta measured after the impinging of the laser field

(positive delay), we will get a consistant positive value. Unfortunately, we dont see such a signal.

We cannot see a consistent signal. A signal might exist within the noise, so trying to eliminate the sources of noise arising from the used experimental tools could be the way to go.

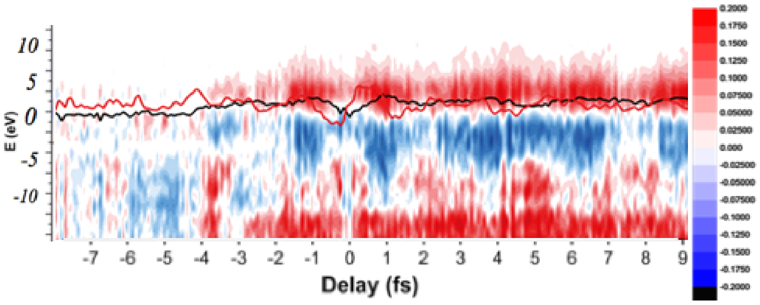

Figure 7.9: A normalized de-streaked spectrogram. The black and red lines shows the performed subtraction at each delay step of a core band and the VB respectively.

Chapter 8

Summary and Conclusion

Summary

In the framework of this thesis, photoelectron streaking experiments on small bandgap semiconductors were performed. Such experiments involve several challenges that arise especially in the case illuminating small bandgap semiconductors, like GaAs, with relatively high laser intensities.

One challenge are the Above threshold Ionization (ATI) electrons emitted via the nonlinear multiphoton ionization process (MPI). In order to overcome this problem, we have successfully designed and implemented a narrow bandwidth Chromium\scandium multilayer XUV mirror which reflects at relatively high photon energy [72]. This development proves to be beneficial to PES experiments of semiconductors having electronic band-gaps in the visible spectral range.

Another challenge was the intrinsically limited spectral resolution of attosecond photoelectron experiments posing a trade-off situation. To be able to see some excitation from VB, we should aim for a good spectral resolution. On the other hand, we should have the temporal resolution small enough to successfully perform the attosecond photoelectron streaking experiment. This challenge is intrinsic in the case of small bandgap materials and we can only make the situation better by designing a small bandwidth XUV mirror. Having this in mind, we have successfully designed and used a Mo\B4C multilayer XUV mirror which has a small bandwidth. The ability to have this relatively small bandwidth was very advantageous since it allowed us to spectrally disentangle the photoelectrons of the VB (where a possible excitation could be detected) and that of the Ga 3d photoelectrons. The validity of the mirror was tested by performing attosecond streaking experiments on GaAs samples in the AS3 beamline.

PES streaking temporal resolution is extremely challenging and has not yet yielded signatures of the desired Rabi oscillations. However, we have employed the techniques successfully to observe an ultrafast (4 fs) build-up of CB-population in graphene that could pave the way to future ultrafast signal metrology.

Conclusion

This thesis reports on developments that have been undertaken to extend the capabilities of attosecond photoelectron streaking experiments from solid surfaces to explore charge transfer dynamics in bandgap materials. Starting from the experimental scheme that allows recording the relative timing of photoelectron emission from different orbitals in a solid, several strategies had to be developed and implemented to overcome limitations so far characteristic for attosecond photoelectron experiments.

- In particular, the study of optical excitations in band-gap materials requires a spectral resolution sufficient to detect the light induced energy gain of the excited electrons. To date, in typical experiments attosecond temporal resolution comes at the price of a spectral resolution >5eV due to the bandwidth of the attosecond XUV pulses. This thesis discusses the development of tailored XUV optics that on the one hand allows to spectrally separate valence- from conduction band photoelectron emission (bandwidth <2eV) while on the other hand they still provide sufficient bandwidth for sub-femtosecond temporal resolution.
- Short pulse laser excitation at the surface of a band-gap material causes the release of large numbers of photoelectrons from the sample surface via nonlinear excitation pathways. This unwanted but unavoidable charge cloud affects the XUV released photoelectrons and hinders a stringent analysis of the recorded time delay scans. To overcome this problem a combination of an orthogonal streaking field significantly reducing the release of surface photoelectrons in combination with novel XUV optics pushing the central photon energy of the attosecond pulses towards 150 eV has been developed in this thesis.

With these developments successfully established it became possible to demonstrate that attosecond photoelectrons spectroscopy now is a viable tool to track electron excitation dynamics in band-gap materials. A proof-of-principle measurement explores the few-cycle laser driven build-up of conduction band population in Graphene.

Appendices

Appendix A

List of Publications

1. Alxender Guggenmos, **Ayman Akil**, Marcus Ossiander, Martin Scaeffer, Abdallah Azzeer, Gerhard Boehm, Marcus-Christian Amann, Reinhard Kienberger, Martin Schultze, and Ulf Kleineberg. *Attosecond photoelectron streaking with enhanced energy resolution for small-bandgap materials.* Optics Letters, Vol. 41, No. 16, August 15 2016. (Alxender Guggenmos, Ayman Akil contributed equally to this article)

2. Axender Guggenmos, Michael Jobst, Marcus Ossiander, Stefan Raduenz, Johann Riemensberger, Martin Schaeffer, **Ayman Akil**, Clemens Jakubeit, Philip Boehm, Simon Noever, Bert Nickel, Reihard Kienberger, and Ulf Kleineberg. *Chromium/scandium multilayer mirrors for isolated attosecond pulses at 145 eV.* Optics Letters, Vol. 40, No. 12, June 15 2015.

3. Marcus Ossiander, Michael Jobst, Stefan Neppl, Johan Riemensberger, Martin Schaeffer, Elisabeth Bothschafter, Michael Gerl, Andreas Kim, **Ayman Akil**, Sebastian Jarosch, Johannes Barth, Ferenc Krausz, Peter Feulner, and Reinhard Kienberger. *Photon Energy Dependent Photoemission Delay in Tungsten.* Ultrafast Optics UFO conference paper, August 2015.

Bibliography

[1] O. D. Muecke, “Signatures of carrier-wave rabi flopping in gaas,” *Phy. Rev. Lett.*, 2001.

[2] O. D. Muecke, “Carrier-wave rabi flopping in gaas: role of the carrier-envelope phase,” *Optics Letters*, 2004.

[3] K. Nakata, “Photoenergy conversion with tio2 photocatalysis: New materials and recent applications,” *Electrochimica Acta*, 2012.

[4] K. Varju, “Physics of attosecond pulses produced via high harmonic generation,” *American Journal of Physics*, 2009.

[5] K. Kulander, “Dynamics of short-pulse excitation, ionization and harmonic conversion,” *Super-Intense Laser-Atom Phys. Ed. by B. Piraux, A. L'huillier, and K. Rzazewski*, 1993.

[6] K. Schafer, “Above threshold ionization beyond the high harmonic cutoff,” *Phys. Rev. Lett.*, 1993.

[7] P. Corkum, “Plasma perspective on strong field multiphoton ionization,” *Physical Re- view Letters*, 1993.

[8] M. Lewenstein, “Theory of high-harmonic generation by low-frequency laser fields,” *Phys. Rev. A*, 1994.

[9] F. Quere, “Time-resolved study of laser-induced breakdown in dielectrics,” *EPL (Europhysics Letters)*, 2001.

[10] A. Amtout, “Resonant raman scattering from excitons in tio2,” *Physical Review B*, 1992.

[11] E. Goulielmakis, “Single-cycle nonlinear optics,” *Science*, 2008.

[12] M. Schultze, “Controlling dielectrics with the electric field of light,” *Nature*, 2013.

[13] S. Wall, “Ultrafast changes in lattice symmetry probed by coherent phonons,” *Nature Communications*, 2012.

[14] M. S. Diakhate, "Quantum dynamical study of the ampli- tude collapse and revival of coherent a 1g phonons in bismuth: a classical phenomenon?," *Applied Physics A*, 2009.

[15] E. M. Bothschafter, "Interband excitation and carrier relaxation as displacive driving force for coherent phonons," *EPJ Web of Conferences*, 2013.

[16] C. Zener, "A theory of the electrical breakdown of solid dielectrics," *Proceedings of the Royal Society of London*, 1934.

[17] T. E. Glover, "Observation of laser assisted photoelectric effect and femtosecond high order harmonic radiation," *Physical Review Letters*, 1996.

[18] Y. Nabekawa, "Interferometric autocorrelation of an attosecond pulse train in the single-cycle regime," *Physical Review Letters*, 2006.

[19] P. M. Paul, "Observation of a train of attosecond pulses from high harmonic generation," *Sience*, 2001.

[20] Y.Mairesse, "Attosecond synchronization of high-harmonic soft x-rays," *Science*, 2003.

[21] T. Nomoto, "Optically excited near-surface phonons of tio2 (110) observed by fourth-order coherent raman spectroscopy," *The Journal of chemical physics*, 2009.

[22] K. Ishioka, "Raman generation of coherent phonons of anatase and ru- tile tio2 photoexcited at fundamental absorption edges," *Physical Review B*, 2012.

[23] E. Hendry, "Electron transport in tio2 probed by thz time-domain spectroscopy," *Physical Review B*, 2004.

[24] W. A. Tisdale, "Hot-electron transfer from semiconductor nanocrystals," *Science*, 2010.

[25] V. P. Zhukov, "Ab initio approach to the excited electron dynamics in rutile and anatase tio2," *Journal of Physics. Condensed matter*, 2010.

[26] Z. Wang, "Wavefront control to generate ultraviolet supercon- tinuum by filamentation of few-cycle laser pulses in argon," *Optics Letters*, 2010.

[27] R. Ernstorferet, "The formation of warm dense matter: experimental evidence for electronic bond harden- ing in gold," *Science*, 2009.

[28] L. Chiodo, "Self-energy and excitonic effects in the electronic and optical properties of tio2 crystalline phases," *Physical Review B*, 2010.

[29] G.H.Wannier, “Wavefunctions and effective hamiltonian for bloch electrons in an electric field,” *Physical Review*, 1960.

[30] W. Franz, “Einfluss eines elektrischen feldes auf eine optische absorptionskante,” *Zeitschrift fuer Naturforschung*, 1958.

[31] L. V. Keldysh, “Behaviour of nonmetallic crystals in strong electric fields,” *Soviet Physics, JETP*, 1958.

[32] T. Fuji, “Attosecond control of optical waveforms,” *New Journal of Physics*, 2005.

[33] T. Fuji, “Monolithic carrier-envelope phase- stabilization scheme,” *Optics Letters*, 2005.

[34] M. Fiess, “Versatile apparatus for attosecond metrology and spectroscopy,” *The Review of Scientific Instruments*, 2010.

[35] T. Clausnitzer, “Highly efficient transmission gratings in fused silica for chirped-pulse amplification systems,” *Applied Optics*, 2003.

[36] A. L. Cavalieri, “Intense 1.5-cycle near infrared laser waveforms and their use for the generation of ultra-broadband soft-x-ray harmonic continua,” *New J. Phys.*, 2007.

[37] T. Udem, “Optical frequency metrology,” *Nature*, 2002.

[38] L. Xu, “Route to phase control of ultrashort light pulses,” *Optics Letters*, 1996.

[39] A. Apolonski, “Controlling the phase evolution of few-cycle light pulses,” *Physical Review Letters*, 2000.

[40] J. Rauschenberger, “Carrier-envelope phase-stabilized amplifier system,” *Laser Physics Letters*, 2005.

[41] G. Tempea, “Prl,” *Physics Review Letters*, 2000.

[42] S. Neppel, *Attosecond Time-Resolved Photoemission from Surfaces and Interfaces*. PhD thesis, Technische Universitaet Muenchen Physik Department E20, 2011.

[43] A. Wonisch, “Design, fabrication, and analysis of chirped multilayer mirrors for reflection of extreme-ultraviolet attosecond pulses,” *Appl. Opt.*, 2006.

[44] M. Hofstetter, “Attosecond dispersion control by extreme ultraviolet multilayer mirrors,” *Opt. Express*, 2011.

[45] R. Scheuerer, *Polarisations und winkelaufgeloste Photodesorptionsmessungen aus molekularen Kondensaten nach Rumpfanregung.* PhD thesis, Technische Universiteat Muenchen, 1996.

[46] I. Rabi, “On the process of space quantization,” *Phys. Rev.*, 1936.

[47] S. T. Cundiff, “Rabi flopping in semiconductors,” *Phy. Rev. Lett.*, 1994.

[48] S. Hughes *Physics Review Letters*, 1998.

[49] I. Rabi, “On the process of space quantization,” *Physical Review Letters*, 1936.

[50] Y. S. Bai, “Selective excitation of dressed atomic states by use of phase-controlled optical fields,” *Physical Review Letters*, 1985.

[51] R. Binder, “Ultrafast adiabatic following in semiconductors,” *Physics Review Letters*, 1990.

[52] A. Schulzgen, “Direct observation of excitonic rabi oscillations in semiconductors,” 1999.

[53] M. Saba, “Direct observation of the excitonic ac stark splitting in a quantum well,” *Physics Review B*, 2000.

[54] S. T. Cundiff, “Rabi flopping in semiconductors,” *Physical Review Letters*, 1994.

[55] O. Mucke, “Signatures of carrier-wave rabi flopping in gaas,” *Physics Review Letters*, 2001.

[56] S. Hunklinger, “Festkoerperphysik,” *Oldenbourg Wissenschaftsverlag GmbH*, 2009.

[57] H. Cotal, “V multijunction solar cells for concentrating photovoltaics,” *Energy and Environmental Science*, 2008.

[58] P. N. Saeta. PhD thesis, Harvard University, 1991.

[59] M. T. Ossiander, “On the expansion of attosecond streaking spectroscopy towards ultrafast surface dynamics,” Master’s thesis, Technische Universitaet Muenchen, 2014.

[60] A. Y. Cho, “Molecular beam epitaxy,” *Progress in Solid State Chemistry*, 1975.

[61] M. B. Panish, “Temperature dependence of the energy gap in gaas and gap,” *Journal of applied Physics*, 1969.

[62] R. F. Pierret *Advanced Semiconductor Fundamentals*, 1987.

[63] D. E. Aspnes, "Optical properties of alxgaas," *Journal of Applied Physics*, 1986.

[64] *Handbook of optical constants of solids.* 1998.

[65] *Low-Energy Electron Diffraction: Crystallography of Surfaces and Interfaces.* Wiley-VCH Verlag GmbH and Co. KGaA, 2012.

[66] *X-Ray Photoelectron Spectroscopy.* 2003.

[67] I. M. Vitomirov, "Geometric ordering, surface chemistry, band bending, and work function at decapped gaas(100) surfaces," *Physics Review B*, 1992.

[68] W. Chen, "Work function, electron affinity, and band bending at decapped gaas(100) surfaces," *Journal of Vacuum Science and Technology B*, 1992.

[69] D. D. Biegelsen, "Surface reconstructions of gaas(100) observed by scanning tunneling microscopy," *Physics Review B*, 1990.

[70] D. Paget, "Reflectance anisotropy spectroscopy: A probe for surface chemistry on (001) gaas," *Journal of Vacuum Science and Technology A: Vacuum, Surfaces, and Films*, 1995.

[71] C. J. Spindt, "Au and al schottky barrier formation on gaas (100) surfaces prepared by thermal desorption of a protective arsenic coating," *Journal of Vacuum Science and Technology B: Microelectronics and Nanometer Structures*, 1991.

[72] A. Guggenmos, "Chromium/scandium multilayer mirrors for isolated attosecond pulses at 145 ev," *Optics Letters*, 2015.

[73] C. Spielmann, "Generation of coherent x rays in the water window using 5 femtosecond laser pulses," *Science*, 1997.

[74] F. Eriksson, "14.5 % near-normal incidence reflectance of cr/sc x-ray multilayer mirrors for the water window," *Opteics Letters*, 2003.

[75] T. Kuhlmann, "Chromium scandium multilayer mirrors for the nitrogen kα line in the water window region," *Optics Letters*, 2002.

[76] T. Gorniak, "X ray holographic microscopy with zone plates applied to biological samples in the water window using 3rd harmonic radiation from the free-electron laser flash," *Optics express*, 2011.

[77] M. Santos-Lleo, "The first decade of science with chandra and xmm newton," *Nature*, 2009.

[78] M. Hentschel, “Attosecond metrology,” *Nature*, 2001.

[79] U. Kleineberg, “Waveform-controlled near-single-cycle milli-joule laser pulses generate sub-10 nm extreme ultraviolet continua,” *Optics Letters*, 2012.

[80] B. L. Henke *At. Data Nucl. Data Tables*, 1993.

[81] C. Montcalm *Optics Letters*, 1995.

[82] C. Montcalm, “Survey of ti-, b-, and y-based soft x-ray-extreme ultraviolet multilayer,” *Applied Optics*, 1996.

[83] A. Guggenmos, “Ion polished cr/sc attosecond multilayer mirrors for high water window reflectivity,” *Optics Express*, 2014.

[84] A. Guggenmos, “Aperiodic crsc multilayer mirrors for attosecond water window pulses,” *OPtics Express*, 2013.

[85] R. Kienberger, “Atomic transient recorder,” *Nature*, 2004.

[86] J. Gagnon *Optics Express*, 2009.

[87] S. Neppl, “Direct observation of electron propagation and dielectric screening on the atomic length scale,” *Nature*, 2015.

[88] M. Schultze, “Delay in photoemission,” *Science*, 2010.

[89] S. Neppl, “Direct observation of electron propagation and dielectric screening on the atomic length scale,” *Nature*, 2015.

[90] M. Schultze, “Attosecond band-gap dynamics in silicon,” *Science*, 2014.

[91] A. Guggenmos, “Attosecond photoelectron streaking with enhanced energy resolution for small-bandgap materials,” *Optics Letters*, 2016.

[92] E. Magerl, “A flexible apparatus for attosecond photoelectron spectroscopy of solids and surfaces,” *Review of Scientific Instruments*, 2011.

[93] K. M. Skulina, “Molybdenum/beryllium multilayer mirrors for normal incidence in the extreme ultraviolet,” *Applied Optics*, 1995.

[94] C. Bourassin-Bouchet, “Shaping of single-cycle sub-50-attosecond pulses with multilayer mirrors,” *New Journal of Physics*, 2012.

[95] A. Guggenmos, “Aperiodic crsc multilayer mirrors for attosecond water window pulses,” *Optics Express*, 2013.

[96] I. J. Sola, “Controlling attosecond electron dynamics by phase-stabilized polarization gating,” *Nature Physics*, 2006.

[97] T. Pfeifer, “Measurement and optimization of isolated attosecond pulse contrast,” *Optics Letters*, 2009.

[98] R. Kienberger, “Atomic transient recorder,,” *Nature*, 2004.

[99] M. Drescher, “Time-resolved atomic inner-shell spectroscopy,” *Nature*, 2002.

[100] S. Haessler, “Phase-resolved attosecond near-threshold photoionization of molecular nitrogen,” *Physics Review A*, 2009.

[101] C. Montcalm, “In situ reflectance measurements of soft- x-ray/extreme-ultraviolet mo/y multilayer mirrors,” *OPtics Letters*, 1995.

[102] B. Sae-Lao, “Molybdenum strontium multilayer mirrors for the 8-12-nm extreme-ultraviolet wavelength region,” *OPtics Letters*, 2001.

[103] J. Gagnon, “The accurate frog characterization of attosecond pulses from streaking measurements,” *Applied Physics B*, 2008.

[104] S. Jarosch, “Setup for attosecond photoemission spectroscopy of dielectrics,” Master’s thesis, Technische Universitaet Muenchen, 2015.

[105] *Electronic Excitations at Metal Surfaces.* Plenum Press, 1997.

[106] *Angle-Resolved Photoemission: Theory and Current Applications.* Elsevier, Amsterdam, 1992.

[107] J. Faure, “Full characterization and optimization of a femtosecond ultraviolet laser source for time and angle-resolved photoemission on solid surfaces,” *Review of Scientific Instrumuments*, 2012.

[108] S. Hellmann, “Time-resolved x-ray photoelectron spectroscopy at flash,” *New Journal of Physics*, 2012.

[109] B. J. Siwick, “Ultrafast electron optics: Propagation dynamics of femtosecond electron packets,” *Journal of Applied Physics*, 2002.

[110] X. J. Zhou, “Space charge effect and mirror charge effect in photoemission spectroscopy,” *J. Electron Spectrosc. Relat. Phenom.*, 2005.

[111] L. P. Oloff, “Time-resolved haxpes at sacla: probe and pump pulse-induced space-charge effects,” *New Journal of Physics*, 2014.

[112] L. P. Oloff, “Pump laser-induced space-charge effects in hhg-driven time- and angle-resolved photoelectron spectroscopy,” *Journal of Applied Physics*, 2016.

[113] S. Collin, "Transverse and longitudinal space-charge-induced broadenings of ultrafast electron packets," *Journal of Applied Physics*, 2005.

[114] A. Damascelli, "Multiphoton electron emission from cu and w: An angle-resolved study," *Physics Review B*, 1996.

[115] Y. Y. Jun, "Tuning the graphene work function by electric field effect," *Nano Letters*, 2009.

[116] Y. Niu, "The effect of electric field maximum on the rabi flopping and generated higher frequency spectra," *New Journal of Physics*, 2008.

[117] M. T. Ossiander, "On the expansion of attosecond streaking spectroscopy towards ultrafast surface dynamics," Master's thesis, Technische Universitaet Muenchen, 2003.

[118] M. Drescher, "X-ray pulses approaching the attosecond frontier," *Science*, 2001.

[119] M. Hentschel, "Attosecond metrology," *Nature*, 2001.

[120] P. Siffalovic, "Femtosecond time-resolved core-level photoelectron spectroscopy tracking surface photovoltage transients on p–gaas," *European Physics Letters*, 2002.

[121] J. Callan, "Ultrafast electron and lattice dynamics in semiconductors at high excited carrier densities," *Chemical Physics*, 2000.

[122] P. Siffalovic. PhD thesis, Universitaet Bielefeld, 2002.

[123] W. H. Knox, "Femtosecond carrier thermalization in dense fermi seas," *Physical Review Letters*, 1988.

[124] W. Z. Lin, "Femtosecond absorption saturation studies of hot carriers in gaas and algaas," *IEEE Journal of Quantum Electronics*, 1988.

[125] J. Shah, "Determination of intervalley scattering rates in gaas by subpicosecond luminescence spectroscopy," *Physics Review Letters*, 1987.

[126] S. K. Sundaram, "Inducing and probing non-thermal transitions in semiconductors using femtosecond laser pulses," *Nature materials*, 2002.

[127] D. H. Kim, "Band structure of femtosecond laser pulse excited gaas," *Solid state communications*, 1994.